ՀՀ ԳԱԱ Վ. Համբարձումյանի անվան Բյուրականի աստղադիտարան

Անահիտ Լյովայի Սամսոնյան

«Փոշով հարուստ աստղառաջացման բռնկումով գալակտիկաների և ակտիվ գալակտիկական միջուկների ուսումնասիրությունը ենթակարմիր [CII] 158 մկմ առաքման գծի միջոցով»

Ատենախոսություն

Ա. 03.02 - «Աստղաֆիզիկա, ռադիոաստղագիտություն» մասնագիտությամբ ֆիզիկամաթեմատիկական գիտությունների թեկնածուի գիտական աստիճանի համար

Գիտական ղեկավար՝

ֆ.մ.գ.դ. Արարատ Գևորգի Եղիկյան

Բյուրական - 2025

NAS RA Byurakan Astrophysical Observatory after V. Ambartsumian

Anahit L. Samsonyan

" Investigation of the dusty Starburst galaxies and Active Galactic Nuclei through the infrared [CII] 158 μm emission line"

Doctoral thesis

For the degree of Doctor of philosophy in the
specialization 01.03.02 – Astrophysics and Radioastronomy

Supervisor:
Dr. Ararat G. Yeghikyan

Byurakan – 2025

CONTENT

1. INTRODUCTION: INFRARED ASTRONOMY AS A TOOL TO STUDY ACTIVE GALAXIES

1.1. Infrared radiation: What is it? Why do we need it?

Radiation in the Electromagnetic Spectrum is categorized by wavelength. Short wavelength radiation is of the highest energy. Gamma, X-rays and Ultraviolet are examples of short wavelength radiation. Longer wavelength radiation is of lower energy. Examples include radio, microwaves and infrared. A rainbow shows the optical (visible) part of the Electromagnetic Spectrum and infrared (if you could see it) would be located just beyond the red side of the rainbow.

Infrared light, often abbreviated as IR, is a form of electromagnetic radiation that is invisible to our eyes but can be sensed as heat on our skin. All objects with a temperature above absolute zero (-273.15 degrees Celsius or -459.67 degrees Fahrenheit) emit infrared radiation because of the thermal motion of their constituent particles (atoms and molecules). This property makes infrared radiation useful for studying temperature variations and heat signatures. Astronomers have found that infrared radiation is especially useful when trying to probe areas of our universe that are surrounded by clouds of gas and dust. Because of infrared's longer wavelength, it can pass right through these clouds and reveal details invisible by observing other types of radiation. Infrared astronomy has been crucial in studying the formation of stars and planets, the interstellar medium, dusty star forming galaxies and the early Universe.

Infrared radiation covers the wavelengths from 0.7μm (micrometers) to 1 mm (millimeter), from near to far infrared. Near-Infrared (NIR) covers the wavelength range approximately 0.7 to 2.5μm. It is often used for studying overtone and combination bands in molecules, as well as for applications such as analyzing organic compounds, determining the composition of materials, and studying biological samples. Mid-Infrared (MIR) covers approximately 2.5 to 25μm. MIR spectroscopy is especially useful for identifying functional groups in organic molecules, as well as for studying chemical bonding, characterizing minerals, and investigating the properties of gases. Far-Infrared (FIR) covers approximately 25μm to 1mm. FIR spectroscopy is used for studying low-energy vibrational modes in molecules, as well as

for observing the rotational transitions of molecules. It is essential in astronomy for studying the cold interstellar medium and in condensed matter physics for investigating lattice vibrations in solids. It is important to note that these wavelength ranges are approximate, and the exact divisions between them can vary depending on the context and the specific instrumentation used. Infrared spectroscopy is a versatile tool with applications in various scientific disciplines, including chemistry, physics, astronomy, and environmental science. The choice of wavelength range depends on the specific research or analytical objectives.

All objects with a temperature above absolute zero emit thermal radiation, which includes infrared radiation. This radiation is a natural consequence of the thermal energy associated with the motion of particles within the object. Dust particles, whether in space or on Earth, are composed of tiny solid or liquid particles. These particles have a temperature, and therefore, they emit thermal radiation in the form of infrared light due to their thermal energy. The specific wavelengths of the infrared radiation emitted by dust particles depend on their temperature. The hotter the particles, the shorter the wavelengths of the emitted infrared radiation. Cooler particles emit longer-wavelength infrared radiation. In astronomy, interstellar dust particles are found in the vast regions of space between stars and within galaxies. These dust particles can absorb and re-radiate energy, and their infrared emissions are crucial for astronomers to study celestial objects. Astronomers use specialized telescopes and detectors sensitive to infrared wavelengths to observe and study the thermal emissions from dust particles in space. This allows them to gain insights into the composition, temperature, and distribution of dust in the cosmos. In summary, dust particles, like all objects with temperature, emit infrared radiation as thermal radiation. In astrophysics and various scientific disciplines, studying this emitted infrared radiation provides valuable information about the physical properties and conditions of the emitting dust particles and the environments in which they exist.

Polycyclic aromatic hydrocarbons (PAHs) are large organic molecules composed of carbon and hydrogen atoms arranged in multiple fused aromatic rings. These molecules are known for their interesting spectroscopic properties, especially in the infrared (IR) region of the electromagnetic spectrum. PAHs can emit and absorb infrared radiation, and they are often

studied in the context of astrochemistry and astrophysics, as well as in environmental and materials science. PAHs are known for their strong emission of infrared radiation when they are exposed to ultraviolet (UV) or visible light. This phenomenon is often referred to as "PAH emission features." The specific wavelengths at which PAHs emit infrared radiation are distinctive and are used as a diagnostic tool in various fields, including astronomy. In astronomy, PAHs play a crucial role in the interstellar medium, where they are abundant. They are responsible for the so-called "infrared emission bands" seen in the spectra of many galaxies, nebulae, and interstellar regions. These emission bands are used to study the chemical composition, temperature, and ionization state of the regions where PAHs are present, providing insights into the environments and processes in space. In summary, PAHs are known for their unique infrared spectroscopic signatures, and studying the infrared radiation emitted and absorbed by PAHs helps us understand their chemical properties, environments, and potential applications.

1.2. Atomic emission lines in Infrared

Another essential tool is Infrared atomic emission lines, which are spectral lines produced when electrons in atoms transition from higher to lower energy levels and emit photons in the infrared part of the electromagnetic spectrum. Infrared atomic emission lines serve as diagnostic tools in astrophysics. By studying the intensity, wavelength, and shape of these lines, astronomers can deduce crucial information about the temperature, density, chemical composition, and ionization state of the emitting gas. This helps in characterizing the nature and evolutionary stages of astronomical objects, from individual stars to entire galaxies. The atomic emission lines [Ne II] and [Ne III] refer to spectral lines associated with the ionized forms of the element neon (Ne) in the infrared part of the electromagnetic spectrum. The [Ne II] line corresponds to a transition of a singly ionized neon atom (Ne+) and emits infrared radiation at a wavelength of approximately 12.81μm. The [Ne III] line corresponds to a transition of a doubly ionized neon atom (Ne++) and emits infrared radiation at a shorter wavelength, approximately 15.55μm. The [Ne III] line is typically observed in hotter and more energetic environments than [Ne II]. It is commonly found in regions where there are high-

energy sources like hot stars, supernova remnants, and active galactic nuclei (AGN). The presence of [Ne III] indicates the presence of highly ionized neon atoms and provides insights into the intense radiation and heating processes in these regions. Observing and analyzing these neon spectral lines, along with other emission lines from various elements, allows astronomers to probe the physical conditions, composition, and ionization states of the gas in different astronomical objects. The specific wavelengths of these lines provide valuable diagnostic tools for understanding the nature of celestial sources and their radiation environments.

1.3. Sources of Infrared radiation as distributed in Active galaxies and the key contributions by Viktor Ambartsumian to AGN research

Ambartsumian was one of the first scientists to propose that the nuclei of galaxies could harbor extremely energetic and compact regions. This idea was revolutionary in the mid-20th century when the prevailing view was that galaxies were largely stable, passive systems. He suggested that some galaxies have "active" nuclei, which emit vast amounts of energy. These active regions, as we now understand, are powered by accreting supermassive black holes in the centers of galaxies, and they are responsible for phenomena like quasars and radio galaxies. Ambartsumian proposed that the centers of galaxies might contain massive and compact objects, far more massive than typical stars. This was a precursor to the modern understanding of supermassive black holes residing in the cores of many galaxies, including our own Milky Way. He speculated that these objects could play a key role in the high-energy processes observed in AGN, including the emission of jets and radiation across the electromagnetic spectrum. Ambartsumian also suggested that the processes in the nucleus of a galaxy could be related to bursts of star formation, an idea that resonates with our current understanding of AGN-starburst connections. Many AGNs are in galaxies undergoing intense star formation, and the interaction between AGN activity and star formation remains an area of active research today. One of his other groundbreaking ideas was that the nuclei of galaxies might serve as sites for the formation of new stars or other compact objects. While this idea

was initially controversial, it contributed to the development of modern concepts about galactic evolution, the role of AGN feedback, and the star formation cycles in galaxies [1].

Ambartsumian's ideas laid the groundwork for many modern concepts in extragalactic astronomy and AGN studies. His work on the existence of powerful processes occurring in the centers of galaxies was far ahead of its time, as it predated the discovery of quasars and the confirmation of supermassive black holes. His theories about violent energy release in galaxy nuclei helped astronomers move away from the view of galaxies as static systems and toward a dynamic model where accretion processes and AGN feedback influence the host galaxy's evolution. Today, Ambartsumian's contributions are recognized as foundational to our understanding of AGN, and his work continues to influence how we study galactic nuclei, black holes, and active galaxies [2, 3, 4].

In active galaxies, infrared (IR) radiation is a key diagnostic tool that reveals the interplay between various astrophysical processes, primarily dominated by Active Galactic Nuclei (AGN) and regions of star formation. The AGN standard scenario posits that a significant fraction of the IR radiation originates from the dusty torus surrounding the supermassive black hole (SMBH) at the galaxy's core. This torus, composed of gas and dust, absorbs the intense ultraviolet (UV) and X-ray radiation emitted by the accretion disk as material falls onto the black hole. The absorbed energy is then reprocessed and re-emitted as thermal IR radiation, particularly in the mid-IR (5-40 μm) and far-IR (40-500 μm) regions of the spectrum [5, 6, 7]. This characteristic AGN-induced IR radiation serves as a hallmark of obscured and heavily dust-enshrouded AGN activity, providing a key indicator of accretion processes hidden from optical or X-ray observations due to dust absorption [6].

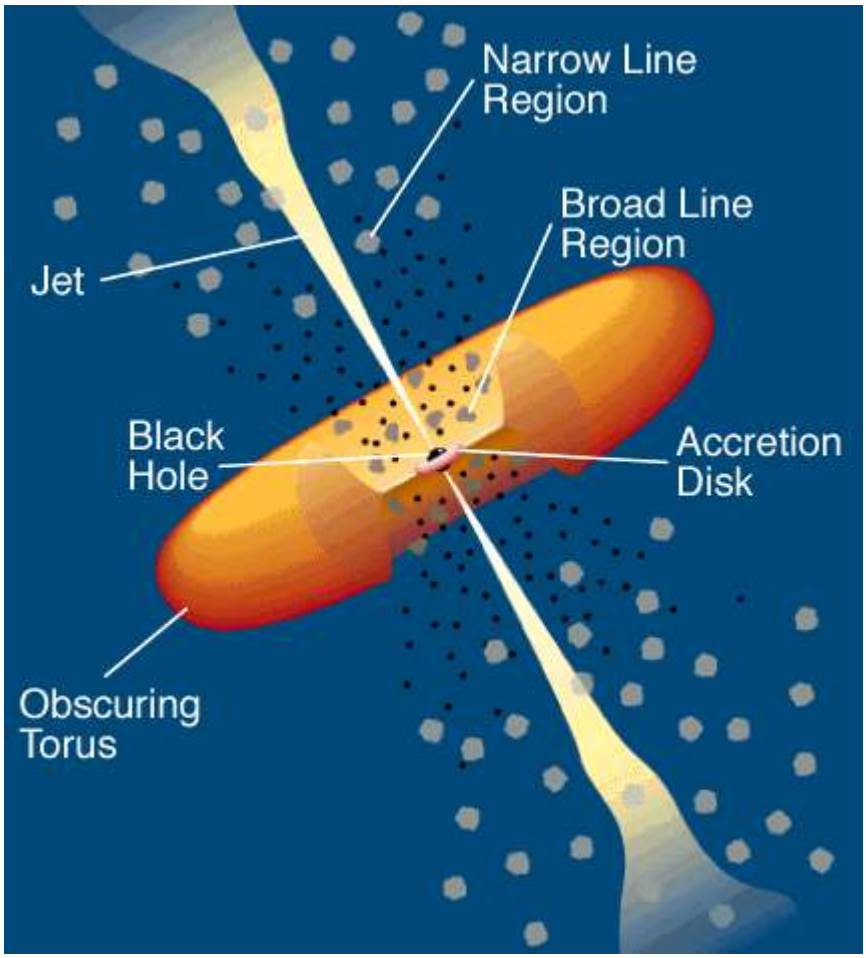

Figure 1-1. AGN Unified model classical sketch (Credit: C.M. Urry and P. Padovani)

The AGN Unified Model is a framework that seeks to explain the wide variety of active galactic nuclei (AGN) phenomena under a single, coherent model. This model was developed in response to the diversity of observational characteristics of AGNs, which, despite appearing different, were believed to stem from a common underlying structure and physical processes. The AGN Unified Model was formalized in the late 1980s and 1990s, primarily driven by the work of scientists such as Antonucci, Urry, and Padovani [5, 8, 9, 6]. The Figure 1-1 shows a classical sketch of a line-of-sight unification model showing the main ingredients of an active galactic nucleus.

The central premise of the unified model is that the apparent differences between various types of AGNs are largely due to the orientation of the AGN relative to the observer, rather than intrinsic physical differences. Below are the primary components of this model:

Supermassive Black Hole (SMBH):

At the heart of every AGN lies a supermassive black hole (SMBH), typically millions to billions of times the mass of the Sun. This black hole is the engine that powers the AGN, driving the emission of vast amounts of energy across the electromagnetic spectrum.

The SMBH is surrounded by an accretion disk of hot gas, which spirals inwards and emits radiation, particularly in the optical, UV, and X-ray bands. The accretion of material onto the black hole is the primary energy source for AGNs.

Accretion Disk:

The material in the accretion disk is heated to extremely high temperatures as it spirals toward the SMBH, emitting high-energy radiation. The accretion disk produces most of the optical and ultraviolet (UV) light observed in AGNs. In some cases, X-ray emission is also produced near the inner regions of the disk.

The radiation from the accretion disk ionizes surrounding gas, leading to the characteristic broad emission lines in some AGN spectra.

Broad-Line Region (BLR):

Surrounding the accretion disk is the broad-line region (BLR), a region of fast-moving gas clouds. These gas clouds are ionized by the radiation from the accretion disk and produce the broad emission lines seen in some AGNs. The gas in the BLR is moving at velocities of thousands of kilometers per second, which causes the emission lines to be broadened due to the Doppler effect.

The BLR is visible in Type 1 AGNs (e.g., Seyfert 1 galaxies and quasars) but is hidden in Type 2 AGNs due to the presence of a toroidal obscuring structure.

Obscuring Torus:

Surrounding the central SMBH and the accretion disk is a dusty, toroidal-shaped structure called the torus. This torus plays a key role in the unified model, as it determines how much of the central engine is visible depending on the observer's line of sight.

If the AGN is viewed face-on, the observer has a direct view of the accretion disk and BLR, which characterizes a Type 1 AGN. If viewed edge-on, the torus blocks the view of the accretion disk and BLR, and the observer only sees narrow emission lines from the narrow-line region (NLR), which characterizes a Type 2 AGN.

Narrow-Line Region (NLR):

The narrow-line region (NLR) is located further away from the SMBH than the BLR and consists of lower-density gas clouds moving at slower velocities (hundreds of kilometers per second). The NLR produces narrow emission lines that are seen in both Type 1 and Type 2 AGNs.

Since the NLR is located outside the torus, it is visible regardless of the viewing angle, contributing to the narrow emission lines observed in the spectra of all AGNs.

Relativistic Jets (in some AGNs):

In certain AGNs, particularly radio-loud AGNs such as blazars and radio galaxies, relativistic jets are launched from the vicinity of the SMBH. These jets, composed of charged particles, are ejected at nearly the speed of light along the poles of the black hole's spin axis.

If one of these jets is pointed directly toward Earth, the AGN appears as a blazar, which is characterized by strong and variable non-thermal emission across the electromagnetic spectrum. Jets are a defining feature of radio-loud AGNs.

The unified model classifies AGNs into two primary types based on orientation:

Type 1 AGN:

In Type 1 AGNs (e.g., Seyfert 1 galaxies and quasars), the observer has an unobstructed view of the central engine, including the accretion disk, BLR, and NLR. As a result, both broad and narrow emission lines are visible in the spectrum.

These AGNs tend to be bright in the optical and UV bands due to the direct view of the accretion disk.

Type 2 AGN:

In Type 2 AGNs (e.g., Seyfert 2 galaxies and radio galaxies), the view of the central engine is blocked by the obscuring torus, so only the NLR is visible. Consequently, only narrow emission lines are observed in the spectrum.

These AGNs are often brighter in the infrared due to the re-radiation of absorbed light by dust in the torus.

A central idea in the AGN unified model is that the differences between Type 1 and Type 2 AGNs are due to orientation. If the line of sight to the observer is unobstructed, the AGN appears as a Type 1, with both broad and narrow emission lines visible. If the line of sight passes through the torus, the AGN appears as a Type 2, with only narrow lines visible.

Additional Subclasses:

Blazars: These are a subclass of AGNs with relativistic jets pointed almost directly at the observer. They show extreme variability and strong non-thermal emission, with radiation dominated by the jets.

Radio Galaxies: These AGNs are characterized by powerful radio jets and lobes. Depending on the orientation, they can appear as either radio-loud quasars (if viewed face-on) or narrow-line radio galaxies (if viewed edge-on).

Evidence Supporting the Unified Model:

Polarized Light: In Type 2 AGNs, polarized light has been detected, suggesting that light from the hidden BLR is scattered into the line of sight by dust above or below the torus. This is consistent with the idea that the BLR exists in Type 2 AGNs but is obscured from direct view.

X-ray Observations: X-ray telescopes have detected hard X-rays emitted by the central engine in Type 2 AGNs, despite the optical light being obscured by the torus. X-rays can penetrate the torus, confirming the presence of the SMBH and accretion disk.

Infrared Emission: Infrared observations reveal re-radiated energy from the dusty torus, which absorbs optical/UV light and re-emits it in the infrared. This emission is present in both Type 1 and Type 2 AGNs, but is more dominant in Type 2 AGNs.

The AGN Unified Model has been critical in simplifying our understanding of AGN diversity. Instead of needing separate physical explanations for each AGN subtype, the model provides a unifying framework that attributes differences in appearance to orientation effects. It has

been instrumental in shaping modern AGN research and has guided the interpretation of multi-wavelength observations from instruments such as Hubble, Chandra, and ALMA.

In addition to the AGN itself, star formation regions within these galaxies contribute significantly to the observed IR emission. Massive, young stars formed in these regions heat the surrounding dust, causing it to radiate thermally in the far-infrared [10, 11]. This emission often peaks in the far-IR and is particularly strong in galaxies undergoing rapid star formation, such as starburst galaxies. The far-IR luminosity is directly linked to the star formation rate (SFR), as it traces the energy reprocessed by dust grains heated by ultraviolet radiation from young, hot stars [10, 11]. As a result, active galaxies with ongoing star formation typically exhibit strong infrared excesses, blending the contributions from both AGN activity and stellar processes [11].

Beyond the thermal IR continuum emission, both AGN and star formation regions also emit prominent atomic infrared emission lines. These lines, arising from the photoionization and excitation of gas in the galaxy, are useful for probing the physical conditions in the galaxy's interstellar medium (ISM). In AGN, high-ionization lines such as [O IV] at 25.9 μm and [Ne V] at 14.3 μm trace the ionizing radiation from the central black hole's accretion disk [1, 12]. These lines are particularly useful for diagnosing the degree of AGN activity and distinguishing it from star formation [12]. On the other hand, lower-ionization lines such as [Ne II] at 12.8 μm and [S III] at 18.7 μm are more commonly associated with HII regions and photo-dissociation regions (PDRs), where the gas is ionized by the ultraviolet light of young stars [12].

An additional important infrared signature in star-forming regions comes from polycyclic aromatic hydrocarbons (PAHs), which produce distinct emission features at 3.3, 6.2, 7.7, 8.6, and 11.3 μm [13]. PAH molecules are excited by ultraviolet radiation from young stars, making their emission a reliable tracer of star formation. Interestingly, PAH features tend to be weaker or absent in AGN-dominated environments due to the destruction of these molecules by the intense radiation field of the active nucleus. The relative strengths of PAH features versus fine-structure lines such as [Ne II] or [O IV] can therefore be used to disentangle the contributions of star formation and AGN activity in composite galaxies [13, 14].

Together, the combination of AGN-related IR emission, star formation-driven IR excess, and atomic emission lines provides a comprehensive picture of the energy sources in active galaxies [5, 6, 7, 10, 11, 1, 12, 13, 14]. This multi-wavelength approach, particularly focusing on the infrared spectrum, allows astronomers to distinguish between the competing processes of accretion-driven luminosity and stellar heating, offering insights into both the central engine of AGN and the ongoing formation of stars in the surrounding galaxy.

Infrared (IR) lines play a crucial role in the diagnostic classification of active galaxies. In the case of Active Galactic Nuclei (AGN), infrared emission lines are particularly useful because they can penetrate deep into dust-obscured regions that are often inaccessible to optical or ultraviolet observations. In AGN-dominated galaxies, high-ionization IR lines, such as [Ne V] 14.3 μm and [O IV] 25.9 μm, provide powerful diagnostics for detecting AGN activity. These lines originate from gas ionized by the intense ultraviolet and X-ray radiation from the accretion disk surrounding the supermassive black hole (SMBH). As a result, they serve as robust tracers of the hard ionizing radiation field characteristic of AGN [1, 12].

In addition to the high-ionization lines used for AGN classification, low-ionization lines, such as [Ne II] 12.8 μm and [S III] 18.7 μm, are commonly observed in star-forming regions. These lines arise from the H II regions ionized by young, hot stars and are often used to distinguish starburst galaxies from AGN. When combined with mid-IR features like polycyclic aromatic hydrocarbons (PAHs), which are excited by star formation, these lines help classify the relative contributions of star formation and AGN activity in galaxies [10].

1.4. Infrared lines used for diagnostics (H_3^+, CHO^+), Star formation rate using [CII] 158μm line

Infrared lines are also crucial for probing the ionization rate of molecular hydrogen (H_2), especially in regions influenced by cosmic rays. The ionization of molecular hydrogen by cosmic rays plays a significant role in shaping the chemistry of the interstellar medium (ISM), particularly in dense molecular clouds where cosmic rays can penetrate deeper than UV photons. One of the most critical ions in this context is H_3^+ (tri-hydrogen cation), which forms when cosmic rays ionize molecular hydrogen (H_2) [15].

The H_3^+ ion is a direct tracer of cosmic ray ionization rates. Once formed, H_3^+ reacts with other molecules in the ISM, producing a variety of complex molecules. The strength of infrared lines from H_3^+ allows astronomers to measure the ionization rate of H_2 and thereby infer the intensity of cosmic rays in these regions. For example, observations of H_3^+ lines in the near-IR (around 3.7 μm) have been used to estimate cosmic ray ionization rates in the Milky Way and other galaxies [16].

The star formation rate (SFR) is a fundamental measure of the growth and evolution of galaxies. It quantifies the amount of gas being converted into stars over time, providing insights into the future evolution of galaxies and the processes driving star formation. Measuring the SFR is particularly challenging in dusty galaxies, where optical and ultraviolet light from newly formed stars is absorbed and re-emitted in the infrared by dust grains. To overcome this limitation, astronomers use tracers that are less affected by dust, with far-infrared (FIR) lines playing a key role [10].

One of the most widely used FIR tracers of star formation is the [CII] 158 μm line. The [CII] line is one of the brightest emission lines in the FIR and originates primarily from the photo-dissociation regions (PDRs), where ultraviolet (UV) radiation from young, massive stars ionizes and excites carbon atoms [17]. It can also arise from diffuse neutral gas and ionized regions, but in star-forming galaxies, the bulk of the [CII] emission is associated with star formation activity in the PDRs surrounding massive star-forming regions [12].

The [CII] 158 μm line is crucial for determining the SFR in galaxies because it traces the far-UV photons from young stars that ionize and excite the carbon atoms. In regions where massive stars are forming, these photons dominate the heating of dust grains, which leads to significant [CII] emission. Since the line is relatively unaffected by dust extinction, it provides an excellent way to measure star formation in dusty environments such as starburst galaxies and luminous infrared galaxies (LIRGs), where optical tracers of star formation are obscured by dust [1].

The calibration of the [CII] line as a tracer of SFR relies on its correlation with other star formation diagnostics, such as the total infrared (TIR) luminosity, which is a proxy for the reprocessed starlight from young stars. Studies have shown a strong correlation between [CII]

emission and the SFR across a wide range of galaxy types, from local galaxies to high-redshift star-forming systems. In particular, for galaxies with moderate to high SFRs, the [CII]-SFR relation becomes a robust diagnostic tool for measuring star formation, as it remains reliable even in heavily dust-enshrouded environments [18, 19].

However, it is important to note that the relationship between [CII] emission and SFR can be influenced by factors such as metallicity, gas density, and the strength of the radiation field. In some low-metallicity galaxies, for example, the [CII] emission may not scale linearly with SFR due to the reduced abundance of carbon in the gas phase [20]. Similarly, in regions of very intense star formation, such as ultra-luminous infrared galaxies (ULIRGs), the [CII] line may become "saturated" as other cooling mechanisms, such as CO emission, dominate. Despite these caveats, the [CII] line remains one of the most valuable tracers of SFR in the infrared, particularly in dusty or distant galaxies [21].

At high redshifts, where galaxy formation and evolution proceed more rapidly, the [CII] 158 μm line has become a cornerstone for understanding the SFR in early galaxies. In the epoch of reionization, when the first galaxies and black holes formed, the [CII] line is one of the few accessible tracers of star formation that can be observed with current infrared and submillimeter instruments such as the Atacama Large Millimeter/submillimeter Array (ALMA). Detecting the [CII] line in high-redshift galaxies allows astronomers to probe star formation at epochs when the universe was less than a billion years old, providing key insights into the formation of the first galaxies [22].

For galaxies at $z > 6$, where optical and ultraviolet emission is redshifted out of the observable range, the [CII] line remains one of the few ways to trace the star formation rate and the physical conditions of the interstellar medium (ISM). Recent observations have detected strong [CII] emission in galaxies at these high redshifts, underscoring its importance in early galaxy evolution studies [23].

1.5. Statement of the problem

Understanding the initial formation of galaxies depends on discovering sources obscured by dust and tracing these sources to their earliest epoch in the universe. The extreme luminosity

of dusty, local sources was originally revealed by the ultraluminous infrared galaxies (ULIRGs; e.g., [24, 25], whose luminosity arises from infrared emission by dust, and this dust often obscures the primary optical sources of luminosity. That such galaxies are important in the early universe was demonstrated by source modeling which indicated that the infrared dust emission from galaxies dominates the cosmic background luminosity [26, 27, 28].

Surveys in the submillimeter were the first to discover individual, optically obscured, dusty sources at redshifts z >= 2 [29]. A variety of observing programs using spectra from the Spitzer Infrared Spectrometer (IRS; [30]) subsequently found luminous ULIRGs to redshifts z~3 [31, 32, 33, 34]. This Spitzer-discovered population of high-redshift ULIRGs has large infrared-to-optical flux ratios [$f_\nu(24\ \mu m) > 1$ mJy and $R > 24$] attributed to heavy extinction by dust and has been labeled "dust obscured galaxies" (DOGs; [35]). Some DOGs are powered primarily by starbursts and some by active galactic nuclei (AGNs), and the DOGs are similar to the population of submillimeter galaxies in overall spectral energy distributions (SEDs), redshifts, and Luminosities [36, 37, 38, 39, 40].

To discover and understand dusty galaxies at even higher redshifts than the DOGs known so far, the atomic line emission of [CII] 158 μm is the single most important spectroscopic feature because it is the strongest far-infrared line [17, 41, 42, 43, 44, 45]. Consequently, this line will provide the best opportunity for redshift determinations and source diagnostics using submillimeter and millimeter spectroscopic observations. Already, [CII] has been detected at redshift exceeding 7 [46, 47] and shown to be strong in starbursts with $1 < z < 2.5$ [48, 49, 50]. The [CII] line should be a diagnostic of star formation because it is primarily associated with the photodissociation region (PDR) surrounding starbursts (SBs; [51, 52, 53, 54].

In many high-redshift sources, especially dust-obscured sources, the [CII] feature is the only diagnostic atomic emission line that can be observed. This makes it vital to optimize this line for learning about intrinsic source properties. Not only line luminosities, but also accurate line profiles, are observed. For example, the submillimeter galaxy in the group BRI 1202-0725 at z=4.7 has a [CII] full width half maximum (FWHM) of 700 km s^{-1}, measured with the Atacama Large Millimeter Array, but the associated quasar has a FWHM of only 275 km s^{-1} [22]. What can we learn from such differences?

A great amount of diagnostic information concerning the observable differences between dusty, obscured sources powered by active galactic nuclei (AGNs) and those powered by rapid star formation ("starbursts") has been acquired via the mid-infrared spectroscopy of the Infrared Spectrograph (IRS; [30]) on the Spitzer Space Telescope [55]. Classifications of AGN and starburst sources have been developed using both the strength of polycyclic aromatic hydrocarbon (PAH) features in low-resolution spectra and various emission line ratios in high-resolution spectra [56, 57, 58, 59, 60, 61, 62, 63, 64, 65] [66].

These findings underscore the critical role of far-infrared diagnostics, particularly the [CII] 158 μm emission line, in unraveling the complexities of galaxy evolution. The integration of mid-infrared spectroscopic tools, submillimeter observations, and advanced classifications has significantly advanced our ability to differentiate between AGN-driven and starburst-driven processes in dusty, high-redshift galaxies. By leveraging the [CII] line as a robust tracer of star formation and interstellar medium properties, this research provides a foundation for probing the earliest stages of galaxy formation, bridging observational gaps, and refining models of cosmic evolution. The capability to study both the physical conditions and kinematics of these distant galaxies sets a path for future explorations, further enabling the discovery of hidden populations of galaxies in the early universe.

2. [CII] 158 μm LUMINOSITIES AND STAR FORMATION RATES

Results are presented for [CII] 158 μm line fluxes observed with the Herschel PACS instrument in 112 sources with both starburst and active galactic nucleus (AGN) classifications, of which 102 sources have confident detections. Results are compared with mid-infrared spectra from the Spitzer Infrared Spectrometer and with L_{ir} from IRAS fluxes; AGN/starburst classifications are determined from equivalent width of the 6.2 μm polycyclic aromatic hydrocarbon (PAH) feature. It is found that the [CII] line flux correlates closely with the flux of the 11.3 μm PAH feature independent of AGN/starburst classification, log [f([CII] 158 μm)/f(11.3 μm PAH)] = −0.22 ± 0.25. It is concluded that the [CII] line flux measures the photodissociation region associated with starbursts in the same fashion as the PAH feature. A calibration of star formation rate (SFR) for the starburst component in any source having [CII] is derived comparing [CII] luminosity L([CII]) to L_{ir} with the result that log SFR = log L([CII])] – 7.08 ± 0.3, for SFR in M_0 yr^{-1} and L([CII]) in L_0. The decreasing ratio of L([CII]) to L_{ir} in more luminous sources (the "[CII] deficit") is shown to be a consequence of the dominant contribution to L_{ir} arising from a luminous AGN component because the sources with the largest L_{ir} and smallest L([CII])/L_{ir} are AGNs.

2.1. Introduction

Our primary motives for the present chapter are to present [CII] results for a large sample of dusty sources and to compare with mid-infrared classification indicators for starbursts and AGNs. This comparison leads to a calibration between star formation rate (SFR) and [CII] luminosity. We emphasize the diagnostics used for DOGs at z ~ 2, because the large populations of submillimeter and mid-infrared DOGs now known at this epoch provide a crucial reference for scaling to higher redshifts. The epoch $2 < z < 3$ is also important because this is the observed epoch at which starburst and AGN activity seems to peak [67, 68, 69, 70, 71].

The [CII] line should be primarily a diagnostic of star formation, being associated with the photodissociation region (PDR) surrounding starbursts [51, 52, 53, 54], and the line appears

to be weaker in the most luminous sources ("the [CII] deficit"; [41]). It is crucial to understand the origin of this line and the extent to which its luminosity is a measure of SFR. Does [CII] scale with other star formation indicators? Is the [CII] deficit a consequence of AGN dominance rather than star formation in luminous sources?

Determining such answers was the objective of new observations with the Herschel Space Observatory [72].

2.2. Observations

2.2.1. Selection of Sources

Using the Herschel PACS instrument [73], it was possible to measure efficiently the [CII] luminosity in luminous, dusty galaxies within the local universe. The Herschel PACS observing program OT1dweedman1 included 112 sources chosen to connect the [CII] results to various mid-infrared diagnostics of starburst and AGN activity that can be derived from spectroscopic observations with the Spitzer IRS.

Our source list was assembled using these criteria. (1) All targets have complete low-resolution and high-resolution mid-infrared spectra from 5 μm to 35 μm with the Spitzer IRS; low-resolution spectra are available in the Combined Atlas of Spitzer IRS Spectra (before: Cornell Atlas of Spitzer IRS Spectra) (CASSIS; https://cassis.sirtf.com/ [74]). (2) All targets have complete fluxes from the Infrared Astronomical Satellite (IRAS) so the total infrared luminosities L_{ir} can be determined with the relation of [25]. (3) Finally, all targets are spatially unresolved (according to estimates described below) to give confidence that IRS and Herschel spectroscopy measure the same source. These selection criteria do not include any source classification criteria; the criteria derive only from selection based on available archival observations.

The 112 sources in the observing program are taken from the 301 sources in [64] by proceeding as follows. That list was produced starting with all IRS archival observations then available having both IRS low-resolution spectra and complete flux measures with IRAS, giving a sample of 501 sources. To exclude extended sources for which IRS and IRAS flux

comparisons would not be the same, the total f_ν (IRAS 25 μm) was compared to the f_ν (IRS 25 μm) measured with the 10" slit of the IRS to define a list of 301 sources estimated to be unresolved see Figure 2 in [64] and the accompanying discussion). The resulting sample has $0.004 < z < 0.34$ and $42.5 < \log L_{IR} < 46.8$ (erg s^{-1}) and covers the full range of starburst galaxy and AGN classifications.

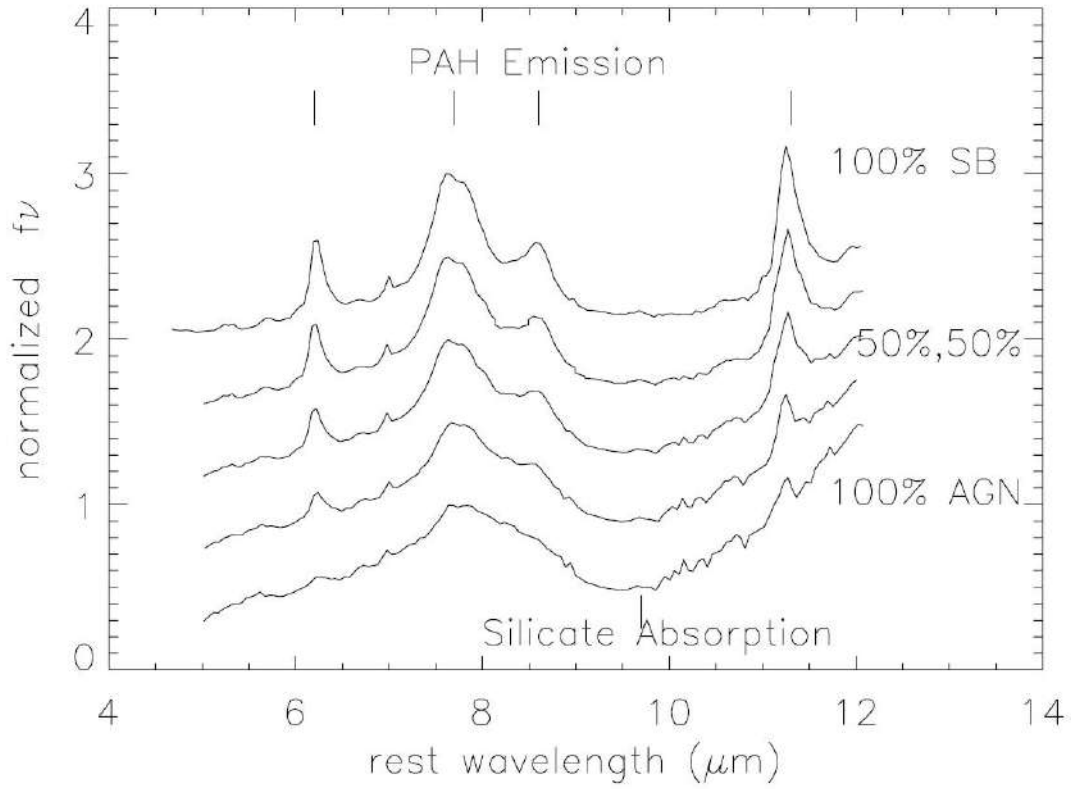

Figure 2-1. Transition in mid-infrared spectra from pure starburst to pure absorbed AGN. Top spectrum is median observed rest-frame IRS spectrum of 51 starburst PAH emission sources (100% starburst) from samples in [64]; bottom spectrum is median observed rest-frame IRS spectrum of 65 AGNs with silicate absorption (100% AGN; from the same reference); intermediate spectra show mixes of top and bottom spectra, changing mix by 25% in each spectrum. Spectra are normalized to peak fv (7.8μm) and displaced by 0.5 units of f_ν.

Of these 301 sources, 182 also have IRS high-resolution spectra in addition to the low-resolution spectra. At the time of the PACS OT1dweedman1 proposal, 41 of these 182 had PACS observations listed either in the Herschel Reserved Observations Search Tool (30

sources) or archival [CII] data from Infrared Space Observatory (ISO; 11 sources; [42]. Of the 141 remaining sources, we selected for new PACS [CII] observations the 123 brightest as measured by IRS flux of the 11.3 μm polycyclic aromatic hydrocarbon (PAH) feature. Subsequently, 11 of these 123 were yielded to program OT1dfarrah1, giving our final sample of 112 sources. These are the results we report in the [75] paper. We also include for comparison the prototype ULIRG Markarian 231 using the PACS [CII] flux from [76] and IRS data from [64] because this important source satisfies all of our sample selection criteria.

Having IRS low-resolution and high-resolution spectra for all sources means that many comparisons can be made with various mid-infrared diagnostic features, including several atomic and molecular emission lines, silicate absorption and emission, and the dust continuum. In future papers, we will present comparisons with emission line fluxes, velocities, and profiles. For the present analysis, our goal is only to compare the [CII] results to PAH molecular emission features. The PAH features are the most important diagnostics for classifying dusty, luminous starbursts, and AGNs at $z \gtrsim 2$, as described below in Section 2.2.2 and illustrated in Figure 2-1. They are also the most important mid-infrared measure of SFR. By relating [CII] to PAH, the populations of DOGs already known at $z \sim 2$ can be compared with sources at even higher redshifts when such sources are observed using [CII].

2.2.2. Classification of sources

To understand the ultimate luminosity source, it is necessary to distinguish starbursts and AGNs. The most important mid-infrared spectroscopic criterion for classification is the broad complex of PAH emission (Figure 2-1) which arises within the PDR surrounding starbursts [77]. That PAH emission is weak in AGNs compared to starbursts was initially demonstrated observationally by [78] using spectroscopy with the ISO. The strength of a PAH feature compared to the underlying continuum (the equivalent width, EW) decreases as the AGN component increases because the continuum beneath the PAH feature increases in proportion to the hot dust heated by the AGN.

Spectra for hundreds of sources with the IRS quantified the dependence of PAH strength on starburst/AGN classification determined from optical spectra [56, 61, 64]. These comparisons with optical classifications led to an infrared classification derived from EW (6.2 μm), measured as described below. The continuous gradation of EW (6.2 μm) provides a single parameter, the quantitative measure of the starburst/AGN mix. We use the EW (6.2 μm) for classification rather than the stronger 11.3 μm PAH feature because the 11.3 μm feature is near the long wavelength limit of the IRS for $z >\sim 2$, and we also want to apply the classification at high redshifts.

The PAH spectroscopic emission features are complex (Figure 2-1), including an underlying plateau between 5 μm and 10 μm, a maximum at rest-frame ~7.7 μm, and specific features at 6.2 μm and 11.3 μm. Features are broad and blended, and the "continuum" beneath the features includes wings of other PAH emission features. Sophisticated measures of PAH strengths require various assumptions about the underlying dust continuum and relative feature strengths to deconvolve the full, broad PAH features into different components [13]. This deconvolution is uncertain when using observations of faint sources with poor signal-to-noise ratios (S/Ns) and limited coverage of rest-frame wavelengths, as arises for the highest redshift sources with IRS spectra.

To avoid such uncertainties, we use simple parameters for PAH strength that allow consistent, model-independent observational measures that are possible even with weak features or poor S/Ns. These measures are made with the SMART software for IRS spectra [79] and are (1) the EW (6.2 μm) determined using a Gaussian fit to the PAH feature and a linear fit to the continuum beneath the feature within the range 5.5 μm to 6.9 μm; (2) the total flux of the 11.3 μm feature, f(11.3 μm), determined with a Gaussian fit to the PAH feature and a linear fit to the continuum beneath the feature from 10.5 μm to 12 μm. Measurements are given in [64].

Although the range of EW (6.2 μm) is continuous among spectra, comparisons with optical classes show consistent divisions. The initial study of IRS spectra for 22 optically classified starbursts showed that 21 of 22 sources have rest-frame EW (6.2 μm) > 0.4 μm [56]. Subsequent studies confirmed this result and also determined an EW limit for optically

classified AGNs. Of the 19 sources with EW (6.2 μm) > 0.4 μm having optical classifications in the f_ν(24 μm) > 10 mJy sample of [61], 18 are classified as starbursts; of the 17 sources with EW (6.2 μm) < 0.1 μm, 16 are classified as AGNs. The distribution in [64] is illustrated in their Figure 4, where 14 of 17 sources having both EW (6.2 μm) > 0.4 μm and optical classifications are starbursts, and 42 of 57 having EW (6.2 μm) < 0.1 μm are AGNs. Using these results, we have adopted the criteria that AGNs have EW (6.2 μm) < 0.1 μm, composite sources have intermediate 0.1 μm < EW (6.2 μm) < 0.4 μm, and starbursts have EW (6.2 μm) > 0.4 μm. (Observed frame EWs are greater by a factor of (1 + z) compared to rest-frame EWs.)

This empirical observational classification is quantitatively consistent with starburst/AGN luminosity fractions when synthetic spectral combinations of mid-Infrared spectral templates are assumed. Using the mixes of observed starburst and AGN spectra shown in Figure 2-1, for example, the dependence of EW (6.2 μm) on the fractional AGN contribution to the mid-infrared luminosity is shown in Figure 2-2. With this mix of spectra, >90% of the mid-infrared luminosity arises from a starburst if EW (6.2 μm) > 0.4 μm, confirming that this value of EW (6.2 μm) defines a starburst. The majority of the mid-infrared luminosity, >55%, arises from an AGN if EW (6.2 μm) < 0.1 μm. In fact, most AGNs in the present paper actually have EW (6.2 μm) < 0.01 μm for which > 90% of the luminosity arises from an AGN in Figure 2. Composite sources have contributions from both starburst and AGN. The boundaries illustrated in Figure 2-2, therefore, are those used to define classification symbols in those figures below which do not display a quantitative EW (6.2 μm).

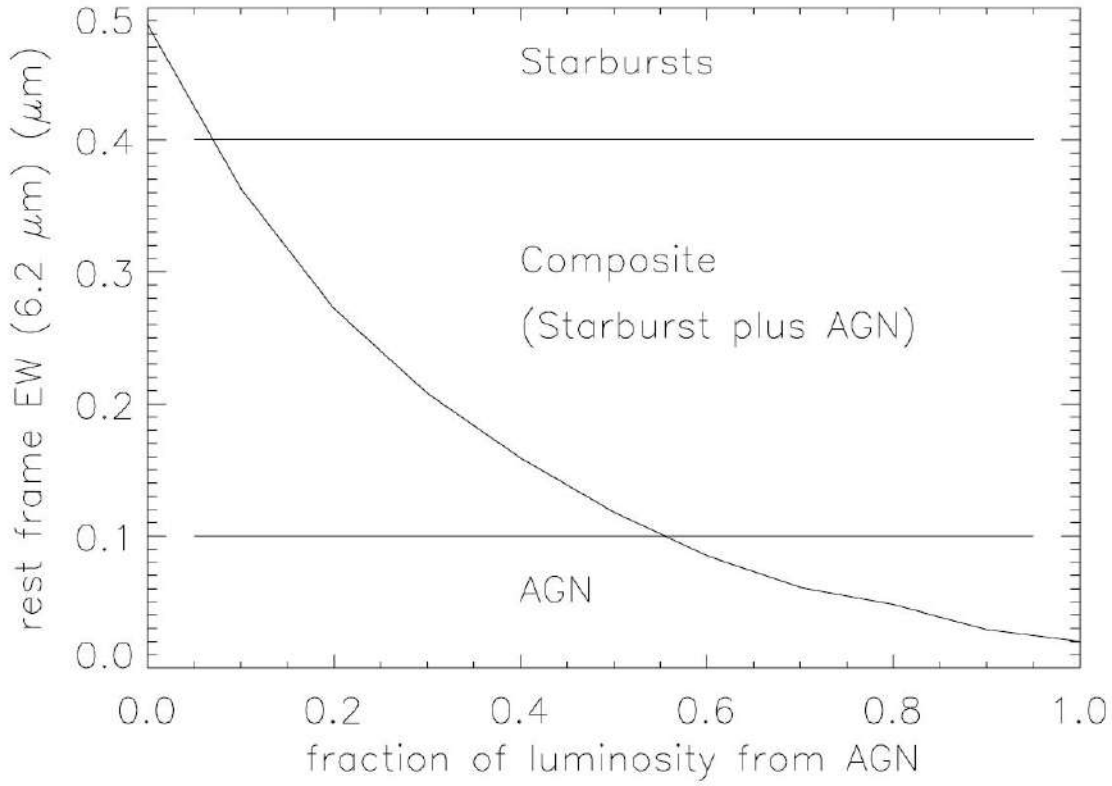

Figure 2-2. Equivalent width in μm of 6.2 μm PAH emission feature shown in Figure 2-1 compared to a fraction of total luminosity at 7.8 μm which arises from AGN component. Curve derives from various mixtures of the "100% starburst" and "100% AGN" spectra shown in Figure 2-1. Criteria for EW (6.2μm) used to classify Herschel sources in the remaining figures are illustrated.

2.2.3. Observations and [CII] Measurements

All [CII] observations were made using PACS line spectroscopy in point-source chop nod mode with medium throw. A single repetition cycle was used for all but 20 sources, giving total observing time for the program of 20.2 hr for 112 sources. Table 1 in [75] includes results for the 112 sources. Data reduction was done with version 8 of the Herschel Interactive Processing Environment, together with the "PACSman" software [80] used for fitting line profiles and continuum within each of the 25 equivalent spatial pixels, or "spaxels" produced by the PACS image slicer (pacs_om.pdf). Illustrations of these fits are in Figure 2-

3, with examples of both high and low S/N sources, together with an example of a source with an unusually broad line profile.

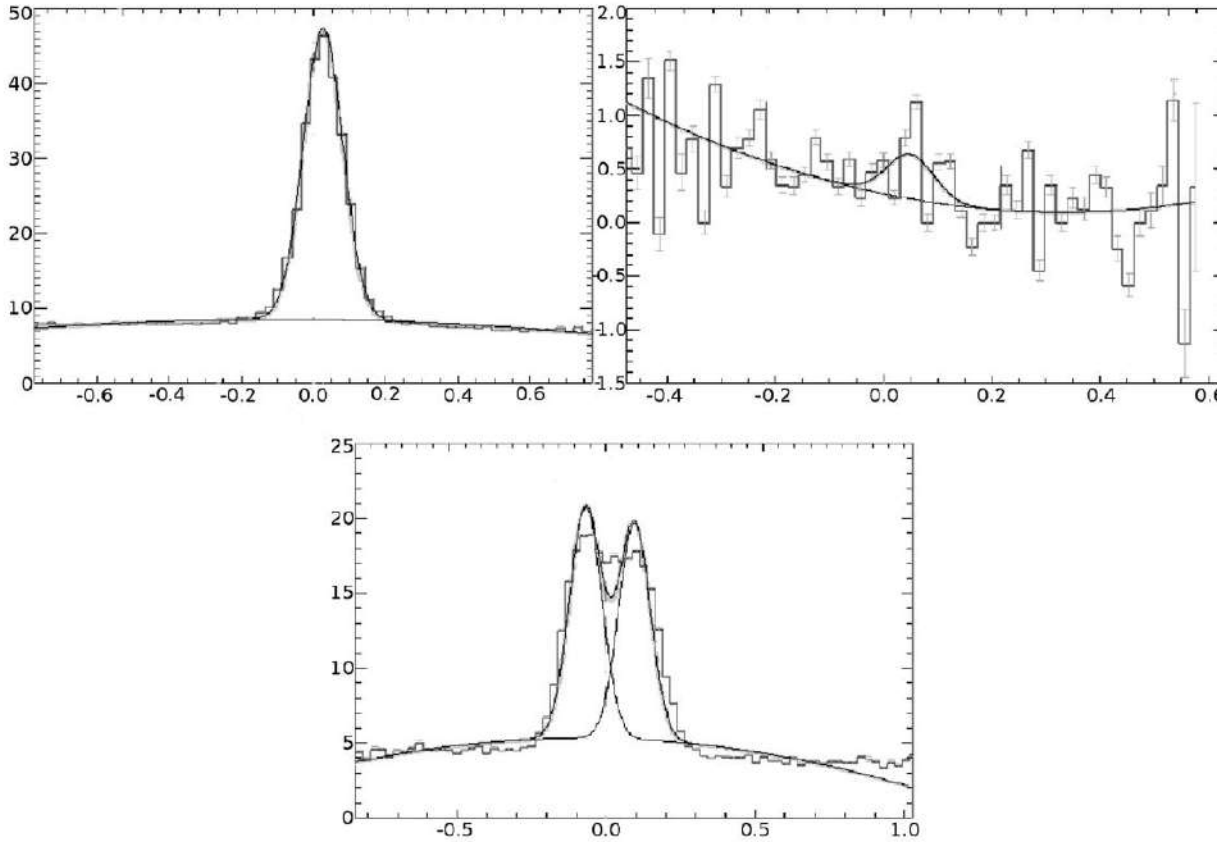

Figure 2-3. Examples of line fits in the brightest spaxel for three sources in Table 1 of [75]. Vertical axes are flux density in Jy; horizontal axes are wavelength differences in μm from [CII] rest wavelengths derived using redshifts in Table 1. Upper left panel (source 28 in Table 1) is a high S/N detection for which the line flux derives from the Gaussian fit shown; upper right panel (source 92 in Table 1) is an upper limit; lower panel (source 83) is a complex, broad profile for which the line flux is the total integrated flux within the wavelength bounds of the two profiles shown. [C II] line fluxes in Table 1 are the sum of the brightest spaxel plus the 8 surrounding spaxels, increased by a correction factor of 1.16–1.21 (depending on redshift) to include the flux from an unresolved source that would fall outside these 9 spaxels.

We include a line detection as real if the S/N for the line profile fit in the brightest spaxel exceeds 3. If S/N < 3 for the line flux in the brightest spaxel, we adopt an upper limit for

the total line flux. Of our 112 sources, 102 are detected according to this criterion. All results are in Table 1.

One method for measuring total source fluxes with PACS is to take only fluxes in the brightest, central spaxel and correct to total flux assuming an unresolved source that is perfectly centered in the central spaxel. In this case, the flux from the central spaxel is corrected by a factor of 1.95 at wavelength 160 μm to determine the total flux. The greatest uncertainties in this technique are the requirement of perfect centering and the possibility that sources are extended.

To minimize centering uncertainties and to maximize the inclusion of total flux, the procedure we adopt instead for measuring detections is to measure the total line flux in the brightest spaxel plus the 8 surrounding spaxels, f(3 × 3). (For detected sources, we find that the brightest spaxel is always the central spaxel, except for four cases where it is displaced by one spaxel, noted in Table 1) The f(3 × 3) covers a spatial area of 28" by 28". Calibration communicated to us by the PACS calibration team gives the result that the f (3 × 3) should be corrected by a factor 1.16 to give the total flux at 160 μm for an unresolved source that is precisely centered. This correction is slightly wavelength dependent, increasing to a maximum correction of 1.21 for our highest redshift source, for which the [CII] line is observed at 212 μm.

To list the total fluxes of detected sources, therefore, we correct f(3 × 3) to include flux outside these spaxels by taking values between 1.16f(3 × 3) and 1.21f(3 × 3) as the total source line flux, depending on the observed frame wavelength according to the formula given in the footnote to Table 1. These corrected f(3 × 3) are the values listed in Table 1 for the total [CII] line flux.

These two alternative measures of total line fluxes from the brightest spaxel and from f(3×3) are compared in Figure 2-4. This comparison illustrates empirically the large error that can arise from imperfect centering if using only the brightest spaxel. The plot compares the single brightest spaxel corrected by a factor of 1.95 with the sum of the 9 spaxels corrected by 1.16. The limiting ratio for these corrected fluxes should be unity (log = 0 on vertical axis) for a perfectly centered point source, and several sources satisfy this value. Small

centering uncertainties have little effect within the large area of the f(3 × 3) flux, so the scatter in 1.16f (3 × 3)/1.95f(brightest) primarily demonstrates the uncertainty arising when using only the brightest spaxel to determine total flux. The vertical dispersion of the points and the dominance of values above unity can be explained by slight differences in source centering within the brightest spaxel. (To simplify this illustrative calculation, we apply no wavelength dependence for different redshifts to the correction factors for Figure 2-4 because such differences are small compared to the centering uncertainties.)

For example, in the extreme case of a source being offset 5" in a direction such that the centering is on a spaxel corner, the “brightest spaxel” would be shared evenly among 4 spaxels. In this extreme example, the brightest spaxel would have 1/4 of the flux within the 4 spaxels, or within encircled energy of radius 10" (taken as 72% of the total flux for an unresolved source), so the brightest spaxel has 18% of the total source flux. For this extreme case of sharing the brightest spaxel among 4 spaxels, therefore, the correction to total flux derived only from the brightest spaxel should actually be a factor of 5.6 and not a factor of 1.95, so the corrected total flux from the brightest spaxel alone if corrected by 1.95f(brightest) would be erroneously faint by a factor of 2.9. This extreme case is shown as the upper line in Figure 2-4. Intermediate centering of an unresolved source within the brightest spaxel would lead to values anywhere between the upper and lower lines in Figure 2-4, so centering uncertainties alone of $<\pm 5$" could explain the dispersion of all points in Figure 2-4, except for the one source falling above the upper line.

Extended sources would also have ratios above unity in Figure 2-4, and it is not possible to determine from this ratio alone whether a source is unresolved but not perfectly centered, or whether the source is slightly extended. A diffuse source so extended that it evenly fills the central 3 × 3 spaxels (so each of these 9 spaxels has the same flux as the brightest spaxel) would have log[1.16f (3 × 3)/1.95f(brightest)] = 0.73, but no sources show this extreme ratio. This is proof that no sources are extended as large as 30".

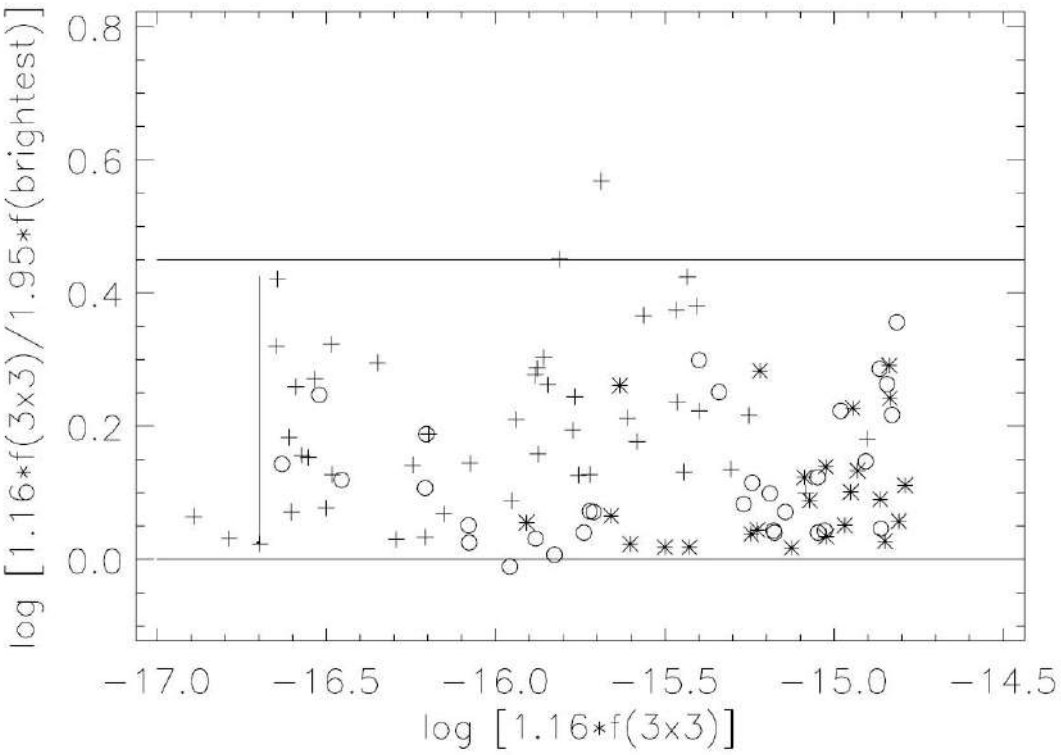

Figure 2-4. Vertical axis compares total corrected [CII] source flux derived from observed flux in 3 × 3 spaxels compared to corrected flux derived only from the brightest spaxel; both observed measures are corrected for fractional flux that would fall outside of those spaxels for a perfectly centered, unresolved source, using corrections of 1.95f(brightest) and 1.16f (3×3) at 158μm (small changes in corrections because of different redshifts are ignored in this ratio comparison). Horizontal axis is corrected total [CII] flux 1.16f (3×3) in Wm^{-2}. The 102 detected sources in Table 1 are shown as crosses for AGNs, open circles for composite AGNs plus starbursts, and asterisks for starbursts (all using the EW (6.2μm) classification discussed in Section 2.1). Vertical line defines flux upper limit for the 10 undetected sources in Table 1. Upper horizontal line is the maximum value of ratio 1.16f (3 × 3)/1.95f(brightest) that can arise for an unresolved source because of imperfect centering; sources above this line must be extended. Lower horizontal line is ratio of unity expected for a perfectly centered unresolved source.

Further evidence that most sources are unresolved is the similar distribution in ratio 1.16f (3 × 3)/1.95f(brightest) between starbursts and AGNs. If some sources are extended, they

should be extended starbursts instead of unresolved AGNs, but starbursts show no more extension to large ratios than do the AGN. The consequence to our analysis of having some marginally resolved sources would be that the total [CII] flux is erroneously large compared to PAH, because the PAH measure derives from IRS measures calibrated for unresolved sources. When comparing the [CII]/PAH ratio below in Section 2.3.2, however, the only three sources with [CII]/PAH ratios significantly above the dispersion are three AGNs, and none of these three show any evidence of spatial extent in the PACS images.

Figure 2-4 also illustrates how upper limits for non detections are determined. The detection limit for our sample is at log f([CII] 158 μm) ~ –16.7 in units of W m^{-2}. This value is taken as the upper limit of [CII] line flux for the 10 sources which are not detected, according to our criterion of S/N < 3 in the brightest spaxel.

2.3. Analysis and Results

In the present analysis, the mid-infrared spectroscopic features used for comparisons to [CII] line luminosities are the PAH emission features at 6.2 μm and 11.3 μm. These values are tabulated by [64] measured as described above in Section 2.2.1. The 11.3 μm PAH is used as the PAH flux measurement for comparison with [CII] because this feature is detected in all but two of our sources, whereas the 6.2 μm feature is only a limit in 25 sources. The EW (6.2 μm) is used only for source classification, and all sources with limits for EW (6.2 μm) have classification as AGN because of the weak 6.2 μm PAH.

2.3.1. Comparison of PAH and [CII]

Photoionization and photoelectric heating models for [CII] [81, 53, 82, 17] in comparison with previously available observations [41, 21, 49] indicate that [CII] emission arises primarily in PDRs, with ionization produced by the hot stars of the adjacent HII region. Although [CII] can arise in any region with singly ionized carbon and sufficiently energetic electrons

for collisional excitation, the level of ionization seems the most important parameter for line strength; models show a weakening of [CII] if the ionization parameter increases, resulting in a diminishing of the PDR compared to the HII region. This could be the result of harder ionization either from AGNs or from unusually hot stars in compact, young starbursts.

Comparisons of 6.2 μm PAH and [CII] using ISO results showed overall consistency between the two measures of PDRs but discussed various reasons why detailed agreement is not expected [52, 41]. Models as well as Herschel observations of spatially resolved [CII] emission regions and Galactic PDRs show that detailed relations are complex [83, 80, 84, 85] but generally confirm that [CII] emission arises primarily in the PDR and scales with the PAH [86].

For our sample, the objective is an empirical observational comparison to determine how the observed [CII] and PAH fluxes scale together when integrated over many star-forming regions throughout many sources. Such scaling would be an indication that the [CII] luminosity can be used as a quantitative measure of PDRs and SFRs in the same fashion as the PAH luminosity can be used [77] and thereby allow reliable use of [CII] as a star formation indicator. The large sample of sources enabled by the new Herschel observations can also determine the cosmic dispersion in this comparison and the extent to which the differences in [CII]/PAH ratios seen on small scales within starburst galaxies [87] average out when integrated over entire starburst systems.

Figure 2-5 compares the [CII] total line flux, f([CII] 158 μm), with the 11.3 μm PAH feature, f(11.3 μm PAH), as a function of the source classification from EW (6.2 μm). Figure 2-6 shows the [CII]/PAH ratio compared to total infrared luminosity $L_{ir.}$ (For comparison, the ground-based measurement of [CII] for the source at z = 1.3 from [48] is also shown in Figure 2-5 because this source has an IRS spectrum allowing PAH measurement; this source has a higher redshift than any of our PACS sources.) Also shown for comparison in these and subsequent figures is the prototype local ULIRG Markarian 231 using [CII] fluxes from [76] and PAH measures from [64], because this source satisfies our selection criteria.

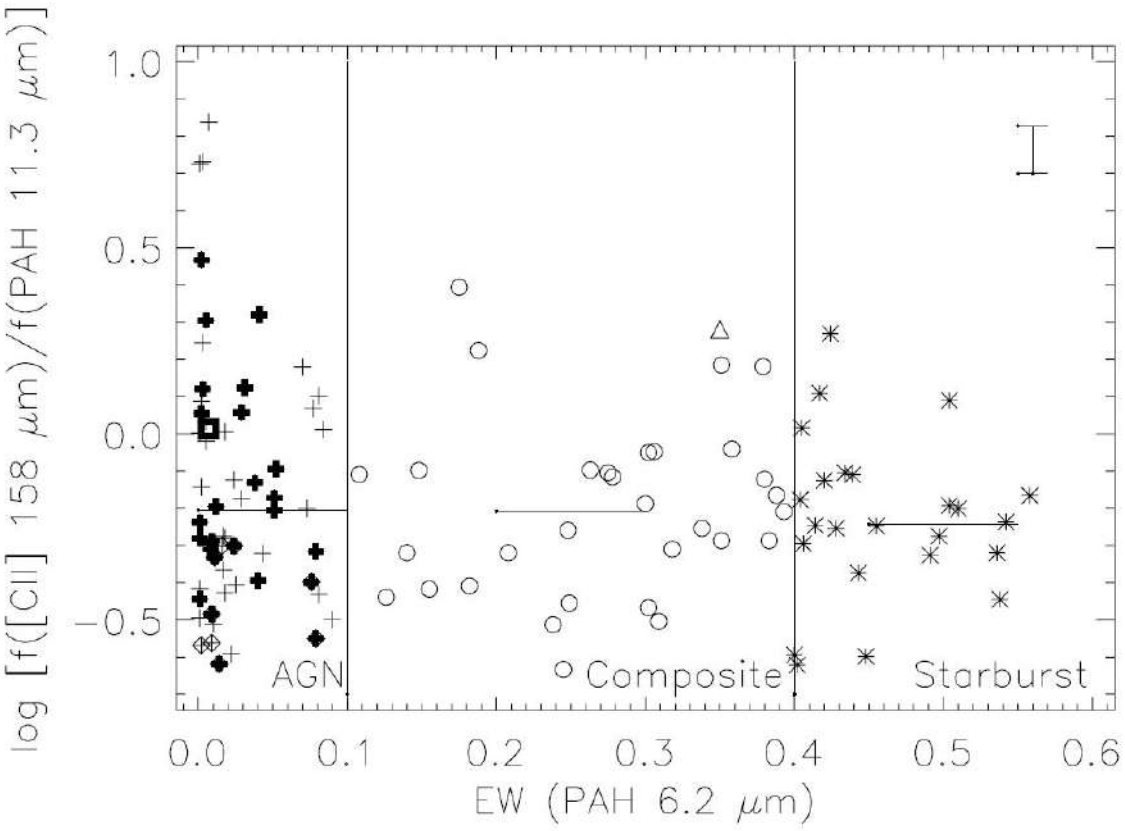

Figure 2-5. Ratio of [CII] to PAH 11.3μm line fluxes, compared to source classification from EW (PAH 6.2μm) measured in μm. Crosses are AGNs from the EW classification (discussed in Section 2.2.1); thick crosses are those sources with silicate absorption in IRS spectra noted in [64]. Open circles are composite AGNs plus starbursts, and asterisks are starbursts. Sources with diamonds (all AGNs) are upper limits to [CII] line fluxes in Table 1 of [75]. Triangle is the source at z = 1.3 from [48]. Square is Markarian 231 using [CII] flux from [76]. Horizontal bars are medians within each category; medians include limits because all limits fall below the median. Vertical error bar shows the observational uncertainty for individual points assuming flux uncertainties of ±12% for f([CII]) and ±10% for f(PAH 11.3μm).

Figure 2-5 shows the important conclusion that the [CII] to PAH ratio is independent of starburst/AGN classification. The median ratios for all classes are the same. Figure 2-6 shows that the ratio does not depend on source luminosity. The overall median and dispersion for all sources is log [f([CII] 158 μm)/f(11.3 μm PAH)] = –0.22 ± 0.25. This scatter is a measure of the cosmic dispersion in the comparison of [CII] and PAH when integrated

fluxes that include entire, unresolved collections of starbursts are observed. This dispersion is independent of AGN/starburst classification which implies that the dispersion is a measure of variances within the starbursts.

Because the PAH luminosity is determined by the starburst, this result means that the [CII] line flux also depends only on the starburst component of the source, regardless of the fractional starburst/AGN mix. This result indicates that [CII] luminosity can be used as a measure of starburst luminosity with as much reliability as PAH, because [CII] is a measure of the same PDRs as is the mid-infrared PAH. The [CII] luminosity measures SFR in any source for which [CII] is observed, even if the source luminosity is dominated by an AGN.

A question about the use of the 11.3 μm PAH feature for flux measures is whether this feature might be affected by silicate extinction in sources showing strong silicate absorption as in Figure 2-1, because the PAH feature falls within the broad silicate absorption centered at 9.7 μm. The silicate absorption is always associated with AGN classification and is attributed to thick dust clouds close to the AGN (e.g., [88, 89]. An important question about the geometry of these absorbing clouds is whether they also surround the starburst regions. The [CII] results allow a test of this. If the starbursts are affected by the same silicate absorption that affects the AGN, then the f([CII] 158 μm)/f(11.3 μm PAH) ratio should be systematically larger in sources with silicate absorption because the [CII] is not affected by the silicate absorption feature.

These absorbed sources are noted in Table 1 of [75] and shown in Figure 2-5, where it is seen that there is no systematic difference in the ratio for the absorbed AGNs compared to the emission AGN. Formally, the median for the absorbed AGNs is log [f([CII] 158 μm)/f(11.3 μm PAH)] = –0.23 and is –0.18 for the emission AGNs, which is opposite to what would arise if the absorbed AGNs have suppressed 11.3 μm PAH. (The AGN median shown in the figure is for all AGNs.) Based on this observation, we conclude that the 11.3 μm PAH feature arises outside of the region affected by silicate absorption, so this feature has the same reliability for measuring starburst PDRs regardless of the presence of silicate absorption.

Among all of the sources in Figures 2-5 and 2-6, only three appear anomalous. These are all AGNs and have the largest f([CII])/f(PAH) ratios—sources 3C 120, Mrk 590, and NGC

3393 in Table 1—with f([CII])/f(PAH) about a factor of 10 greater than the median. All have strong and reliable [CII] detections with no unusual profiles or evidence of spatial mismatches or source extension. The PAH 11.3 μm feature is weak in all three, but independent CASSIS spectra yield fluxes consistent to within ~30%, so there is no indication that the anomalous weakness of PAH is a measurement error. All are silicate emission sources, so the anomalies cannot be explained by silicate absorption associated with the AGN. These are the only sources among the 112 sources in all categories with excess [CII] luminosity compared to PAH. Why are the ratios so unusual in these three sources?

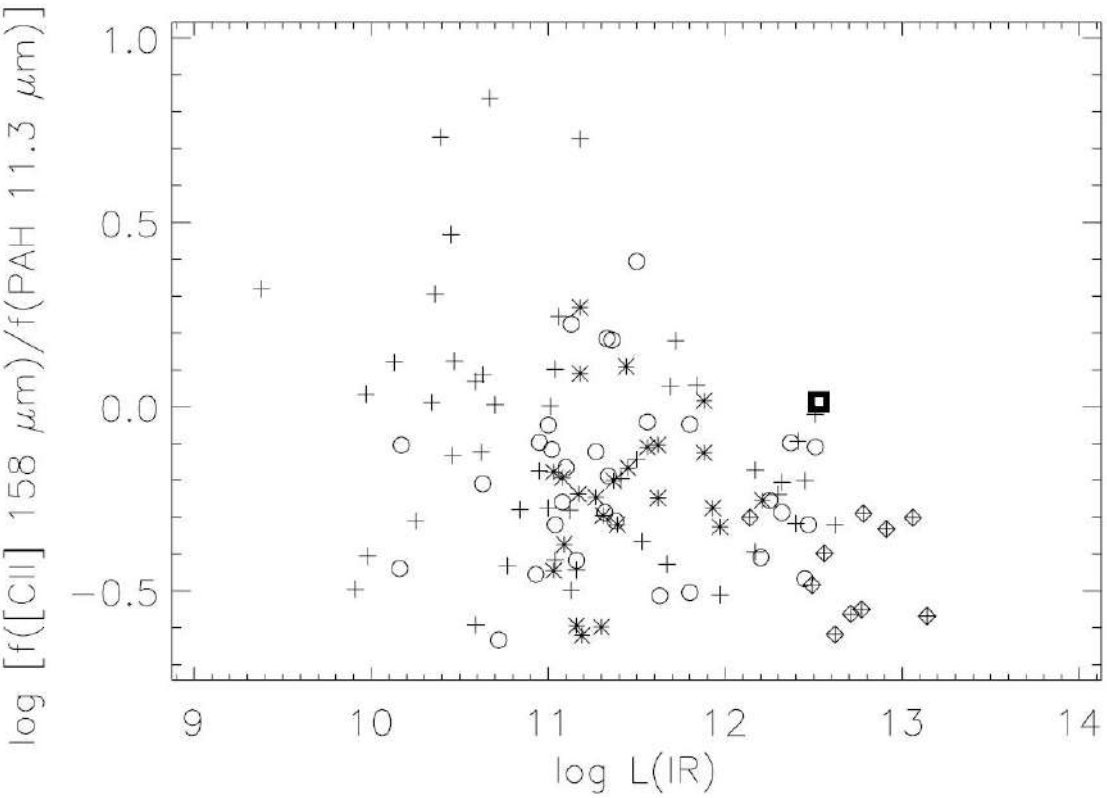

Figure 2-6. Ratio of [CII] and PAH 11.3μm line fluxes, compared to total infrared luminosity L_{ir} in $L_{\odot}$. Crosses are AGNs from the EW classification, open circles are composite AGNs plus starbursts, and asterisks are starbursts. Sources with diamonds (all AGNs) are upper limits to [CII] line fluxes in Table 1. Square is Markarian 231.

There are various possible explanations. One possibility is that an unusual combination of radiation hardness and ionization parameter, caused by geometry, density distributions, or

ionizing spectrum, causes PAH emission in the PDR to be suppressed while maintaining [CII] within the HII region [41]. An alternative possibility could be that the PAHs are weak because of star formation taking place in dense clouds which are so obscured that the mid-infrared PAH from the starburst PDR suffers significant extinction compared to the far-infrared [CII]. Because the AGN is not absorbed, such clouds would require a small filling factor or geometric placement outside of the observer's line of sight to the AGN. In this circumstance, we would expect mid-infrared emission lines associated with any obscured starburst, such as [NeII] 12.8 μm, also to be unusually weak compared to [CII], and would also expect to observe excess far-infrared continuum from the obscured starbursts.

2.3.2. Star Formation Rate from [CII]

For eventual application to high-redshift, dusty sources in which [CII] measurements with ALMA or other submillimeter/millimeter spectroscopy are the primary diagnostic, calibration of [CII] luminosity to SFR is our most important objective. The conclusion reached above, that [CII] luminosity L([CII]) measures the PDRs arising from star formation, encourages the calibration of SFR compared to L([CII]).

Determining the SFR for dusty sources ultimately traces back to the method of [10], in which the total infrared luminosity L_{ir} is attributed to reradiation by dust of the primary stellar luminosity from the starbursts. The original calibration is log SFR = log L_{ir} – 9.76, for L_{ir} in $L_{\odot}$. We adopt the updated calibration in [90], giving log SFR = log L_{ir} – 9.97. All of our sources have L_{ir} listed in [64] determined using the formulation in [25], described in the footnote to Table 1. This L_{ir} is an estimate of the complete 8 μm to 1000 μm luminosity derived from all four IRAS bands.

By comparing L_{ir} to L([CII]) for starbursts, a calibration can be determined between L([CII]) and SFR. It is necessary to assure that L_{ir} arises only from a starburst and is not contaminated by an AGN component. Figure 2-7 compares the ratio L([CII])/L_{ir} depending on source classification. The medians seen in this figure trend as expected if L([CII]) measures only

the starburst component but L_{ir} arises from both starburst and AGN components. As the contribution to L_{ir} arising from AGN luminosity increases compared to the L([CII]) arising from starburst luminosity, the ratio L([CII])/L_{ir} systematically decreases for AGNs (this is discussed further in Section 2.3.3 in context of the CII deficit). To calibrate SFR to L([CII]) using L_{ir}, AGNs and composites in Figure 2-7 are not used because some fraction of the L_{ir} arises from AGNs.

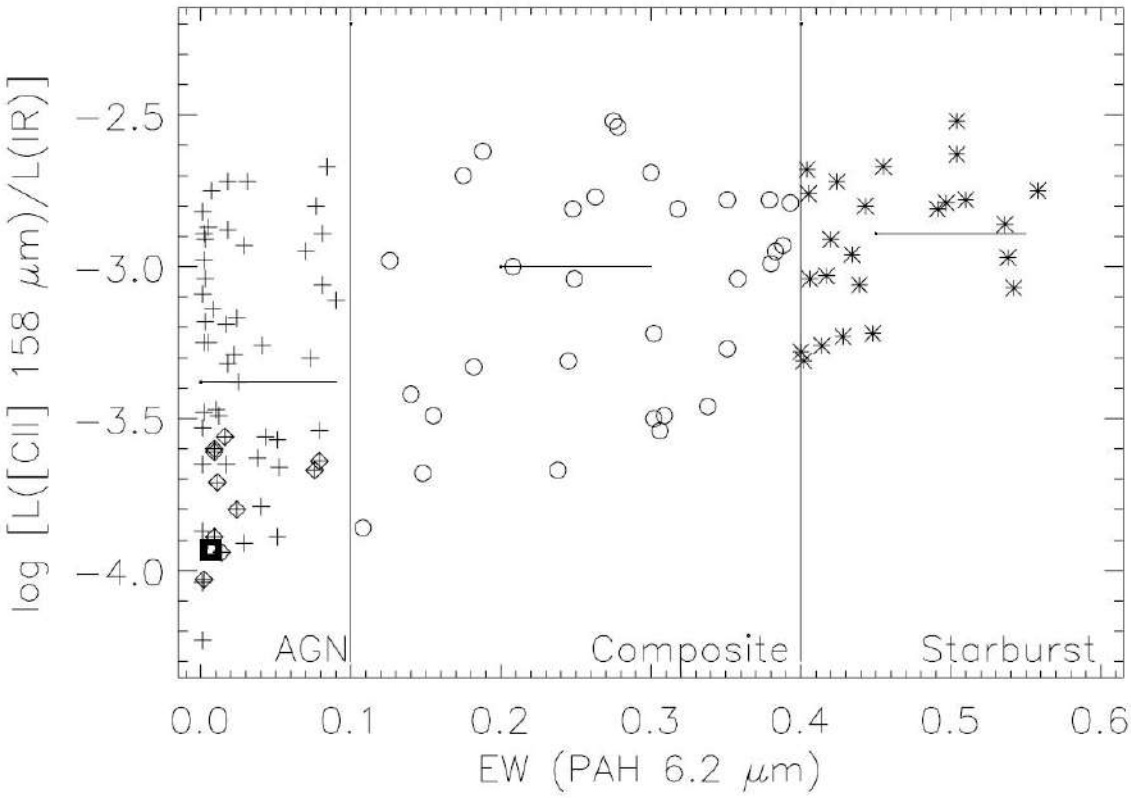

Figure 2-7. Ratio of [CII] luminosity L([CII]) to total infrared luminosity L_{ir}, compared to source classification from EW (PAH 6.2μm) measured in μm. Crosses are AGNs from the EW classification, open circles are composite AGNs plus starbursts, and asterisks are starbursts. Sources with diamonds (all AGNs) are upper limits to [CII] line fluxes in Table 1. Square is Markarian 231. Horizontal bars are medians within each category; medians include limits because all limits fall below the median. Median for starbursts is used in the text to calibrate L([CII]) compared to star formation rate, giving log SFR = log L([CII])] – 7.08±0.3, for SFR in M_0 yr^{-1} and L([CII]) in L_0.

For starbursts only in Figure 2-7, the observed median ratio log L([CII])/L_{ir} = –2.89. This gives the calibration log SFR = log L([CII)]) – 7.08 ± 0.3, for SFR in $M_\odot$ yr^{-1} and L([CII]) in $L_\odot$. The uncertainty arises from the 1σ dispersion among the starburst points shown in Figure 2-7. This result is our SFR calibration. Taken with the conclusions from Figures 2-5 and 2-6, that L([CII]) scales with the starburst component in all sources, this calibration can be applied to any source in which [CII] is measured.

The resulting measures of SFR are shown in Figure 2-8. The results show that the greatest SFRs are in sources with a starburst classification from EW (6.2 μm) even though these sources do not have the most luminous L_{ir}. For example, among sources with log SFR > 1.8, six are starbursts, three are composites, and only two are AGNs (not counting upper limits). This preponderance of starbursts is even greater when compared to the sample sizes; this high SFR includes 6 of 24 starbursts, 3 of 31 composites, and only 2 of 55 AGNs. The dominance in SFR by starbursts arises despite the fact that the largest L_{ir} ($L_{ir} > 10^{12}$ $L_\odot$) are dominated by AGNs. The maximum SFR in this sample is ~100 $M_\odot$ yr^{-1}, about a factor of 10 less than in the most luminous starbursts at z ~ 2 with SFR measured using PAH luminosity [91].

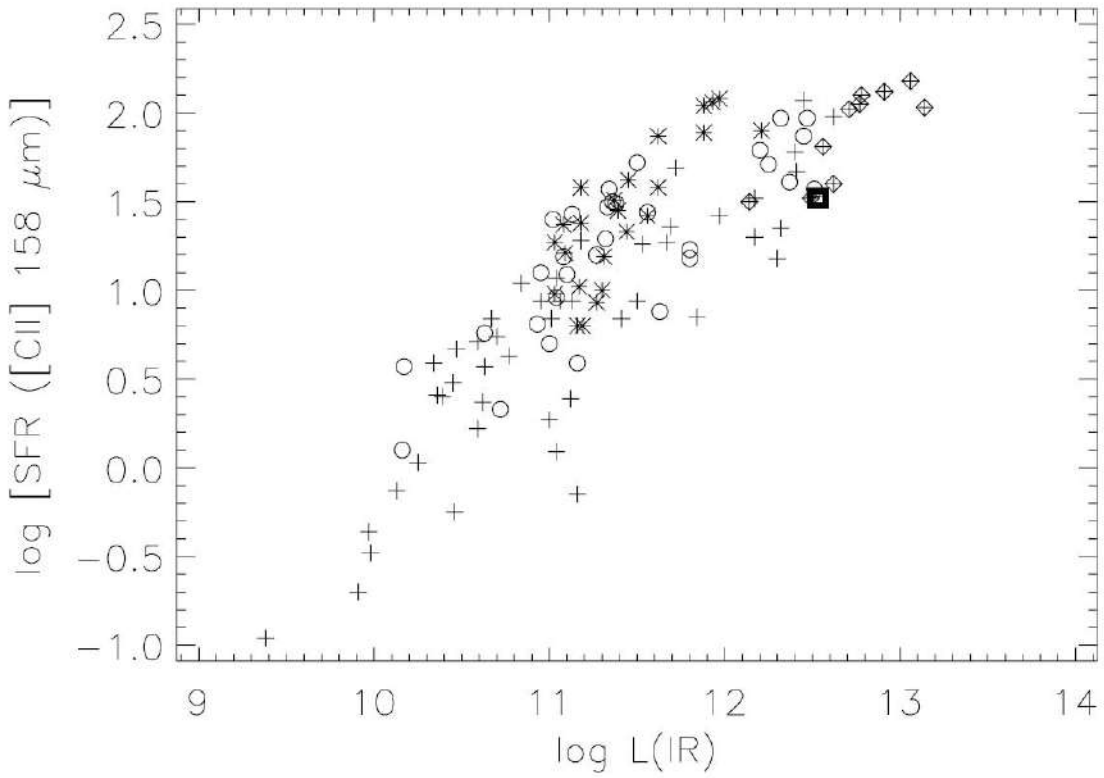

Figure 2-8. Star formation rate in all sources in $M_\odot$ yr^{-1} measured using L([CII]) to SFR calibration from Figure 2-7. Crosses are AGNs from the EW classification, open circles are composite AGNs plus starbursts, and asterisks are starbursts. Sources with diamonds (all AGNs) are upper limits to SFR from upper limits to [CII] line fluxes in Table 1. Square is Markarian 231. L_{ir} is in $L_\odot$.

Another important result from Figure 2-8 is that AGNs are generally accompanied by starbursts, but AGN sources (including composites) encompass a much larger range and dispersion of SFR than do the pure starbursts. AGNs have $-1 < \log SFR < 2$ compared to $0.8 < \log SFR < 2.0$ for starbursts. At luminosity $L_{ir} \sim 10^{11} L_\odot$, AGNs have $-0.2 < \log SFR < 1.3$ compared to $0.7 < \log SFR < 1.7$ for starbursts. Composites are intermediate. These results mean that some fraction of L_{ir} arises from an accompanying starburst even for AGN-dominated L_{ir}, but the large dispersion in SFR/L_{ir} for AGN means this fraction varies by a factor of more than 10.

2.3.3. The [CII] "Deficit" and Source Classification

A primary result from analysis of [CII] luminosity from ISO measures was the discovery of the "[CII] deficit," whereby the most luminous sources have weak L([CII]) compared to infrared luminosity [41, 52]. This is confirmed in new Herschel results [21] and ground-based results [49]. The explanation of this deficit remains a question, and there are many possibilities, thoroughly reviewed by [41]. These include HII regions with densities above the critical density for [CII] emission, regions with increasing ionization parameter and harder ionizing radiation which diminishes or destroys the PDR [53, 82, 49, 21], and self-absorption or dust extinction of [CII].

One simple possibility to explain the deficit is that the most luminous sources are powered primarily by AGNs so that most of the infrared luminosity arises from AGNs which do not have accompanying L([CII]) from a starburst PDR. In this case, there would be no difference within the starburst regions or PDRs between ULIRGs and lower luminosity starbursts; the deficit is simply a consequence of increased AGN activity and the subsequent additional L_{ir}. This would be an important conclusion because of previous suggestions that individual starbursts in ULIRGs have higher luminosity density than other starbursts [41, 49].

Because we have already concluded that L([CII]) scales with the starburst component, we would expect [CII] to be relatively weaker if an AGN dominates L_{ir} than if L_{ir} arises primarily from starbursts. This is already shown in Figure 2-7, which demonstrates that AGNs systematically have smaller values of $L([CII])/L_{ir}$. Whether AGNs are responsible for the deficit is tested in Figure 2-9 by comparing $L([CII])/L_{ir}$ with L_{ir} using the source classifications derived from EW (6.2 μm). The overall distribution of points in Figure 2-9 demonstrates a deficit similar to the results summarized in [21, 49]. The line is fit to all points in our sample and would have an even steeper slope depending on the actual values for the upper limits. Figure 2-9 indicates that the [CII] deficit shown by our sample arises because of AGNs. All sources with a deficit, $\log L([CII])/L_{ir} < -3.4$, are either AGNs or composites. All AGNs do not show deficits, however. Some lower luminosity AGNs have $L([CII])/L_{ir}$ ratios similar to

starbursts; the deficit arises only in the highest luminosity AGNs. The ratios in Figure 9 and the SFRs shown in Figure 2-8 indicate that the starbursts within our sample have a maximum luminosity $L_{ir} \sim 10^{12}\ L_{\odot}$ at which $\log L([CII])/L_{ir} \sim -3.4$. Any further increase in L_{ir} comes only from an AGN component without additional L([CII]), thereby decreasing $L([CII])/L_{ir}$.

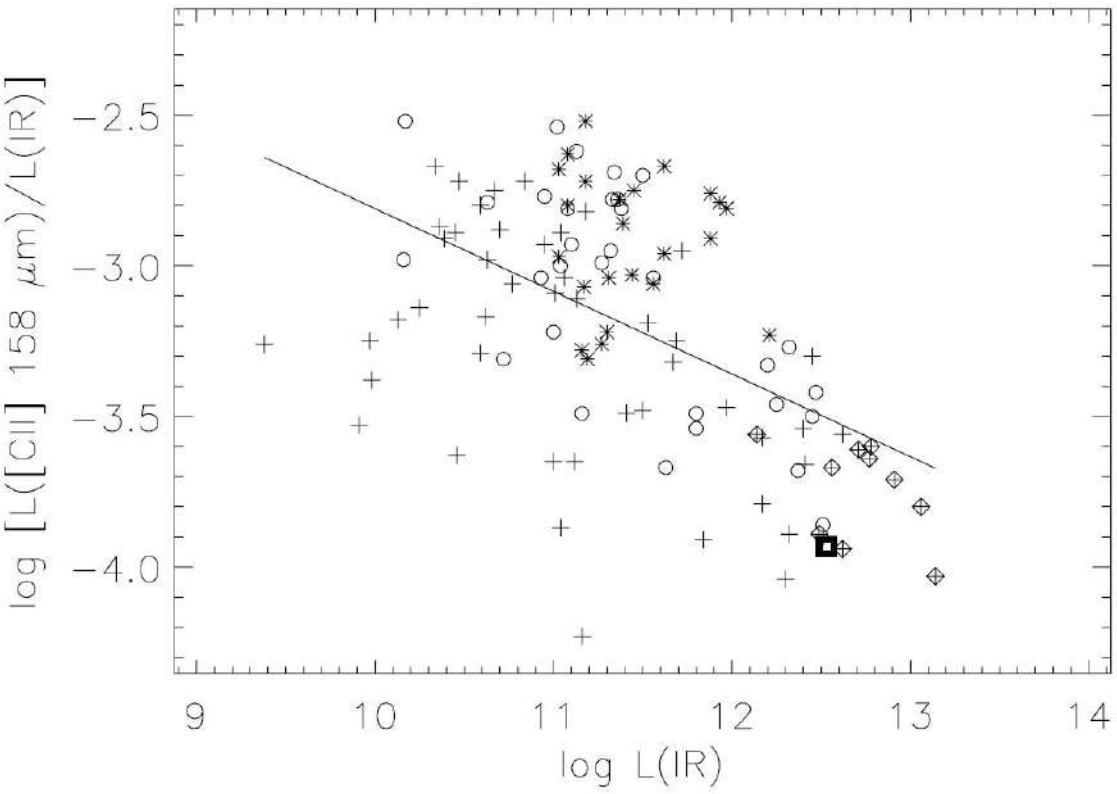

Figure 2-9. Ratio of [CII] luminosity to total infrared luminosity, L_{ir}, compared to L_{ir} in $L_{\odot}$. Crosses are AGNs from the EW (PAH 6.2μm) classification, open circles are composite AGNs plus starbursts, asterisks are starbursts, and sources with diamonds (all AGNs) are upper limits to [CII] line fluxes in Table 1; line is linear fit to all of these points. Square is Markarian 231.

These conclusions consider only the total infrared luminosity L_{ir} and do not address the important question of how the shape of the continuum SED depends on the AGN/starburst fraction. A measure of "far-infrared luminosity" is also defined by [25] using L_{fir} as an estimate of the 40 μm to 120 μm luminosity derived only from the 60 μm and 100 μm

bands, and L_{fir} is used as a luminosity measure in some of the other analyses cited above. Our PACS results also provide the far-infrared continuum flux density at rest-frame 158 μm, and we will discuss these results in a future analysis to determine, for example, if sources with larger starburst fractions determined from L([CII]) also have a greater proportion of far-infrared luminosity.

2.3.4. Comparisons to Dusty Sources at z ~ 2

At redshifts z ~ 2, the rest-frame spectral features observed with the Spitzer IRS are those shown in Figure 2-1. For starbursts and dusty, absorbed AGNs, the spectra show a maximum near 7.8 μm. For starbursts, this is the peak of the PAH feature. For absorbed AGNs, this is a localized continuum maximum between absorptions on both sides of the maximum [92]. These heavily absorbed AGNs are the AGN among the DOGs and were generally not known from optical observations because of the heavy extinction by dust. Type 1 AGNs or optically discovered quasars are also luminous in the infrared but have silicate in emission (e.g., [93]), which does not show the localized peak at 7.8 μm.

The presence of the 7.8 μm maximum explains why large numbers of dusty, optically obscured Spitzer sources are selected at z ~ 2, because this maximum becomes centered within the broadband 24 μm filter used for surveys with the Multiband Imaging Photometer for Spitzer [94]. Spitzer-discovered sources at these redshifts have also been measured in far-infrared, submillimeter, and millimeter wavelengths and compared to the Herschel or submillimeter-discovered populations [95, 40]. The highest redshift source confidently discovered based on IRS spectra has z = 3.35, a redshift limit set by the observable IRS long wavelength limit for identifying the 7.8 μm maximum.)

In spectra of faint sources with poor S/N, the spectral maximum near 7.8 μm is the most reliable observational measure of mid-infrared (rest-frame) flux density and can be easily measured from published spectra of faint, high-redshift sources [33, 96, 39, 97]. For these

reasons, our previous analyses of starbursts and AGNs observed with the IRS use the parameter νL_ν (7.8 μm) as a measure of infrared luminosity for local sources and Spitzer-discovered DOGs at z >~ 2 [98, 34, 99].

Future detections or limits on [CII] at high redshifts will provide important constraints on the earliest epochs of formation for luminous dusty starbursts and AGNs. It is useful, therefore, to compare f_ν (7.8 μm) and [CII] line fluxes for our present sample to predict [CII] line fluxes for the dusty population at z > 2, when scaled from the DOGs already known at z ~ 2.

The comparison is shown in Figure 2-10, using the maximum flux densities f_ν (7.8 μm) from [64] and comparing $f([CII])/\nu f_\nu$ (7.8 μm) so that units are the same. If high-redshift populations have the same [CII] characteristics as our low-redshift Herschel sample, these results predict $\log [f([CII])/\nu f_\nu (7.8\ \mu m)] = -2.2 \pm 0.2$ for starbursts and $\log [f([CII])/\nu f_\nu (7.8\ \mu m)] = -2.7 \pm 0.5$ for AGNs. The larger dispersion of this ratio for AGNs arises because of the large range in the starburst component of AGNs, discussed in Section 2.3.2.

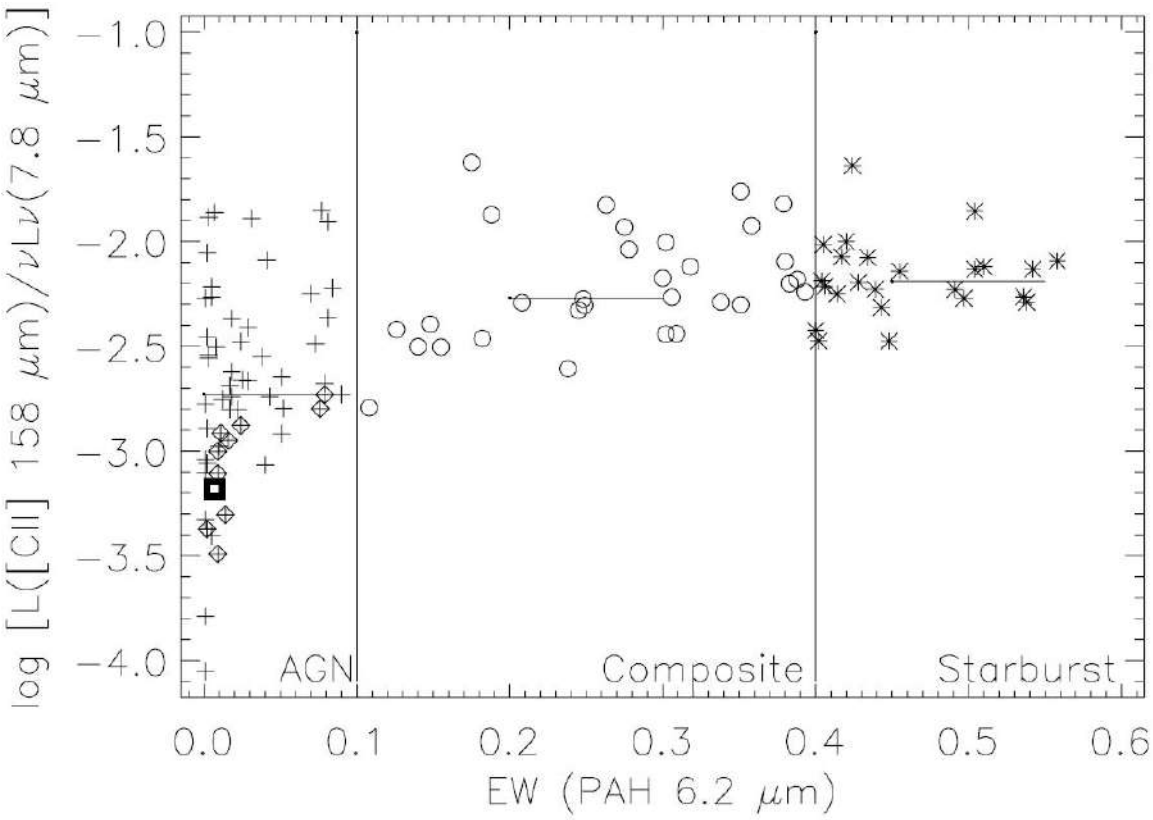

Figure 2-10. Ratio of luminosities L([CII])/νL_ν (7.8μm) for all sources in Table 1. Symbols are as in preceding figures. Horizontal bars are medians within each category; medians include limits because all limits fall below the median.

2.4. Conclusions and summary

The Herschel PACS instrument has been used to observe [CII] 158 μm line fluxes in 112 sources having a wide range of starburst and AGN classifications chosen because they have complete mid-infrared spectra with the Spitzer IRS and have complete IRAS fluxes for determining L_{ir}. Of the 112 sources, 102 have reliable line detections and 10 are upper limits.

It is found that the [CII] line flux correlates with the flux of the 11.3 μm PAH feature, log [f([CII] 158 μm)/f(11.3 μm PAH)] = −0.22 ± 0.25. This f([CII])/f(PAH) ratio is independent of AGN/starburst classification as determined from EW of the 6.2 μm PAH feature. We conclude that [CII] line flux measures the starburst component of any source as reliably as the PAH feature.

This conclusion leads to a calibration of SFR determined from the luminosity of [CII] for the starburst component in any source. The calibration is derived using L_{ir} only for starbursts to avoid AGN contamination of L_{ir} and has the result log SFR = log L([CII])] – 7.08 ± 0.3, for SFR in $M_\odot$ yr^{-1} and L([CII]) in $L_\odot$. This result applies to the starburst component of any source in which [CII] is observed. The maximum SFRs in the sample are 100 $M_\odot$ yr^{-1}, and SFRs are dominated by sources classified as starbursts, but most AGNs also have some measurable starburst component.

The [CII] "deficit," or a smaller ratio of L([CII])/L_{ir} with increasing L_{ir}, is shown to arise because L_{ir} of the most luminous sources arises primarily from an AGN so that L([CII]) from the starburst component is small in comparison.

3. [CII] 158 μm AND MID-INFRARED EMISSION LINES

A summary is presented for 130 galaxies observed with the Herschel Photodetector Array Camera and Spectrometer instrument to measure fluxes for the [CII] 158 μm emission line. Sources cover a wide range of active galactic nucleus to starburst classifications, as derived from polycyclic aromatic hydrocarbon strength measured with the Spitzer Infrared Spectrograph. Redshifts from [CII] and line to continuum strengths (equivalent width (EW) of [CII]) are given for the full sample, which includes 18 new [CII] flux measures. Calibration of L([CII)]) as a star formation rate (SFR) indicator is determined by comparing [CII] luminosities with mid-infrared [NeII] and [NeIII] emission line luminosities; this gives the same result as determining SFR using bolometric luminosities of reradiating dust from starbursts: log SFR = log L([CII)]) – 7.0, for SFR in M_O yr^{-1} and L([CII]) in L_O . We conclude that L([CII]) can be used to measure SFR in any source to a precision of ~50%, even if total source luminosities are dominated by an active galactic nucleus (AGN) component. The line to continuum ratio at 158 μm, EW([CII]), is not significantly greater for starbursts (median EW([CII]) = 1.0 μm) compared to composites and AGNs (median EW([CII]) = 0.7 μm), showing that the far-infrared continuum at 158 μm scales with [CII] regardless of classification. This indicates that the continuum at 158 μm also arises primarily from the starburst component within any source, giving log SFR = log νL_ν (158 μm) – 42.8 for SFR in M_O yr^{-1} and νL_ν (158 μm) in erg s^{-1}.

3.1. Introduction

The objective of our studies is to compare characteristics of [CII] emission with classifications and luminosities of sources determined from mid-infrared spectra, so that [CII] can be used alone as a quantitative diagnostic when no other spectroscopy is available. This is especially important for dusty sources at high redshifts, when the rest frame far-infrared can be observed in submillimeter and millimeter wavelengths, but other rest frame wavelengths are not observationally accessible.

Our observations consist of a sample of 130 sources which include a wide range of active galactic nucleus (AGN) through starburst (SB) classifications, using [CII] observations made with the Photodetector Array Camera and Spectrometer (PACS; [73]) on the Herschel Space Observatory [72]. The [CII] results are compared to mid-infrared spectroscopic diagnostics determined with the Spitzer Infrared Spectrograph (IRS; [30]). The sample is chosen to minimize effects of differing spatial resolutions when comparing Herschel far-infrared observations with Spitzer mid-infrared slit spectroscopy by choosing sources that are unresolved. Sample selection, classification, and results for [CII] fluxes for 112 sources are described in [75].

In that paper, it was found that the [CII] line flux correlates closely with the flux of the polycyclic aromatic hydrocarbon (PAH) 11.3 μm feature independently of AGN/SB classification, log [f([CII] 158 μm)/f(11.3 μm PAH)] = −0.22 ± 0.25. As a result, we concluded that [CII] line flux measures the same PDRs associated with SBs as the PAH feature [77] and, therefore, measures the SB component of any source. A calibration of star formation rate (SFR) was derived by comparing [CII] luminosity L([CII]) to total infrared luminosity L_{ir} using the precepts of [10], with the result that log SFR = log L([CII])] − 7.08 ± 0.3, for SFR in M_0 yr^{-1} and L([CII]) in L_0.

A comprehensive summary is given by [20] of all available [CII] measurements and their use as an SFR indicator through calibration with continuum luminosities (including both ultraviolet and infrared). Their emphasis is on determining uncertainties within the SFR calibration arising from cosmic variance and on discussing why differences can arise among sources. For SBs, the summary results are very similar to those in [75], with the same calibration and similar scatter for the relation between L([CII]) and SFR.

The uncertainties arising from cosmic variance among sources do not include systematic uncertainties in the assumptions used to transform total radiated luminosities from a star forming region into SFRs. It is important, therefore, to determine independent calibrations of L([CII)]) compared to SFR which depend on different precepts. The primary objective of this chapter is to obtain an independent calibration of L([CII)]) as an SFR indicator by comparing [CII] luminosities with mid-infrared [NeII] and [NeIII] emission line

luminosities, calibrated for SFR by [100], using new measurements of high resolution IRS spectra (Section 3.3.2). In addition, we determine the [CII] line to continuum ratio at 158 μm and use this to calibrate SFR from the continuum luminosity at 158 μm (Section 3.3.3); this allows an independent comparison to a previous calibration of SFR from 160 μm luminosity [101]. As part of these analyses, we also provide new [CII] observations of an additional 18 sources and provide new redshifts for all sources determined using only the [CII] emission line.

3.2. Observations

3.2.1. Selection and Classification of Sources

As summarized in [75], the sample selected for [CII] observations with Herschel PACS derives from sources having both Spitzer IRS spectra and full photometry with the Infrared Astronomical Satellite (IRAS), and for which f_ν(IRS)/f_ν(IRAS) comparisons at 25 μm indicate that sources are unresolved (because comparable source fluxes are measured with the slit of the IRS compared to the large beam of IRAS). Sources encompass a wide range of classification, from AGN through composite to SB, derived uniformly from the strength of the PAH 6.2 μm feature in IRS spectra.

Our AGN/SB classification, based on strength of the 6.2 μm PAH feature, is described in [75] and in [64]. The classification criterion is similar to that used in many previous studies, although different authors use different PAH features and different methods for measuring strength (e.g., [78, 102, 57, 60, 62, 63, 66]. The primary motive for using the 6.2 μm feature instead of the stronger 11.3 μm feature is to compare with sources having sufficiently high redshifts that the 11.3 μm feature is not visible in IRS spectra. Our measurement is simply the observed EW(PAH 6.2 μm) determined in a uniform fashion without any modeling assumptions regarding the mix of PAH features and/or the true level of underlying dust continuum. This measurement is made with the SMART software for IRS spectra [79], and the EW(PAH 6.2 μm) is determined using a Gaussian fit to the PAH feature and a linear fit to the continuum beneath the feature within the

range 5.5–6.9 μm. Measurements from IRS low resolution spectra and the empirical correlation of EW(PAH 6.2 μm) with source classification are given in [64]. All spectra are available in the CASSIS spectral atlas [74].

For purposes of the present chapter, the most important use of these diagnostics is to select sources confidently classified as pure SBs so these can be used to determine various relations among [CII], infrared lumi nosity, PAH luminosities, and emission line luminosities that apply to pure SB sources. These relations provide the calibration of SFR. The composite and AGN sources then illustrate changes that occur with increasing fractions of AGN luminosity added to the SB.

The classification utilized in the following discussion is summarized in Figure 3-1 using sources discussed below having both PAH and emission line measurements. The quantitative division among “pure AGNs” and “pure SBs,” with the intermediate “composite” systems is illustrated. The equivalent width (EW) boundaries which are shown derive by combining optical classifications and mid-infrared template spectra to determine classification boundaries as summarized in [64] and [75]. SBs have EW(PAH 6.2 μm) > 0.4 μm, composites have 0.1 μm < EW(PAH 6.2 μm) < 0.4 μm, and AGNs have EW(PAH 6.2 μm) < 0.1 μm. Pure SBs are defined as systems with >90% of the mid-infrared luminosity arising from a starburst, and pure AGNs as systems with >90% of the mid-infrared luminosity arising from the AGN [75]. Composites have mixtures of these components. For the full sample of 130 sources in this chapter, these criteria give 60 AGNs, 36 composites, and 34 starbursts.

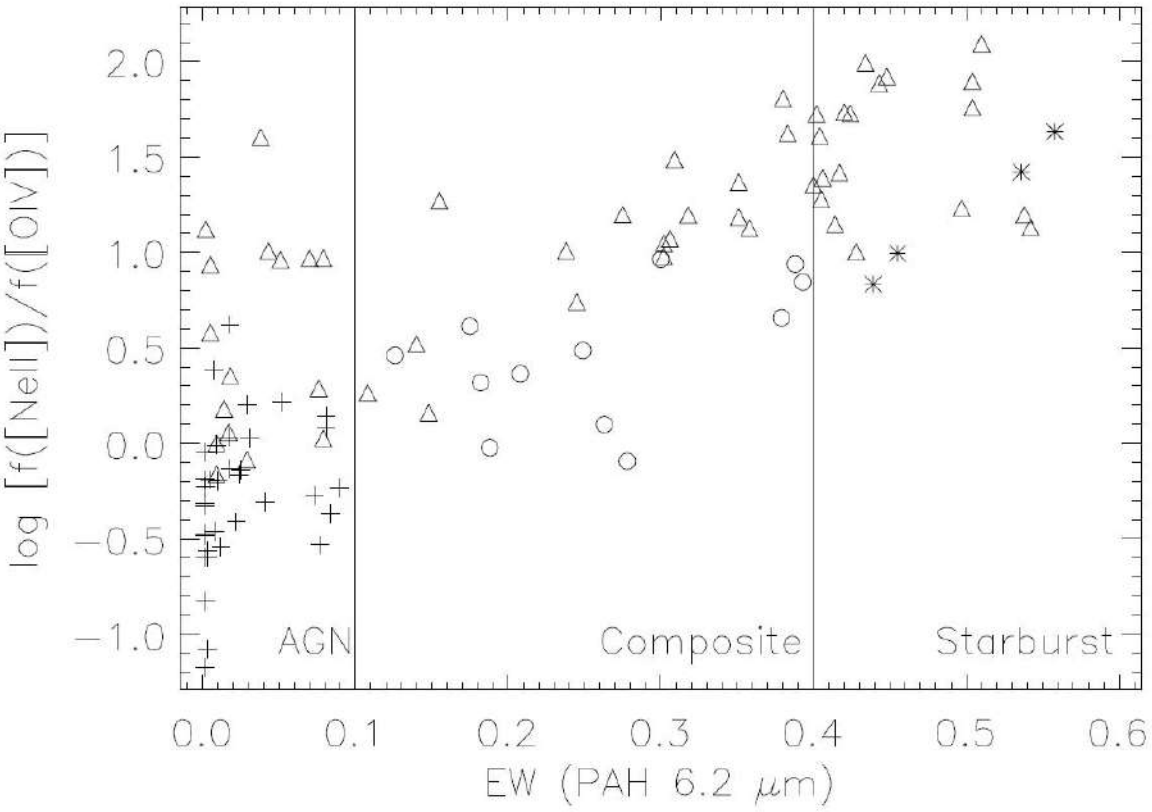

Figure 3-1. Ratio of [NeII] 12.81 μm to [OIV] 25.89 μm emission line fluxes compared to the equivalent width of the PAH 6.2 μm feature in μm. Dividing lines show the division into classifications based on EW(PAH 6.2 μm) used throughout this paper. Crosses are sources classified as pure AGNs, asterisks as pure starbursts, and circles are composites with contribution from both. Triangles are lower limits, in which the [OIV] feature is not measured.

The summary of results in Figure 3-1 comparing the ratio of [NeII] 12.81 μm to [OIV] 25.89 μm emission line fluxes with the classification derived from PAH EW illustrates the conclusions from many previous studies (e.g., [103, 78, 104, 105, 58] that PAH strength correlates with level of ionization as seen in emission lines, which confirms the AGN/SB classification derived from PAH strength. Both the EW(PAH 6.2 μm) from the SB PDR and the relative [NeII] emission line strength from the SB HII region decrease as the SB component decreases, because the AGN adds additional hot dust continuum in the mid-infrared that diminishes EW(PAH 6.2 μm) and also adds increasing strength of the higher

ionization [OIV] (the ionization potential required to produce NeII is 21.6 eV compared to 55 eV to produce OIV).

3.2.2. [CII] Observations and Uncertainties

The [CII] observations are described in [75], where examples of observed line profiles are illustrated. All [CII] observations were made using the Herschel PACS instrument [73] for line spectroscopy in point source chop nod mode with medium throw. [CII] line fluxes are obtained by summing fluxes in the nine central equivalent spatial pixels, or "spaxels," produced by the PACS image slicer. A correction communicated to us by the PACS calibration team is applied for flux that would fall outside these spaxels for an unresolved source, correcting the nine spaxel flux by a factor of 1.16(λ/158 μm) 0.17, with wavelength λ depending on redshift. Data reduction in [75] was done with version 8 of the Herschel Interactive Processing Environment (HIPE), and the "PACSman" software [80] is used for fitting line profiles and continuum.

An additional 18 sources were subsequently observed in program Isargsya-OT2. These [CII] fluxes were derived in a similar way and are given in Table 1 of [106]. Results for the total sample of 130 sources are summarized in Table 2 of [106] where [CII] fluxes for the 112 sources from [75] are also reproduced. Line fluxes are determined from the flux within a fitted Gaussian profile except for 12 sources for which the [CII] profile is asymmetric or shows component structure. For these 12, the total line flux is the integrated flux including all components rather than the flux within a single Gaussian fit.

All results are determined with HIPE version 8. The new sources were also extracted with HIPE version 10, which has a different calibration from version 8. By reducing new sources with both v8 and v10, we find a systematic flux difference such that v8 fluxes are a factor of 1.07 brighter compared to v10. This difference is noted in Table 1 of [106], but fluxes listed for the new sources arise from v8 to be consistent with results in [75].

PACS observations of the [CII] line are made in a continuous scanning mode that produces a "data cloud" containing a large number of separate flux measurements within individual wavelength elements because the spectrometer is read out every 1/8 s [73] and PACS Observer's Manual) during the total integration time of 579 s for these observations. The PACSman uncertainties at each wavelength are determined from the dispersion among the individual measurements within the data cloud. The signal-to-noise ratio (S/N) of the overall profile fit is determined using the uncertainties within these individual wavelength elements. Examples of profiles and fits are shown in [75], including a noisy profile with plotted uncertainties.

Uncertainties of individual [CII] emission line fluxes are determined by the S/N of the profile fit by PACSman in the brightest spaxel, with uncertainties listed in [75] individually by source. S/N is defined as the (line flux)/(uncertainty in line flux) arising from the profile fitting. If S/N < 3, fluxes were listed as upper limits in [75] and are shown as upper limits in plots within the present paper. No new sources in Table 1 of [106] are limits. Median S/N for the remaining sources indicates a median line flux uncertainty of ±15%. The systematic uncertainty for [CII] fluxes depends on PACS flux calibration, estimated as ±12% in the PACS Spectroscopy performance and calibration document PICC-KL-TN-041. (The offset we find between HIPE v8 and v10 reductions is within this uncertainty.) Combining these two sources of uncertainty yields a typical combined uncertainty of ±20% for [CII] fluxes.

In [75], redshifts were listed based on previously determined optical redshifts, verified by IRS mid-infrared emission lines. In Tables 1 and 2 of the [106], we list new redshifts derived from the [CII] line only. Redshifts generally agree to <~0.002, but the [CII] redshifts are given here to allow further study of any systematic differences between [CII] emitting regions and optical or mid-infrared regions.

Uncertainties in measured [CII] line velocities are dominated by centering effects, as described in the PACS Observer's Manual. Depending on precisely where within a spaxel the source is centered, the observed wavelength of the emission line can change by ~±40 km s^{-1}. To empirically estimate the uncertainties arising both from this effect and from

fitting the line profile, we compare in Figure 3-2 the [CII] centroid velocity within the brightest spaxel relative to the velocity within the second brightest spaxel (only for sources in which both spaxels have S/N > 3). This plot does not include the 12 sources noted in Table 2 with asymmetric or component structure to the [CII] line profile, because these sources may really have spatially different components on a sub-spaxel scale.

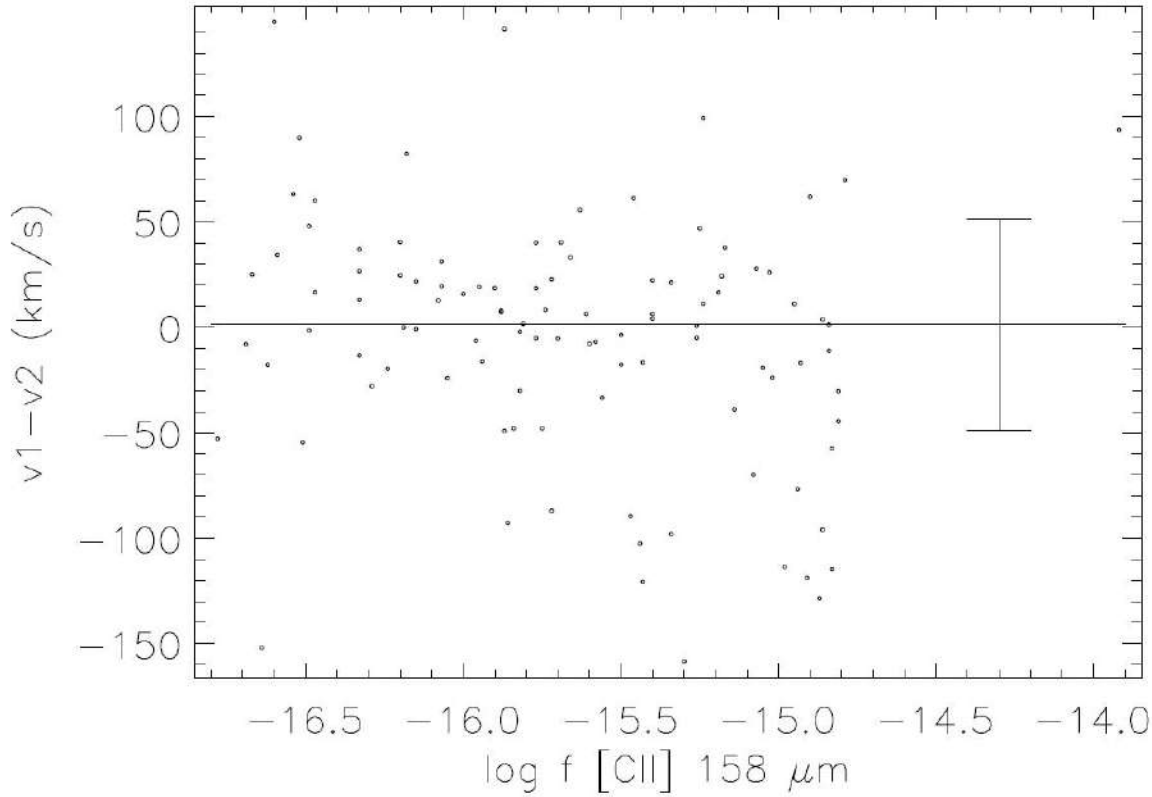

Figure 3-2. Difference in measured [CII] line profile velocities in km s^{-1} between the profile centroid velocity in the brightest spaxel (v1) compared to the velocity in the second brightest spaxel (v2), using only sources in which both spaxels have S/N > 3 for the measured line flux; line flux is shown in units of W m^{-2}. The empirical uncertainty of final [CII] velocity measurements is taken as the 1σ dispersion among these velocity differences of ±50 km s^{-1}, which includes uncertainties arising both from profile fitting and from the location of the source within a spaxel. This plot does not include the 12 sources with asymmetric or component structure for which we only use the velocities from the brightest spaxel, because these are sources which may have real spatially different components.

From Figure 3-2, the brightest spaxel systematically gives the same velocity as other spaxels; the median velocity offset between the brightest and second brightest is less than 1 km s^{-1}. The random errors from source position and profile fitting are determined as the 1σ dispersion among the velocity differences shown between the brightest spaxel and the second brightest, which gives a dispersion of ±50 km s^{-1}. This is our measurement of empirical uncertainty for the measured [CII] velocities. This dispersion is much larger than the formal centroiding uncertainty of the line fit for the brightest spaxel, typically only a few km s^{-1} in the PACSman fits, indicating that velocity uncertainties are dominated by positional effects of the source within the spaxel. The final redshift measurement which is reported in Tables 1 and 2 of [106] is that of only the brightest spaxel.

In Section 3.3.3, the line to continuum ratio (EW) for the [CII] line is discussed. This is important for understanding the relation between far-infrared dust continuum reradiation and the origin of the [CII] emission line. Uncertainties in EW arise from both the [CII] emission as uncertainties in the line flux, and as uncertainties in the level of the underlying continuum. Usually, the latter is a much larger source of uncertainty because source continua are faint compared to the background. These two uncertainties as determined by PACSman are summed quadratically to give total uncertainty in the EW which is listed in Table 2.

Comparisons of [CII] with PAH fluxes in [75] and below are made using the 11.3 μm PAH feature because this is the strongest PAH feature in IRS spectra. The flux ratios for the new sources are given in Table 1, using measurements of the 11.3 μm feature taken from [64] as determined with a Gaussian fit to the PAH feature and a linear fit to the continuum beneath the feature from 10.5 μm to 12 μm.

3.2.3. IRS Emission Line Observations and Uncertainties

In [75], [CII] observations were compared with PAH strength using IRS low resolution spectra. All objects in that paper also have IRS high resolution spectra, which derive from archival observations in various Spitzer observing programs (e.g., [58, 60, 62, 107]. For many sources, line fluxes have been previously published. In the [106], we remeasure emission lines in these high resolution spectra with the goal of a uniformly measured data set that uses the final IRS flux calibrations and noise masks; the new measurements also provide an empirical determination of line flux uncertainties that arise from the profile fitting process and noise removal.

Line fluxes are measured using Gaussian fits in the SMART analysis program [79], beginning with the post-Basic Calibrated Data products in the Spitzer Heritage Archive. The line fit is on top of the underlying continuum which is a combination of background and real source continuum. Because of the short IRS high resolution slit, simultaneous background measurements cannot be subtracted from a single on-source observation, so we do not determine the real source continuum before fitting the line. Therefore, EWs are not measured. High resolution spectra are especially important for the [NeII] 12.81 μm line fluxes because an adjacent PAH feature makes accurate [NeII] measures impossible on low resolution spectra. We treat the wings of the PAH as an underlying continuum when measuring the [NeII] flux.

Even after removal of known bad pixels, the IRS high resolution spectra are contaminated by noise spikes from individual "rogue pixels." These rarely interfere with individual emission lines at known wavelengths, although they are serious contaminants when searching for weak, unknown emission features. In those few cases when a single pixel noise spike interferes with an otherwise smooth emission line profile, such spikes are removed by visual inspection. This is done independently for each spectrum from the two nods of an observation, and line profiles are fit independently for each nod. To estimate the uncertainty of line fluxes arising from the noise removal and from the line fitting process, line fluxes from the two spectra arising from the two nods were compared. As expected, line uncertainty is greater for fainter lines. The dispersion of the ratio of measured fluxes between the two nods is ±9% for all lines, and ±6% for bright lines with log

flux >–20.2 (units of W cm^{-2}). For quadratically combining IRS line flux uncertainty with the [CII] uncertainty of ±20%, we adopt the larger 9% dispersion for all lines, giving a final uncertainty for flux ratios [CII]/IRS lines = ±22%.

3.3. Discussion

3.3.1. Comparison of [CII] Fluxes and Mid-infrared Emission Lines

In Figures 3-3 – 3-6, the [CII] flux is compared with mid-infrared features from IRS spectra. All scales are the same so ratios can be compared among the plots. Figure 3-3 repeats the comparison with PAH 11.3 μm from [75], adding the new sources in Table 1 of [106]. Figure 3-4 compares [C II] to [NeII], Figure 3-5 [CII] to [NeIII], and Figure 3-6 [CII] to [NeII]+[NeIII].

The comparison with PAH in Figure 3-3 reconfirms the conclusion in [75], that the scaling between [CII] and PAH is independent of source classification, implying that the SB component and SFR is measured equally well by PAH emission or by [CII] emission in sources of all classifications. The correlation of [CII] with a SFR indicator can be checked in a completely independent way using Figure 3-4, which compares [CII] with [NeII], because [NeII] is a luminosity indicator of star formation determined by the HII region instead of the surrounding PDR.

Figure 3-4 shows a result very similar to the [CII]/PAH comparison. The median ratios f([CII])/f([NeII]) are independent of classification. The dispersion about the median is also similar to the dispersion in [CII]/PAH. Because [NeII] arises primarily from SBs, this result is very important empirically because it confirms the previous conclusion from PAH that [CII] scales with the SB component within sources of all classifications.

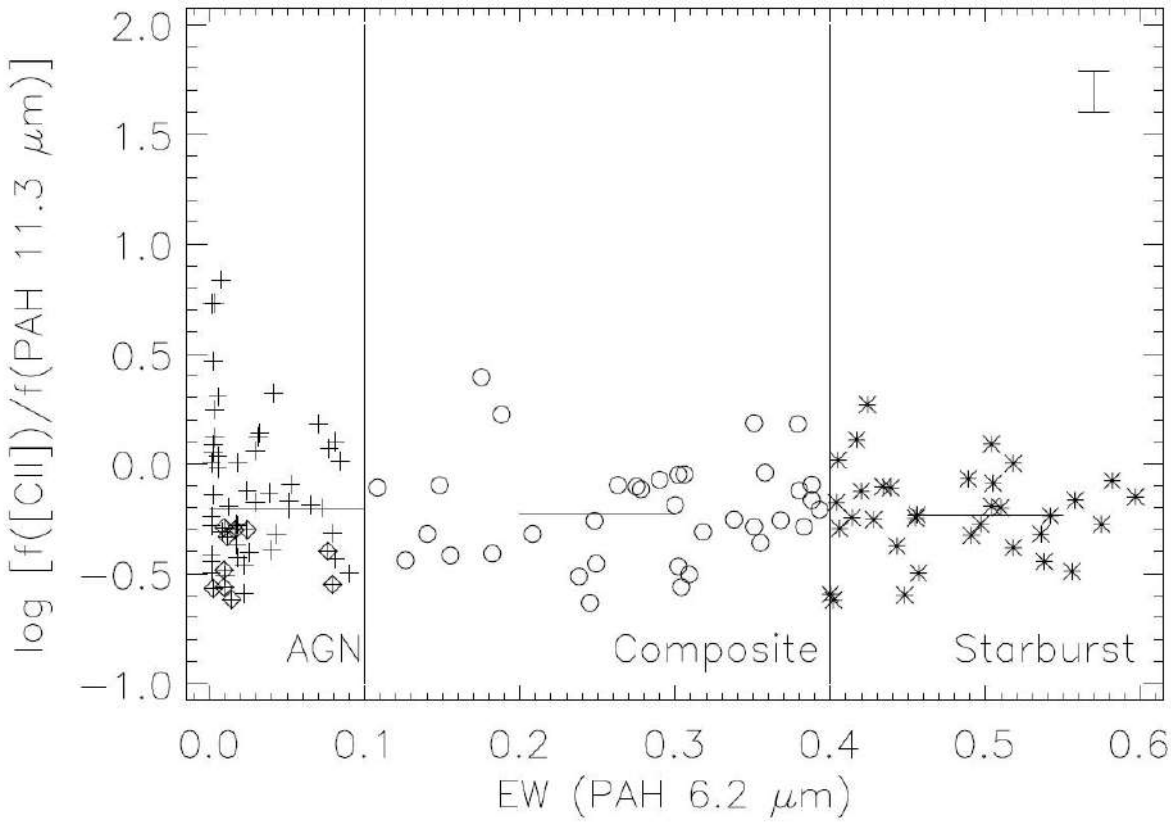

Figure 3-3. Ratio of [CII] 158 μm to PAH 11.3 μm line fluxes, compared to the source classification from EW(PAH 6.2 μm) measured in μm, for all sources. Crosses are AGNs from the EW(PAH 6.2 μm) classification, open circles are composite AGNs plus starburst, and asterisks are starbursts. Sources with diamonds (all AGNs) are upper limits to [CII] line fluxes. Horizontal bars are medians within each category; medians include limits because all limits fall below the median. Vertical error bar shows the observational line ratio uncertainty for individual points of ±22% derived in the text.

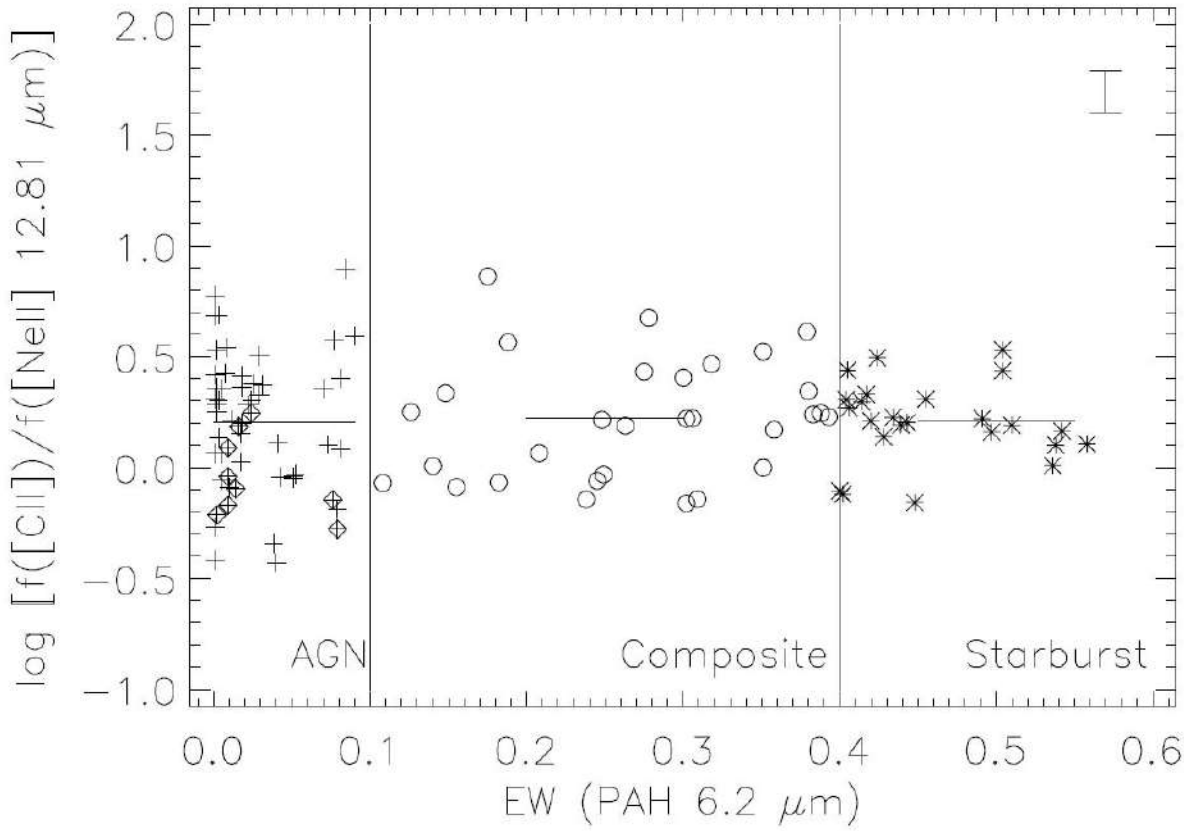

Figure 3-4. Ratio of [CII] 158 μm to [NeII] 12.81 μm line fluxes, compared to source classification from EW(PAH 6.2 μm) measured in μm. Crosses are AGNs from the EW(PAH 6.2 μm) classification, open circles are composite AGNs plus starburst, and asterisks are starbursts. Sources with diamonds (all AGNs) are upper limits to the ratio because their values are limits to [CII] line fluxes but detections in [NeII]. Horizontal bars are medians within each category, including limits. Vertical error bar shows the observational line ratio uncertainty for individual points of ±22% derived in the text.

Figure 3-5 compares [CII] with [NeIII]. There is a greater difference of ratio with classification than for [NeII]. The increasing ratio f([CII])/f([NeIII]) from AGNs to SBs can be explained if [NeIII] arises both from AGN ionization and SB ionization, but [CII] arises only from SBs, so that AGNs contain an additional [NeIII] component compared to [CII]. The implications of these results are discussed in the next section.

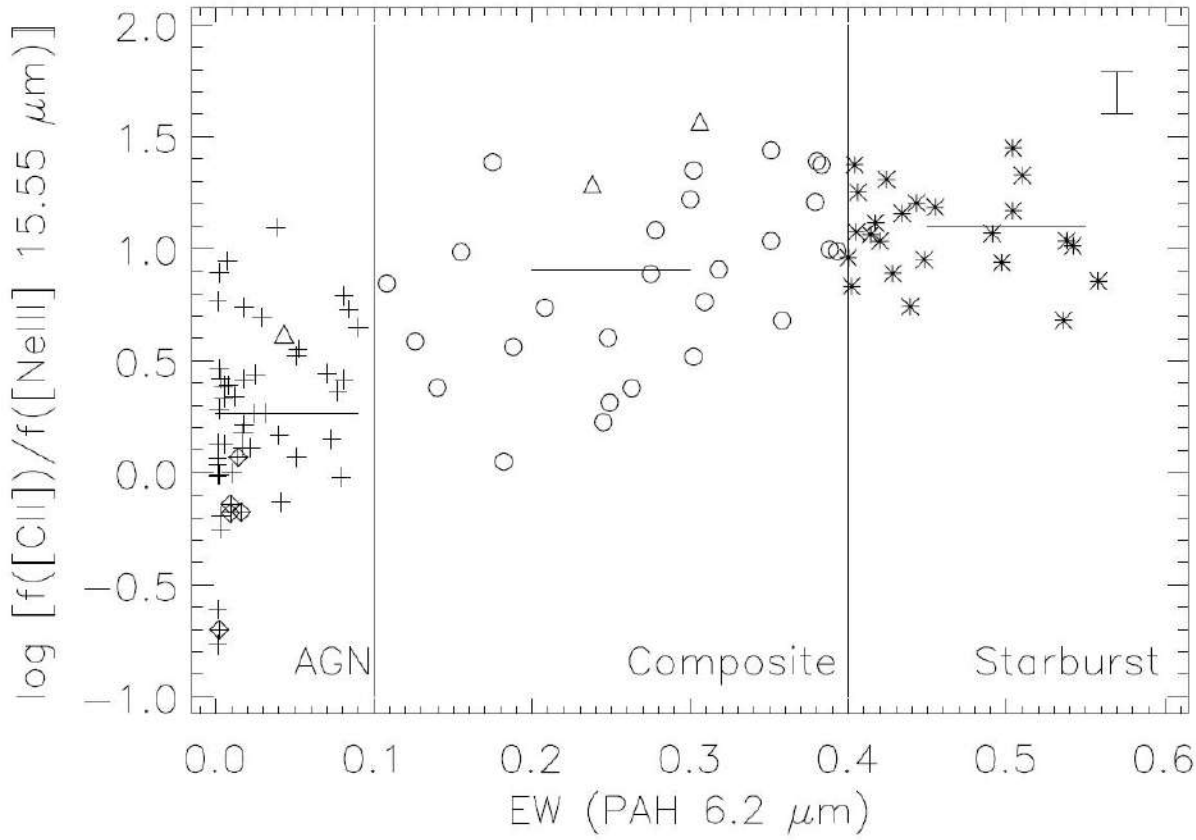

Figure 3-5. Ratio of [CII] 158 μm to [NeIII] 15.55 μm line fluxes, compared to source classification from EW(PAH 6.2 μm) measured in μm. Crosses are AGNs from the EW(PAH 6.2 μm) classification, open circles are composite AGNs plus starburst, and asterisks are starbursts. Sources with diamonds (all AGNs) are upper limits to the ratio because their values are limits to [CII] line fluxes but detections in [NeIII]. Triangles are lower limits to the ratio because values arise from limits for [NeIII] but detections in [CII]. Horizontal bars are medians within each category, including limits. Vertical error bar shows the observational line ratio uncertainty for individual points of ±22% derived in the text.

3.3.2. Star Formation Rate from [CII] Calibrated with Neon Emission Lines

The [CII] line is expected to arise primarily within the PDR surrounding star forming regions [51, 52, 53, 54]. As the primary cooling line for low ionization regions, [CII] can also arise within more diffuse emission regions associated with the "infrared cirrus," for

which the ionization and heating of CII (and the accompanying far-infrared dust continuum) is not necessarily a measure of the young, ongoing SBs. This diffuse [CII] is observed in nearby, resolved galaxies [108]. The scaling of [CII] with PAH found in [75] for luminous, unresolved sources indicates, however, that [CII] primarily measures the PDRs in spatially integrated observations that include entire galaxies rather than individual regions within galaxies.

In [75], SFR was determined by the comparison of [CII] to total infrared luminosity, using the assumption [10] that all of the radiation from ongoing star formation is absorbed and reemitted in the infrared spectrum by the dust. A completely independent estimate of SFR can be made by ionization models of the HII region, where the emission lines are related only to the ultraviolet ionizing continuum of the SB. A great advantage of using mid-infrared emission lines for comparison to the models is that they are much less subject to uncertainties regarding extinction corrections compared to optical lines.

SB models have been scaled to the luminosity of the infrared [NeII] and [NeIII] lines by [100] and discussed in comparison with Spitzer IRS observations by [58]. The Ho and Keto result is SFR (M_0 yr^{-1}) = 4.34×10^{-41} L([NeII]+[NeIII]) (erg s^{-1}), estimating about a factor of two uncertainty for individual sources depending on the fraction of ionizing photons which are absorbed by gas and the fractional ionizing state of neon. These differences arising from cosmic variance among sources can explain the dispersion in the [CII]/([NeII]+[NeIII]) ratio in Figure 3-6, for example. In what follows, we use only the pure SBs in Figure 3-6 for comparisons to avoid any uncertainty regarding neon luminosity from an AGN component.

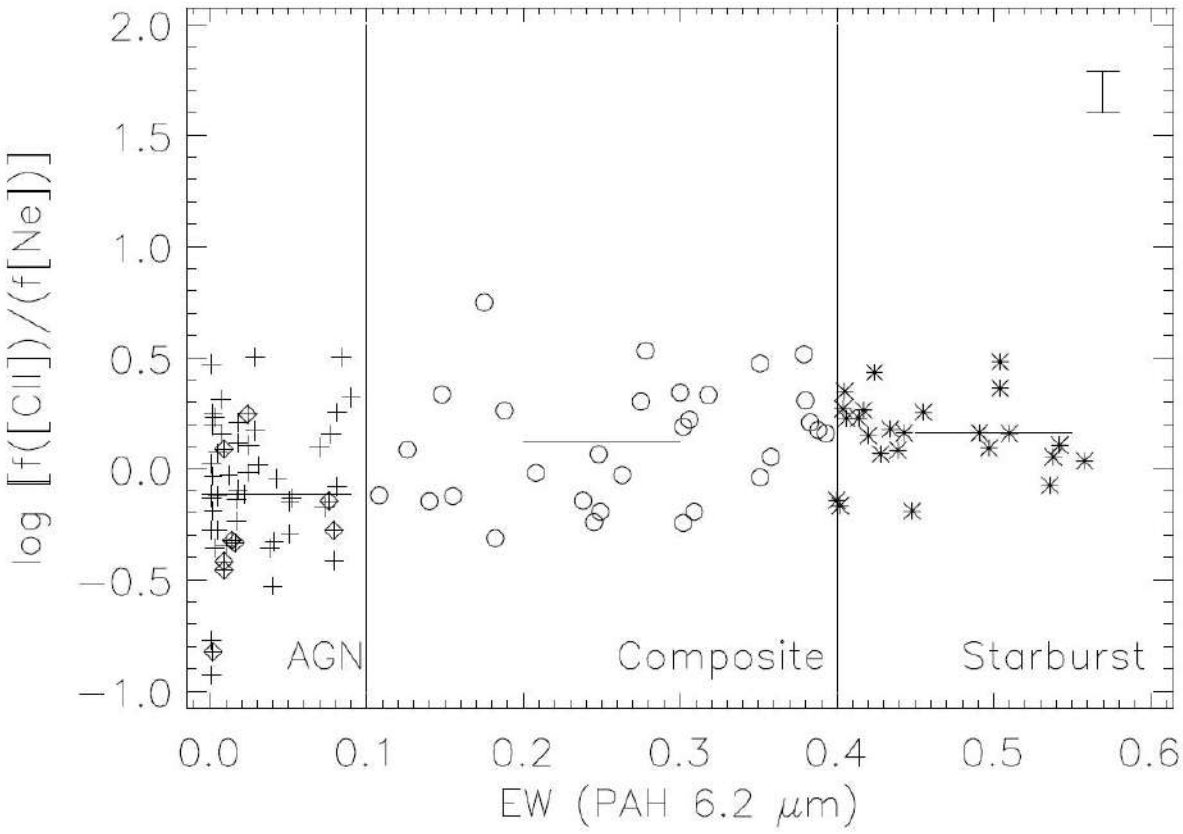

Figure 3-6. Ratio of [CII] 158 μm to [NeII] 12.81 μm + [NeIII] 15.55 μm line fluxes, compared to source classification from EW(PAH 6.2 μm) measured in μm. Crosses are AGNs from the EW(PAH 6.2 μm) classification, open circles are composite AGNs plus starburst, and asterisks are starbursts. Sources with diamonds are upper limits to the ratio because their values are limits to [CII] line fluxes but detections in [NeIII] and/or [NeII]. Horizontal bars are medians within each category, including limits. Vertical error bar shows the observational line ratio uncertainty for individual points of ±22% derived in the text.

Figure 3-6 shows the scaling with [CII]. For the pure SBs in our sample, the result is log f[CII]/(f[NeII]+ [NeIII]) = 0.16 ± 0.15. Composites give a similar result, but, as expected from the individual plots for these lines in Figures 3-4 and 3-5, the value for AGNs is lower. This scaling for pure SBs applied to the Ho and Keto relation gives the result that SFR ($M_\odot$ yr^{-1}) = 3 × 10^{-41} L([CII]) (erg s^{-1}), or log SFR = log L([CII]) – 6.93 ± 0.15 for SFR in $M_\odot$ yr^{-1} and L([CII]) in $L_\odot$. Our result derived in Paper I from calibrating SFR using the

total infrared dust luminosity was log SFR = log L([CII)]) – 7.08 ± 0.3, so the two independent results agree well within the cosmic variance among sources. The systematic difference in SFR calibration is less than the variance within either calibration. From this, we conclude that the relation log SFR = log L([CII)]) – 7.0 can measure SFR to a precision of ±<~50% for any individual source within the uncertainties arising from cosmic variance.

Our conclusion that [CII] is a reliable SFR indicator differs from the conclusions of [109] and [110]. This difference arises primarily from our calibration of SFR derived from either the bolometric luminosities or the neon line luminosities using only pure SBs based on the PAH classification criterion. The spectral energy distributions of dusty sources show large variations, with changes in characteristic temperatures that may depend on luminosity or redshift (e.g., [111, 112]). Determining the relative AGN/SB contribution to dust luminosity at different infrared wavelengths is a complex problem to which various diagnostics can be applied [60]. By using only a subset of sources having no indications of any AGN contribution, contamination from AGN luminosity cannot affect the calibration of SFR, and it is not necessary to determine quantitatively the AGN/SB fraction within individual sources to determine an SFR calibration. This issue and the differences from previous conclusions are considered further in the next section.

All of the results summarized above show consistent correlations between the [CII] luminosity and the luminosity of the SB PDRs measured using the [CII]/PAH ratio and from the SB HII regions measured with the neon lines. These results imply that [CII] measures the same SBs as those measured with the mid-infrared diagnostics. Are there any sources with indications of excess [CII] luminosity that may not be associated with the SB PDR or HII region luminosities? Additional [CII] could arise from lower ionization regions associated with an AGN or from widespread low ionization from older SBs and association with infrared cirrus [111]. There could also be excess [CII] compared to the mid-infrared diagnostics if SBs are so dusty that the mid-infrared features suffer significant extinction compared to [CII] (e.g., [110]).

The ratios among [CII]/PAH/[NeII] in Figures 3-3 and 3-4 show median ratios that are the same for all classifications from AGN through SB. The sources with the largest [CII] excess are among composites and AGN, so those are the best candidates for sources with additional [CII] not associated with the SBs. For this reason, we attempt an estimate of the excess [CII] luminosity which may be present in composites and AGNs.

To do this, we determine the [CII] luminosity remaining in the AGN and composite sources, L([CII], other), after subtracting from the total L([CII]) the luminosity component from SBs, L([CII], SB), assuming the median observed ratio logL([CII], SB)/L(PAH 11.3) = 0.22 for SBs in Figure 3-3. For example, if log L([CII], other)/L([CII]) = –0.3, this means that 50% of the observed L([CII]) does not arise from the SB component. In many cases, this leads to L([CII], SB) > L([CII]). In these cases, we arbitrarily adopt a limit L([CII], other) < 0.1 L([CII]).

Because of the scatter of ~0.2 dex in the L([CII], SB)/L(PAH 11.3) ratio for individual SBs (Figure 3-3), only statistical estimates for the overall samples can be determined in this way. Of the 36 composite sources, only 4 have log L([CII], other)/L([CII]) > –0.3. This means that [CII] luminosity from alternative sources may exceed [CII] luminosity from conventional SBs in only 11% of composite sources. For AGNs, only 14 of 60 AGNs exceed log L([CII], other)/L([CII]) = –0.3, meaning that 23% of AGNs may have excess [CII] luminosity that exceeds the SB [CII] luminosity. While these estimates are approximate and qualitative, they indicate that there is no strong evidence within our sample for sources in which [CII] luminosity arising from other mechanisms exceeds the [CII] luminosity from ongoing star formation.

3.3.3. Ratio of [CII] Luminosity to Continuum Luminosities

The comparisons of [CII] with neon line fluxes in the preceding section confirm, as did the PAH comparisons discussed in [75], that the [CII] luminosity gives the same measure of SFR as that found using the mid-infrared diagnostics. A related and important question

is how SFR measured with [CII] compares with SFR measured using only the infrared continuum luminosity. This is crucial because of the common use of the continuum luminosity alone, particularly the far-infrared continuum, to measure the evolution of star formation in the universe [113, 114].

The biggest question in the comparison of continuum luminosity and L([CII)]) arises from previous observations that more luminous sources in L_{fir} have relatively weaker L([CII)]), termed the "[CII] Deficit" [41, 52, 21, 49]. The L_{fir} is usually defined as the luminosity within 40 μm <~ λ <~ 125 μm, measured quantitatively using the 60 μm and 100 μm photometry with IRAS according to the formulation in [115]. A deficit could be explained by SBs with increasing ionization parameter and harder ionizing radiation in more luminous sources [53, 82, 49] or by having dustier, more obscured SBs [110, 109]. If L_{fir} invariably measures SFR, then a deficit would mean that the SFR from [CII] is systematically underestimated for the most luminous sources.

In [75], we concluded that the deficit is not a consequence of differences among SBs but instead arises because more luminous sources have increasing contributions from AGNs to the dust continuum luminosity. This conclusion arose because luminous sources with an apparent deficit show the mid-infrared diagnostic of AGNs (weak PAH), indicating that most continuum luminosity is produced by AGN dust heating. This is illustrated in Figure 9 of [75], where our sources reach $L_{ir} > 10^{13}$ L_O, but all sources except one having $L_{ir} > 10^{12}$ L_O contain AGNs. The one SB does not show a deficit compared to lower luminosity SBs, but the high luminosity AGNs do show a systematic deficit.

We illustrate this result again in Figure 3-7 using the conventional parameters for the deficit, the ratio L([CII)])/L_{fir} compared to L_{fir}, determining L_{fir} from the IRAS fluxes tabulated in [64]. The plot is made only for pure SBs, as defined by our classification criterion EW(PAH 6.2 μm) > 0.4 μm. The distribution of results for our sample (crosses) confirms the conclusion of [75]—that no trend of ratio with luminosity is seen in the L([CII)])/L_{fir} ratio when only pure SBs are used.

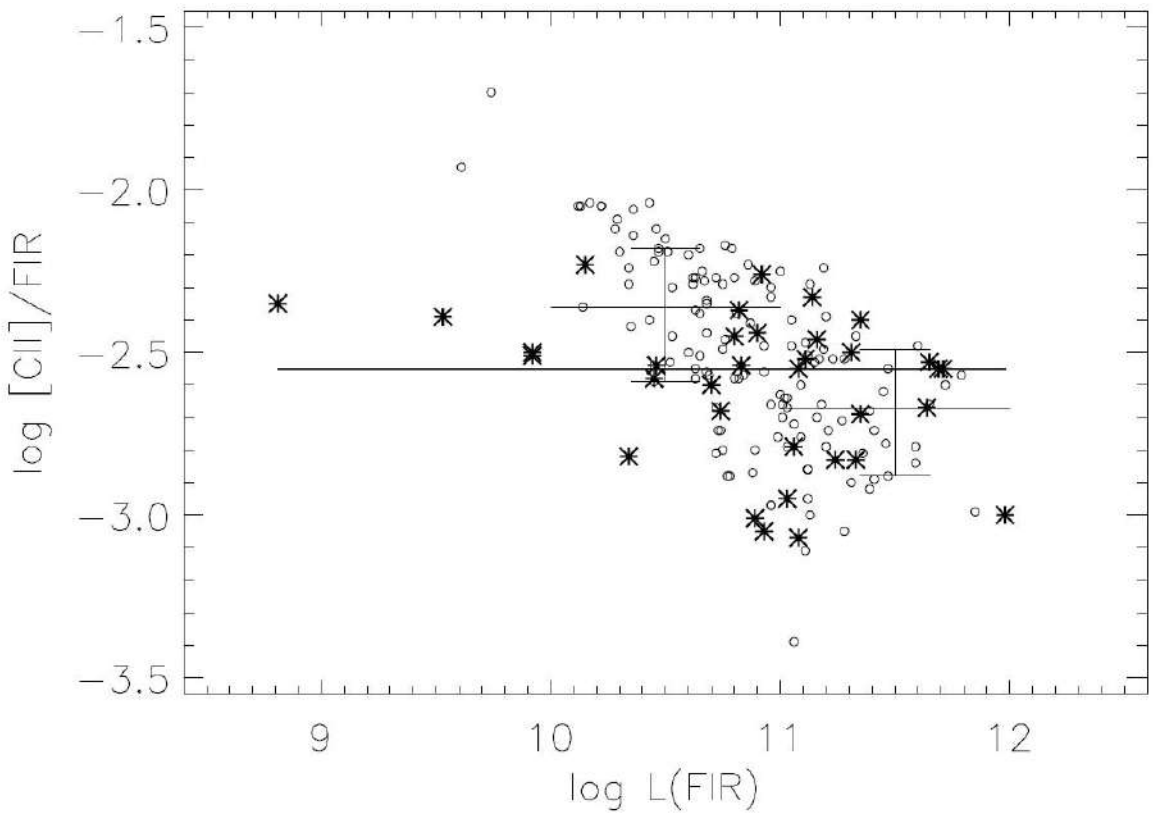

Figure 3-7. Ratio of L([CII])/L_{fir} compared to L_{fir} for starbursts in L_o. Asterisks are starbursts from current sample and the thick horizontal line is their median. Circles are starbursts from [109] using their criterion for pure starbursts; thin horizontal lines and error bars are medians and 1σ dispersions within this sample for 10 < log L_{fir} < 11, and 11 < log L_{fir} < 12.

Figure 3-7 also includes results (circles) for SBs in the [CII] sample of [109] defined by their stated criterion for pure SBs, which is EW(PAH 6.2 μm) > 0.5 μm using PAH measurements from [66]. These results show an overall median that agrees with ours. Within the limited range of L_{fir}, any trend for L([CII])/L_{fir} to decrease with L_{fir} in the Diaz-Santos sample is less than the 1σ dispersion among SBs at any given luminosity. For example, from log L_{fir} (L_o) = 10.5 to log L_{fir} (L_o) = 11.5, the median ratio decreases by a factor of two, but the dispersions at both luminosities exceed a factor of 2.5. Their sources with 10 < log L_{fir} (L_o) < 11 exceed our median ratio by only a factor of 1.5, and their sources with 11 < log L_{fir} (L_o) < 12 are below our median ratio by a factor of 0.8. These comparisons indicate consistency between the two samples of SBs.

To further consider the deficit issue, we can extend consideration of the [CII] line to continuum ratio to longer wavelengths (representing emission from cooler dust) than measured by L_{fir}. This can be done because the continuum at rest frame 158 μm is also measurable for most of our sources having [CII] line observations. Attributing a deficit to luminous SBs invokes the assumption that the coolest dust in luminous sources is invariably heated by SBs instead of AGNs. Even if the far-infrared continuum at <~100 μm can include contributions from AGN heating, as we have concluded, it might be expected that cooler dust seen at longer wavelengths would be increasingly dominated by the SB component. If a deficit really exists among pure SBs, therefore, the deficit should be as readily seen comparing L([CII]) to νL_ν (158 μm) as when comparing to L_{fir}. Conversely, if the apparent deficit arises because L_{fir} is contaminated by hotter AGN dust, any deficit arising because AGNs are included in the sample should diminish when measured with the cooler dust seen at 158 μm.

The strength of [CII] compared to the continuum is defined by the EW, which is a linear measurement of the line to continuum ratio. EW relates to continuum luminosities by νL_ν (158 μm) = λL_λ (158 μm) = λL([CII])/ EW([CII]) for λ = 158 μm. Measuring L([CII)]) and νL_ν (158 μm) with the same PACS observation has an additional advantage in that the spatial resolution of both measures is identical. For sources that may be resolved, this removes one concern when comparing L([CII)]) with L_{fir} determined from IRAS photometry because the IRAS spatial resolution is much poorer than the spaxels of PACS.

The [CII] line fluxes presented in Section 3.2.2 are measured by summing over 9 spaxels. The continuum flux densities are much weaker than the line and are often so weak in outlying spaxels that they are overwhelmed by noise. To minimize the effects of continuum noise, the continuum f_ν (158 μm) is determined by using the total f([CII)]) from Table 2 of [106] combined with EW([CII]) measured only in the brightest spaxel. These EWs are measured in all of our spectra and given in Table 2 of [106]. The uncertainties are often large, primarily because the continua are faint and have large uncertainties after back-

grounds are subtracted. The EW uncertainties that are given in Table 2 include the combined uncertainty of the total line flux and of the continuum level in the brightest spaxel, but uncertainties are dominated by the uncertainty in the continuum.

The νL_ν (158 μm) is compared to EW([CII]) in Figure 3-8 for all of the [CII] detections in Table 2 including AGNs, composites and SBs (the 10 non-detections are not used for this plot because their limits apply to both coordinates). Coordinates are in log units to make direct comparisons with the line to continuum ratio plots $L([CII])/L_{fir}$ used to discuss the deficit in previous references. Figure 3-8 shows similar ranges and dispersions of both values in all of the distributions for AGNs, composites, and SBs. The cosmic variance among individual sources is greater than any systematic differences between classes (shown more quantitatively in the discussion below of Figure 3-9).

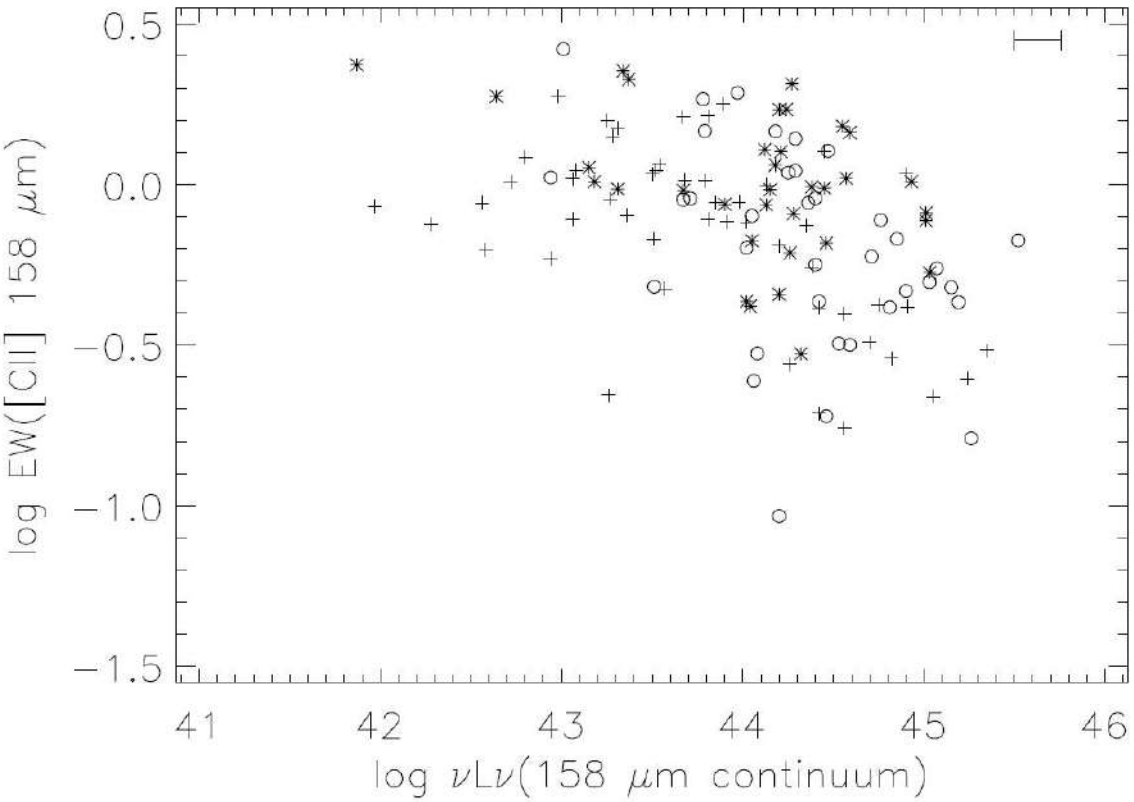

Figure 3-8. Far-infrared continuum luminosity at 158 μm, log νL_ν(158 μm) in erg s^{-1}, compared to the equivalent width of the [CII] emission line in μm for all sources in Table 2. Crosses are AGNs from the EW (PAH 6.2 μm) classification, open circles are

composite AGNs plus starburst, and asterisks are starbursts. Error bar shows the median uncertainty in luminosity determined by the observational uncertainty of continuum flux measurement.

The overall conclusion from Figure 3-8 is that the appearance of a "deficit" is much less conspicuous when using νL_ν (158 μm) than when using L_{fir}. For example, comparisons can be made with Figure 1 of [109] that compare L([CII])/L_{fir} to L_{fir} for their combined sample of AGNs, composites, and SBs. The luminosity range is comparable to that in Figure 3-8, >~10^3, but the range of line to continuum ratio is much greater in the comparison with L fir (~100), compared to a range of ~10 in Figure 3-8. Another conspicuous difference is the clear trend for the upper envelope of points to show a deficit when L([CII]) is compared to L_{fir}, but this trend is not apparent in Figure 3-8. Some high luminosity sources show EWs as large as some low luminosity sources. These results indicate that the apparent deficit becomes less significant when continuum luminosity is measured at the longest wavelengths, consistent with the interpretation that the coolest dust arises in the same SBs measured with the [CII], PAH, and neon features for SBs of all luminosities.

This conclusion can be further illustrated by comparing EW([CII]) with source classification based on EW (PAH 6.2 μm); if νL_ν (158 μm) and L([CII)]) both measure only the SB component of any source, the EW([CII]) should be independent of source classification. The results are shown in Figure 3-9, showing all EW([CII]) in Table 2 of [106]. The scatter increases for AGNs compared to SBs primarily because of increased uncertainties caused by fainter continua. For SBs, the typical observational uncertainty in EW (PAH 6.2 μm) given in Table 2 is only ~10% because the lines and continua are strong, but this uncertainty rises to ~50% for the weak lines and continua of the AGN.

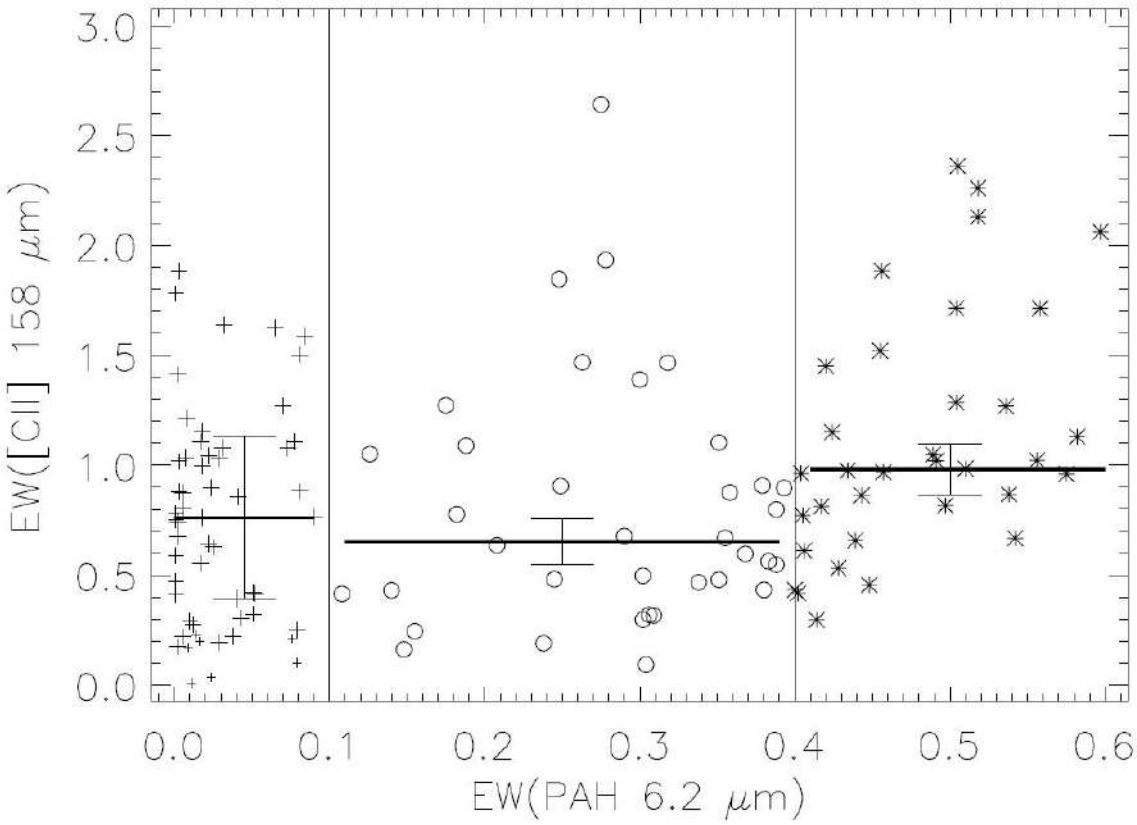

Figure 3-9. Equivalent width of [CII] 158 μm emission line in μm, with uncertainties, compared to EW (PAH 6.2 μm) classification, in μm. Medians are shown as horizontal lines in each class. Error bars show median 1σ uncertainties of the individual EW measurements for different classifications using uncertainties for each source given in Table 2 of [106]. Sources with upper limits in both EWs are not plotted or included in medians, but sources with upper limits only in EW ([CII]) are shown as small symbols (all AGNs).

The crucial result in Figure 3-9 is that the median EW ([CII]) is only marginally greater for SBs compared to composites and AGNs; within the uncertainty, a median value of EW ([CII]) = 0.9 μm falls within all error bars. For SBs, the median EW ([CII]) = 1.0 μm, decreasing to EW ([CII]) = 0.7 ± 0.4 μm for AGNs, and the difference is smaller than the dispersion in EW ([CII]) among individual SBs. The EW ([CII]) changes much less than EW (PAH 6.2 μm). The EW(PAH) ranges from <0.01 μm to 0.6 μm, a range of more than 60. This happens because an AGN has greatly increased mid-infrared continuum from warm dust compared to an SB, thereby decreasing EW (PAH 6.2 μm). By contrast, the

EW ([CII]) ranges from ~0.2 μm to <2 μm, a range of ~10. This result indicates quantitatively that the far-infrared continuum at 158 μm scales much more closely with the SB component of any source than does the continuum at shorter wavelengths. This result illustrates why the νL_ν (158 μm) could be a better estimate of SFR regardless of source classification than is L_{fir}, which includes shorter wavelength emission from hotter dust arising around AGNs.

3.3.4. SFR from the 158 μm Continuum

The preceding section shows that there is no conspicuous deficit when L ([CII)]) is compared to νL_ν (158 μm) for the full sample of AGNs, composites and SBs over all luminosities. Any systematic change in L([CII)])/νL_ν (158 μm) with luminosity or with classification is small compared to the cosmic variance at a given luminosity. This result encourages the conclusion that the far-infrared luminosity at 158 μm scales similarly with L ([CII]) in sources of all classifications and luminosity. This would make νL_ν (158 μm) a more reliable measure of SFR than the L_{fir}, if the latter sometimes includes an AGN component of luminosity.

It was concluded in Section 3.2 that log SFR = log L([CII]) – 6.93 ± 0.15 for SFR in M_0 yr^{-1} and L([CII]) in L_0, calibrated by comparison with the [NeII] and [NeIII] luminosities. The result derived independently in [75] by comparing [CII] luminosities with SFR derived from total infrared dust luminosity as in [10] was log SFR = log L([CII)]) – 7.08 ± 0.3. Both results agree within the uncertainties, so we take as an overall calibration combining these results that log SFR = log L([CII)]) – 7.0 ± 0.2. In both cases, the quoted uncertainties show only the cosmic variance among different SBs but do not reflect any systematic uncertainties in the underlying calibrations. The agreement of the two independent methods implies, however, that such systematic calibration uncertainties are smaller than the variance among sources.

Results for the EW ([CII]) in Figure 3-9 allow a transformation from SFR as measured from L ([CII)]) to SFR measured from νL_ν (158 μm). This leads to a comparison with another independent calibration. Using the median EW([CII]) of 1.0 μm for SBs alone to minimize any residual contamination by AGNs in the continuum, the relations among EW, L ([CII)]), SFR, and νL_ν (158 μm) yield log SFR = log νL_ν (158 μm) – 42.8 ± 0.2 for SFR in $M_\odot$ yr^{-1} and $\nu L_\odot$ (158 μm) in erg s^{-1} (to match units in Figure 3-8). For the luminosities of our sample shown in Figure 3-8, the resulting SFRs range over 0.8 < log SFR < 2.7.

A previous effort with the same objective but a completely independent calibration was by [101], who used 160 μm photometry with Spitzer for comparing continuum νL_ν (160 μm) to the SFR calibrated by H_α luminosity. Their sample consisted of 189 nearby star forming galaxies with generally low infrared luminosities which are not obscured luminous infrared galaxies (LIRGs) or ultraluminous infrared galaxies (ULIRGs) so that SFRs could be calibrated using H_α luminosities without any corrections for extinction. They caution that lower luminosity systems may have significant 160 μm luminosity from dust heated by stellar populations not associated with the current star formation, but they conclude that the νL_ν (160 μm) is dominated by ongoing star formation for νL_ν (160 μm) > 2×10^{42} erg s^{-1} (which encompasses all of our sources). Their resulting calibration is log SFR = log νL_ν (160 μm) – 42.85. This is nearly identical to our result even though derived with completely independent parameters.

The agreement is somewhat fortuitous because [101] use different relations between ionizing photons and SFR compared to those of [10] which were used for our calibration of SFR using bolometric luminosities. Calzetti et al. note that with the Kennicutt calibrations, their result would be log SFR = log νL_ν (160 μm) – 42.68. Although this gives an SFR measure from the 160 μm continuum that is formally 1.3 times larger than our result, it is within our uncertainties. The combined results of the two samples cover a factor of 100 in SFRs and a wide range of dust obscuration, implying a generalized validity to use of the 160 μm continuum as a measure of SFR so long as there is confidence that the dust continuum is dominated by stellar heating.

A calibration of SFR from L_ν (158 μm) was also determined by [110] for a sample of 25 ULIRGs (dominated by AGNs) for which they observe [CII] and continuum fluxes. Their calibration of SFR arises from an earlier comparison [58] between PAH (6.2 μm + 11.3 μm) luminosities and SFRs determined from [NeII] and [NeIII] luminosities using the results of [100]. By comparing SFRs determined from these PAH luminosities with the observed L_ν (158 μm) for the 25 ULIRGs, they determine an empirical relation between SFR and continuum luminosity density that log SFR = 3.36 ± 0.22 + (1.42 ± 0.30) log L_ν (158 μm), for luminosity density in $L_\odot$ per Hz. The nonlinear luminosity dependence implies that a greater SFR is measured from continuum luminosity compared to PAH luminosity as luminosity increases, which is consistent with having a residual contamination of L_ν (158 μm) from AGN luminosity for increasing luminosities. Within the uncertainties of this fit and the luminosity dependence, our results for SFRs are similar. For example, at log νL_ν (158 μm) = 45 in erg s^{-1}, or log L_ν (158 μm) = –0.86 in $L_\odot$ per Hz, our calibration from pure SBs yields log SFR = 2.2 ± 0.2 compared to the Farrah et al. result of 1.7 < log SFR < 2.6.

The uncertainty within our results that is introduced when using νL_ν (158 μm) to measure SFR compared to using L ([CII)]) in sources of different classification can be estimated from the differences among EW ([CII]) for different classifications in Figure 3-9. If some of the νL_ν (158 μm) for AGNs and composites arises from dust heating by an AGN, then EW ([CII]) should be less for these sources compared to SBs. Adopting the median EW ([CII]) = 1.0 μm as the measure of line to continuum ratio for pure SBs leads to an estimate of the SFR error that would derive from use only of the continuum for AGN or composite sources. The error in the SFR measure is inversely proportional to the EW; for example, an EW ([CII]) = 0.5 μm would mean a continuum twice as strong as from SBs, so the continuum alone would lead to an overestimate of SFR by a factor of two compared to the SFR measured from [CII]. For AGNs, the median EW ([CII]) = 0.7 μm, which implies a systematic overestimate of SFR by a factor of 1.4 if using only the far-infrared continuum as the SFR indicator in AGNs. For AGNs, 21/56 have EW ([CII]) < 0.5 μm, leading to an overestimate of SFR from the continuum alone by more than a factor

of two in ~40%. Although these results lead to smaller discrepancies in SFR than would be measured using only L_{fir}, confidence in measuring SFR within a factor of two from continuum luminosities alone requires confidence that the source is dominated by a SB without continuum contamination by an AGN.

3.4. Summary and Conclusions

New [CII] 158 μm observations of 18 sources with the Herschel PACS instrument are presented, and a summary of our total sample of 130 [CII] sources is given that covers a wide range of AGN to SB classifications as derived from PAH strength. New redshifts derived from [CII] and line to continuum strengths (EW of [CII]) are given for the full sample.

Results for 112 sources are compared with emission line fluxes from high resolution Spitzer IRS spectra. A new calibration of [CII] as an SFR indicator is determined by comparing [CII] fluxes with mid-infrared [NeII] and [NeIII] emission line fluxes. This independently gives the same result as determining SFR using bolometric luminosities of re-radiating dust from SBs: log SFR = log L ([CII)]) – 7.0 ± 0.2, for SFR in M_0 yr^{-1} and L ([CII]) in L_0. This confirms that [CII] measures the same SB component of sources as measured with mid-infrared PAH and neon emission line diagnostics.

The line to continuum ratio measured at 158 μm, EW ([CII]), changes little with luminosity or with classification, indicating that the far-infrared continuum at 158 μm arises primarily from the SB component of any source. For pure SBs, the continuum alone gives log SFR = log νL_ν (158 μm) – 42.8 ± 0.2 for SFR in M_0 yr^{-1} and νL_ν (158 μm) in erg s^{-1}. The change of EW ([CII]) with classification (median EW ([CII]) = 1.0 μm for SBs compared to 0.7 μm for AGNs) implies a systematic overestimate of SFR in AGNs by a median factor of 1.4 if using only the far-infrared continuum at 158 μm as an SFR indicator.

4. NEON AND [CII] 158 μm EMISSION LINE PROFILES

A sample of 379 extragalactic sources is presented that has mid-infrared, high-resolution spectroscopy from the Spitzer Infrared Spectrograph (IRS) and also spectroscopy of the [CII] 158 μm line from the Herschel Photodetector Array Camera and Spectrometer (PACS). The emission line profiles of [NeII] 12.81 μm, [NeIII] 15.55 μm, and [CII] 158 μm are presented, and intrinsic line widths are determined (full width half maximum of Gaussian profiles after instrumental correction). All line profiles, together with overlays comparing the positions of PACS and IRS observations, are made available in the Cornell Atlas of Spitzer IRS Sources. Sources are classified from active galactic nucleus (AGN) to starburst based on equivalent widths of the 6.2 μm polycyclic aromatic hydrocarbon feature. It is found that intrinsic line widths do not change among classifications for [C II], with median widths of 207 km s^{-1} for AGNs, 248 km s^{-1} for composites, and 233 km s^{-1} for starbursts. The [Ne II] line widths also do not change with classification, but [Ne III] lines are progressively broader from starburst to AGN. A few objects with unusually broad lines or unusual redshift differences in any feature are identified.

4.1. Introduction

More recently, numerous observations of the [CII] line have been made [75, 106, 110, 116, 109, 20] using the Photodetector Array Camera and Spectrometer (PACS) instrument [73] on the Herschel Space Observatory [72] and have included many sources that had previously been observed by the IRS. Our own previous studies were specifically designed to compare the [CII] line luminosities to mid-infrared PAH emission features and mid-infrared emission lines observed with the IRS in order to calibrate the star formation rate (SFR) using the [CII] line. We found that [CII] luminosities most closely track [NeII] luminosities, from which we concluded that the [CII] is showing PDRs associated with the HII regions seen in [NeII].

The observational study of forbidden emission line profiles has long been a key technique for classifying and understanding active galaxies. The most extensive early studies used the optical [OIII] line at 0.50 μm, from which a conclusion was reached that the width of this line could generally distinguish AGNs and starbursts [117, 118]. All conclusions based on optical lines were restricted to sources with little extinction by dust, however, which led to uncertainties in interpreting differences among profiles if different components of sources had different values of extinction. Now that forbidden emission line profiles are available in the mid-infrared and far-infrared, comparisons can be made without this uncertainty. An initial indication that such line profiles provide interesting results is in the line profile comparisons by [119], which features among 24 ultraluminous galaxies (ULIRGs), done with the goal of seeking outflows from AGNs.

To further evaluate the utility of the [CII] line for understanding AGNs and starbursts, in this paper we compare the [CII] emission line profiles to the mid-infrared diagnostics for all extragalactic sources that have archival observations available for both PACS [CII] and IRS spectra. This study of line profiles is an extension of previous analyses of total [CII] line fluxes. We present emission line profiles for [CII], [Ne II] 12.81 μm, and [NeIII] 15.55 μm for extragalactic sources that have archival observations available for both PACS [CII] and IRS high-resolution spectra. Our resulting sample of 379 extragalactic sources includes all sources with both [CII] and IRS high-resolution observations, except for nearby extended galaxies for which IRS observations were made in a mapping mode. The latter are omitted because our overall goal is to understand the global properties of sources that would generally be unresolved at high redshift. There are 390 [CII] profiles in our total sample, representing 379 different IRS pointings (the remaining 11 are duplicate [CII] observations made at the same IRS position).

We present the source list and measurements of line widths and redshifts, along with overall comparisons among line widths. All of the [CII] line profiles with Gaussian fits are made available in the Cornell Atlas of Spitzer/IRS Sources (CASSIS; [74, 120].

4.2. Observations

4.2.1. Sample Selection

Our sample was selected by examining the abstracts of Herschel observing programs that described observations of extragalactic emission line sources 5 and then studying archival sources from these programs to identify those for which the [CII] line was observed, either in line or range spectroscopy. Once all extragalactic sources with [CII] observations were identified, we searched for these sources in CASSIS to locate sources with high-resolution IRS observations, necessary for line profile information. The individual Herschel observing programs and the number of sources taken from each are SDP-esturm-3, DDT-esturm-4, and KPGT-esturm-1(56); KPGT-smadde01-(13); KPOT-pvanderw-1(11); GT1-lspinogl-4 and GT2-lspinogl-6(14); OT1-dfarrah-1 and OT2-dfarrah-5(23); OT1-dweedman-1(112); OT1-larmus-1(136); OT2-tdiazsan-1 (4); OT1-lyoung-1(5); OT1-nwerner-1(3); OT1-sveilleu-2(1); OT2-idelooze-1(1); OT2-lsargsyan-1(2); OT2-nnesvadb-3(2); OT2-pguillar-7(5); KPOT-aedge-1(1); and OT1-bweiner-1(1). Although we intended a complete search, it is possible that some sources with both [CII] and IRS high-resolution observations have been overlooked. The source list and all results are given in Table 1 of the [121] paper.

4.2.2. IRS High-resolution Spectra

A few previous studies have determined line widths from IRS high-resolution spectra [122, 65, 119]. These results have all been approximated by applying a uniform estimate of the instrumental resolution using the typical resolution of ~500 km s^{-1} for the FWHM of the instrumental profile that is listed in the instrument description. For our analysis, we apply two additional steps for improving the determination of the instrumental profile. The first

is to determine empirical instrumental profiles for individual emission lines, and the second is to apply an "optimal" extraction for the high-resolution spectra, which enhances the signal-to-noise ratio (S/N) for unresolved sources. These steps are described below.

Spectral extraction is the process of producing a one-dimensional spectrum from the two-dimensional images obtained with the IRS detectors. The best possible extraction of unresolved sources applies the point-spread function (PSF) of the telescope/spectrograph combination so that the pixels in the cross-dispersion direction are weighted by the fraction of source flux that falls on them, thereby reducing the background and instrumental noise. This is defined as an "optimal" extraction. These extractions have been implemented for the spectra shown in CASSIS using empirically determined PSFs for both low-resolution [74] and high-resolution [120]. If a source is fully extended over the observing aperture, a better alternative is a full aperture extraction that equally weights all pixels within the aperture. The choices provided in CASSIS for spectral extractions of high-resolution IRS spectra are described in detail by [120]. All previous measures of IRS high-resolution spectra have used full aperture extractions, which are provided by the "post-BCD" spectra of the Spitzer Heritage Archive.

For both low-resolution and high-resolution spectra, the source extent is estimated in CASSIS by noting differences between the source spatial profile compared to the PSF. This estimate is more reliable for low-resolution spectra than for high-resolution because of the limited spatial profile sampling in high-resolution; the PSF has an FWHM of about 2 pixels compared to the 6 pixel length of the high-resolution slits. The majority of our sources are not extended on the scale of the observing aperture, so our final adopted measurements utilize the optimal extraction. For our objective of measuring line profiles, the best possible S/N is crucial in order to obtain the best profiles. This also leads to the choice of optimal extraction even if some flux is underestimated for extended sources.

The extraction labeled as "optimal" in CASSIS uses a simultaneous fitting to the two separate observing nod positions. This option also provides an estimate of the underlying background by using residuals beneath the fitted PSF. Another alternative, "optimal differential," which differences the two nods before fitting the PSF profile, is also given in

CASSIS for comparison to help with removing bad pixels, but this method gives a reliable flux calibration only for unresolved sources. CASSIS illustrates both of the optimal extractions in addition to a full aperture extraction so that users can make a final choice, but recommends “optimal” if the source appears spatially unresolved.

The IRS instrumental spectral resolution for the high-resolution modes is approximately defined by the two pixel projected width of the observing aperture. Spectral resolution varies among different lines because the IRS high-resolution spectrographs are echelle spectrographs with different lines seen in different orders, so resolution increases as the order increases. Because our objective is the best possible measurement of line widths, the instrumental resolutions for the [NeII] and [NeIII] lines presented in this paper are measured empirically. This is done using spatially unresolved planetary nebulae in which these emission lines are strong. The intrinsic widths of planetary nebula emission lines are much smaller than the IRS instrumental line width, so the observed line profiles illustrate the instrumental profile.

The sources used are the planetary nebulae from the Large Magellanic Cloud, the Small Magellanic Cloud, and the Galactic Halo included in [123] and [124]. Because these planetaries are spatially unresolved, the CASSIS optimal extraction is used to measure the lines. Gaussian fits match the observed profiles well, so we adopt instrumental profiles that are Gaussians described by the FWHM of the planetary nebula profiles.

The FWHM and dispersion among individual planetaries are FWHM ([NeII]) = 331 ± 35 km s^{-1} and FWHM ([NeIII]) = 377 ± 35 km s^{-1}. The somewhat better resolution for [NeII] 12.81 μm is expected, because this line is in short-high order 16, whereas [NeIII] 15.55 μm is in order 13. These instrumental line widths were also measured using full aperture extractions; the full aperture extractions give consistent but slightly larger median widths compared to the optimal extractions, 371 km s^{-1} for [NeII] and 465 km s^{-1} for [NeIII]. These differences can be explained by small tilts of the observing slits compared to the dispersion direction of the spectra. The optimal extractions give more weight to the center of the slit where any line smearing from tilt effects is negligible, but the full extractions

equally weight flux near the edges, where slit tilts would produce a larger shift of the dispersed image.

Because the optimal extraction is used for sources in this paper, we adopt as the instrumental resolution profile (FWHM res) the values of 331 km s^{-1} for [NeII] and 377 km s^{-1} for [NeIII], with an uncertainty of about 10% for each. The intrinsic FWHM intrinsic of the observed spectral lines in sources are then determined as $FWHM_{intrinsic}^2 = FWHM_{observed}^2 - FWHM_{res}^2$.

Redshift measurements for sources depend on the position of the line centroids, which depend on the wavelength calibration of the spectra ("WAVESAMP" files). This calibration is applied differently in optimal and full aperture extraction. To determine any systematic uncertainties arising from the extraction technique, we compared line centroids for the planetary nebulae and found that the 1σ dispersion between full aperture and optimal extractions for the neon lines is ±25 km s^{-1}. These results mean that redshift uncertainties arising from different analysis techniques for the high-resolution spectra are only ±0.00008.

The observed results for line widths from the CASSIS optimal extractions are given in Table 1 of [121]. All IRS emission lines, including those obtained with the alternative extractions, can be examined within CASSIS by source name or coordinate using the browse tools provided without requiring any downloads of the spectra. The CASSIS results provide the actually observed coordinate of the source, which sometimes differs from the nominal coordinate corresponding to the source name in other databases. In "cluster" mode for IRS observations, several independent sources may be included within the same AOR, and these sources are sometimes components of the same galaxy. For these reasons, it is necessary to use the accurate coordinates from CASSIS for comparisons to locate the PACS spaxel corresponding to the same position, and these coordinates are in Table 1 of [121].

To determine uncertainties in FWHM for line profiles depending on extraction technique, we compared both full aperture and optimal extractions for the [NeII] and [NeIII] lines in

all sources. Line profiles were measured using Gaussian fits to the [NeII] and [NeIII] emission lines with a first order underlying continuum, fitting with the Spectroscopic Modeling Analysis and Reduction Tool [79, 125]. The dispersions among the differences between full aperture and optimal extractions for the same profiles are a measure of the observational uncertainties that arise from independent fitting of undersampled profiles with different Gaussians. For both lines, these dispersions (±50 km s^{-1} for [NeII] and ±46 km s^{-1} for [NeIII]) are ~10% of the observed median line width (470 km s^{-1} for [NeII] and 512 km s^{-1} for [NeIII]).

Dispersions are a larger fraction of the measured width for narrower lines, so the fractional uncertainty is greater for narrow lines. This effect is an additional reason to prefer optimal extractions for the line measurements. In some cases, the observed FWHM from the best Gaussian fit is smaller than the instrumental resolution, which cannot be physically correct. In these cases, the adopted intrinsic FWHM is arbitrarily listed as 100 km s^{-1} and is displayed at that value in figures so that these anomalous cases can be recognized. There is an offset in measured FWHM such that the full aperture measures are systematically larger, by 20 km s^{-1} for [NeII] and 70 km s^{-1} for [NeIII]. We attribute this difference to a similar effect as noted above for instrumental resolution—that weighting all pixels of the tilted slit evenly in the full aperture extraction leads to a smearing of the line in the direction of dispersion, which artificially increases the line width.

4.2.3. Herschel PACS [CII] Spectra

The PACS instrument [73] simultaneously obtains spectra at 25 positions in a source with square apertures called “spaxels”. If all sources were spatially unresolved and all pointings were perfect, direct comparisons of lines observed with IRS and PACS would be straightforward. Although neither condition is perfectly met for all of these observations, both the IRS slit and a PACS spaxel observe similar fractions of a source. The IRS short-wavelength, high-resolution observing slit for the neon lines is 4.7” wide, designed to

match approximately the FWHM of the telescope diffraction profile at these wavelengths. The PACS spaxels are 9.4” wide, also nearly equal to the FWHM of the Herschel diffraction profile at the [CII] wavelength. Because of this similarity in the fraction of a source observed by the two spectrographs, we compare the line profiles seen in the IRS slit to the [CII] profile seen in the single PACS spaxel that is closest in location to the IRS slit, as illustrated in Figure 4-1.

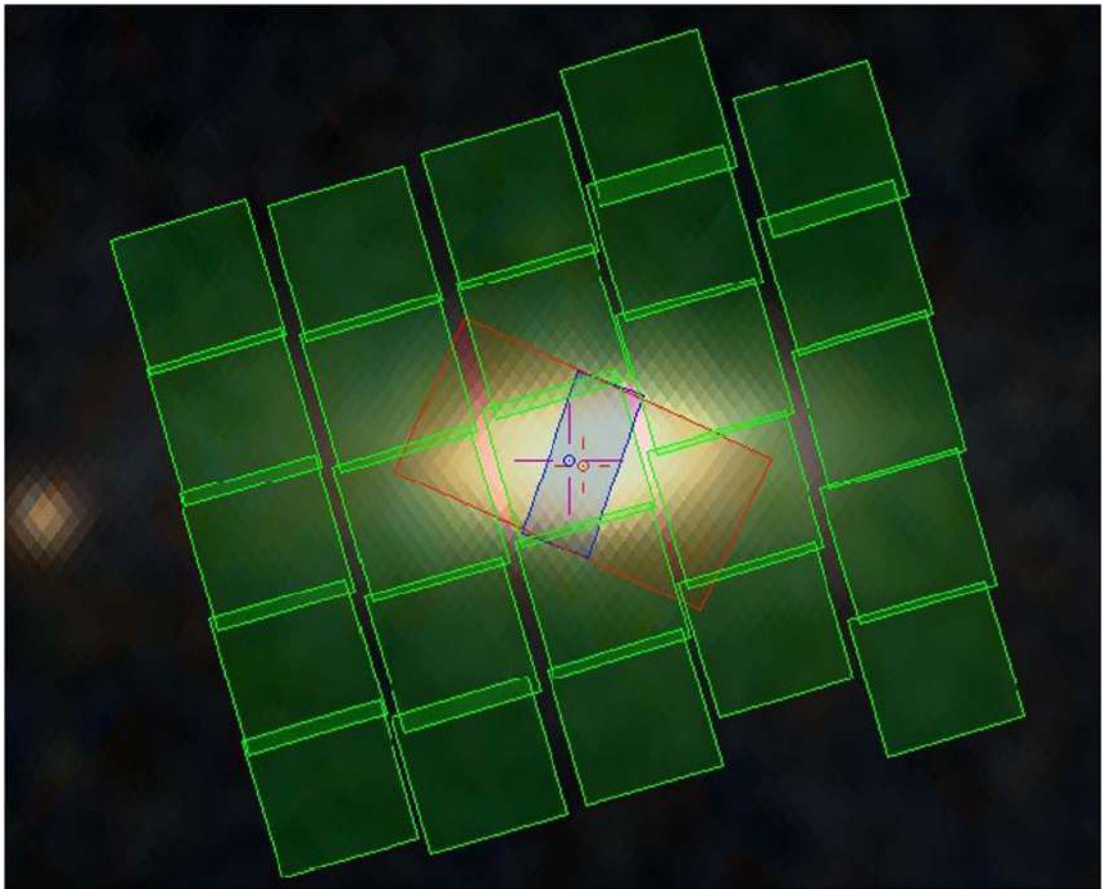

Figure 4-1. Example of PACS spaxels compared to IRS high-resolution slits, for source Markarian 18. Squares are spaxels of size 9”.4×9”.4; the large rectangle is the IRS long-high slit, and the small rectangle is the IRS short-high slit. Crosses show coordinates of the source in IRS slits. All neon lines measured are in the short-high slit. The closest spaxel to the position of the IRS slit is identified in Table 1 of [121]; the numbering convention used in Table 1 for rows and columns of spaxels is as follows. The upper left is 5, 5, the lower left is 5, 1, the upper right is 1, 5, and the lower right is 1, 1. East

is to the left and north is the top of the image. These overlays for all sources are shown in CASSIS at http://cassis.sirtf.com/herschel.

A factor that might affect profile widths in spatially resolved sources is the size of the emitting region observed by PACS. These sizes vary by a large amount because distances range from 0.05 to 1003 Mpc. In Table 1, we list the projected sizes of the PACS 9.4" spaxel based on the angular size distances to the sources. Redshift-independent distances are used if these are listed in the NASA/IPAC Extragalactic Database (NED). If not, redshift-derived distances are determined from [126] using H_0 = 71 km s^{-1} Mpc^{-1}, Ω_M = 0.27, and Ω_L = 0.73. The distribution in projected spaxel size among sources in Table 1 is shown in Figure 4-2. The distributions illustrate that the PACS results refer primarily to global properties of sources on observed scales of many kiloparsecs.

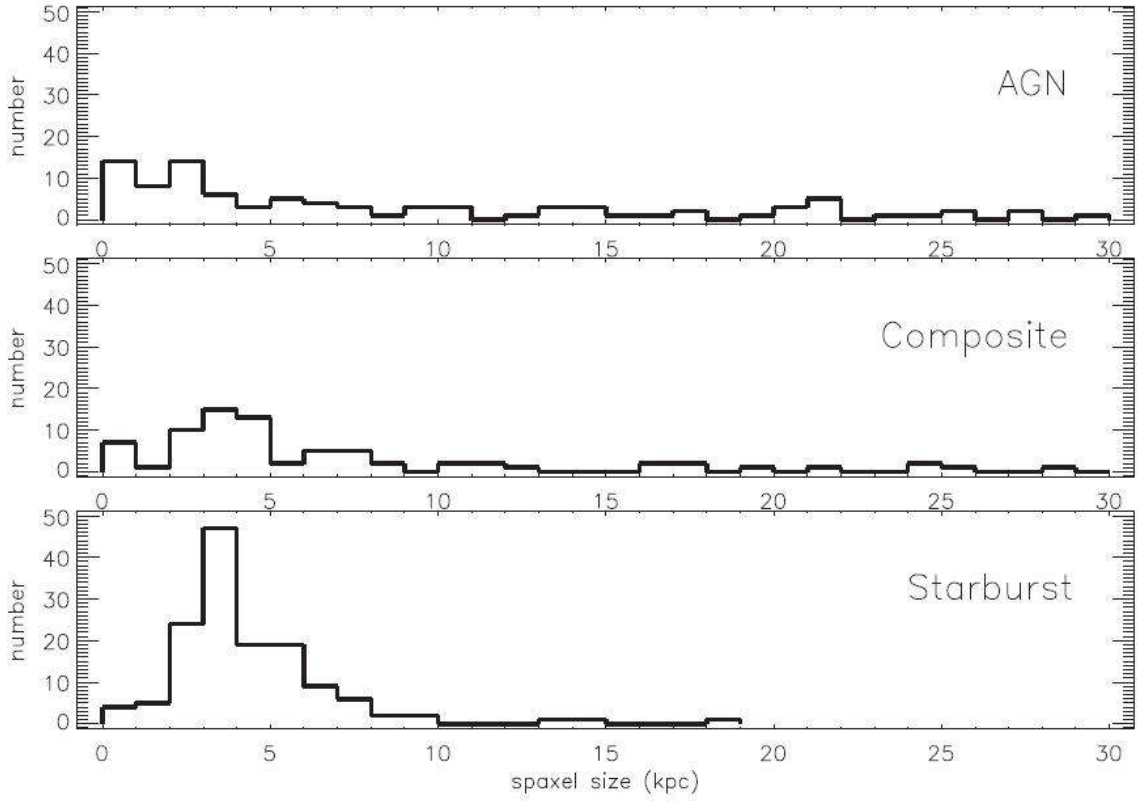

Figure 4-2. Distributions in projected size of 9.4" PACS spaxel among all sources in Table 1 of [121]. Histograms show the actual number of sources of different classifications in each bin of width one kpc.

For our studies of line profiles, an important consideration is to match the position of a PACS spaxel to the position of the IRS aperture. We did this individually for each source, producing overlays of PACS spaxels and IRS aperture using the observed positions given in the headers for the final IRS spectra, the coordinates in Table 1. Overlays such as the example in Figure 4-1 are shown in CASSIS for all of our sources. The individual spaxel corresponding most closely to the position of the IRS aperture is listed in Table 1, using the numbering convention shown in Figure 4-1, and the profile from this spaxel is the [CII] profile shown in CASSIS.

All [CII] observations were reduced with version 12.1.0 of the Herschel Interactive Processing Environment (HIPE), together with the "PACSman" software [80], to fit line profiles and continuum within the spaxels. An illustration of a Gaussian line fit provided by PACSman is in Figure 4-3, and all profiles that we use are shown for the individual sources in CASSIS, searchable by source name or coordinate. Displaying Gaussian fits is particularly useful for seeking sources that might have a core Gaussian but broad or asymmetric underlying wings (e.g., [127]). There are 34 sources in our sample for which [CII] was observed but yields a profile with insufficient S/N for an accurate width or radial velocity measurement. These profiles are shown as "no data" in Table 1, but they are illustrated in CASSIS with an attempted Gaussian profile fit at the line position.

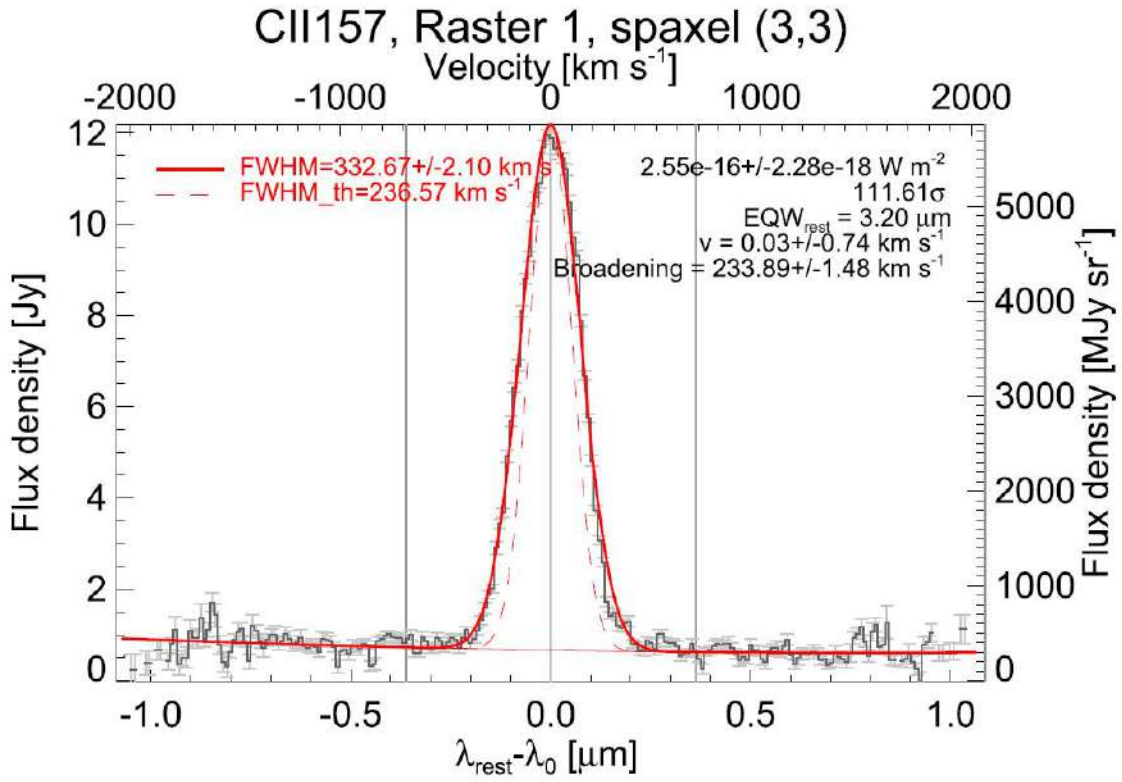

Figure 4-3. Example of a [CII] profile produced by PACSman and displayed in CASSIS, for the source Markarian 18. The fit by PACSman produces the FWHM and uncertainty of the observed Gaussian profile (solid line) fit to the data points (broken line and error bars), together with line flux and equivalent width. The line profile is shown at the [CII] redshift given in Table 1 of [121], corrected to the local standard of rest. Any assumed instrumental width (FWHM-th; dashed line) may be input to yield intrinsic width (Broadening) after removing this instrumental width from the observed profile. The instrumental FWHM used for all sources in this paper is 236 km s^{-1}, determined empirically from observations of 30 Doradus, so intrinsic widths given in Table 1 are determined as $FWHM_{intrinsic}^2 = FWHM_{observed}^2 - 236^2$. All profiles used in this paper and the observed FWHM are illustrated in CASSIS, available at http://cassis.sirtf.com/herschel , although slightly different values of FWHM-th are sometimes shown for illustration. For noisy profiles with an observed FWHM fit of <236 km s^{-1}, an artificial value of FWHM-th is shown in the profiles so that the value determined for "broadening" remains positive. In Table 1, all profiles with observed FWHM < 236 km s^{-1} are arbitrarily assigned values of 100 km s^{-1} for intrinsic width.

As was done for the IRS spectra, we determined an empirical instrumental profile for the [CII] observations. This was done using all 25 spaxels in the observation of the 30 Doradus HII region listed in Table 1, because all spaxels give the same observed FWHM, the intrinsic line widths are small compared to the instrumental resolution, and the intrinsic line widths are known. The observed FWHM among these 25 profiles is 239 km s^{-1}. Internal motions within the HII region have been measured for the optical [OIII] 0.50 μm line and have a median FWHM of 45 km s^{-1} at spatial resolutions similar to PACS [128]. Removing this intrinsic width from the width observed by PACS results in an instrumental FWHM of 236 km s^{-1}. The intrinsic FWHM intrinsic of the observed [CII] lines in sources are then determined as $FWHM_{intrinsic}^2 = FWHM_{intrinsic}^2 - 236^2$. The intrinsic widths are listed in Table 1.

4.3. Analysis of [CII] and Neon Line Profiles

Our primary objective for the present paper is to present the measurements in Table 1 and the profiles in CASSIS, which together provide an observational atlas of [CII] 158 μm, [NeII] 12.81 μm, and [NeIII] 15.55 μm line widths that can be used for comparing among various properties for a wide variety of sources. Our eventual objective is to understand in more detail what determines line widths in different galaxies. For now, we only use these results to determine if there are trends with classification as AGN or starburst, or any systematic differences among [CII] and mid-infrared neon lines.

4.3.1. Comparisons of Line Profile Widths

Previous studies using IRS line widths found some indications that higher ionization lines sometimes show broader widths or outflow effects from AGNs, but these effects were found primarily for the high ionization [SIV] and [OIV] lines in a few cases of sources with

the broadest lines [122, 65, 119]. We emphasize the lower ionization neon lines, especially [NeII], because this line most closely tracks [CII] in comparisons of line fluxes [106]. These neon lines are also the best for comparison with previous studies of line profiles of the strongest optical forbidden line, [OIII] 0.50 μm [117, 118, 129], because of similar ionization potentials (21.6 eV to produce Ne II, 41.0 eV to produce NeIII, and 35.1 eV to produce OIII).

The AGN/starburst classification used here, based on the strength of the 6.2 μm PAH feature, is similar to that used in many previous studies, although different authors use different PAH features and different methods for measuring strength (e.g., [78, 102, 56, 57, 60, 62, 63, 107, 64, 66]. The essential result used by all of these authors is that the PAH features increase in strength as the starburst component increases, although different authors adopt somewhat different definitions of AGN-dominated compared to starburst-dominated. The quantitative divisions illustrated in our results are that AGN have EW (6.2 μm) < 0.1 μm, composite AGN plus starburst have 0.1 μm < EW (6.2 μm) < 0.4 μm, and starbursts have EW (6.2 μm) > 0.4 μm.

The divisions we use began with an IRS spectroscopic survey of starburst galaxies by [56] and in a flux-limited IRS survey of sources including all classifications [98], subsequently verified by comparison with optical classifications using several hundred IRS spectra [64]. Our primary motive for using the 6.2 μm feature instead of the stronger 11.3 μm feature has been to allow classification of sources with sufficiently high redshifts that the 11.3 μm feature is not visible in IRS spectra. The strongest PAH complex centered at 7.7 μm is not used because this feature can be confused with an apparent spectral peak at similar wavelengths that arises because of strong absorption on either side of the peak in heavily obscured AGNs. By illustrating various parameters regarding line profiles as functions of EW (6.2 μm), any trends with AGN/starburst classes are readily seen.

The well-established correlation between level of ionization and PAH classification of AGNs and starbursts is illustrated in [106] for various flux ratios among mid-infrared and [CII] emission lines as a function of PAH classification. For our present concerns, the important result is that the [NeII] line tracks [CII] independent of classification, whereas

the higher ionization [NeIII] line is stronger relative to [CII] in AGNs than in starbursts. (The ratio of line fluxes for [NeIII]/[NII] for the optimal extractions is given in Table 1 for each source.) This implies that the line profiles from [NeIII] should be more affected by the AGNs, whereas the [NeII] and [CII] lines should characterize the starburst component. We first consider, therefore, whether line profiles for these three features show any differences between AGNs and starbursts.

Comparisons of AGN/starburst classification with intrinsic line widths (those given in Table 1, after correction for instrumental broadening) are shown in Figures 4-4 – 4-6. We think that the most important result is shown in Figure 4-4 for [CII] because a primary goal of our study is to seek any evidence that the [CII] line width is a diagnostic of AGN/starburst classification. There is no evidence of any trend, however. The medians and dispersions among [CII] line widths in Figure 4-4 are very similar for all classifications, with medians of 207 km s^{-1} for AGNs, 248 km s^{-1} for composites, and 233 km s^{-1} for starbursts with dispersions in all cases of about ±130 km s^{-1}. The most important result for [CII] in Figure 4-4, therefore, is that line widths do not change among classification, indicating that [CII] is dominated by the starbursts within any source and are not affected by the presence of an AGN. This confirms our conclusions in [75, 106] based only on line fluxes.

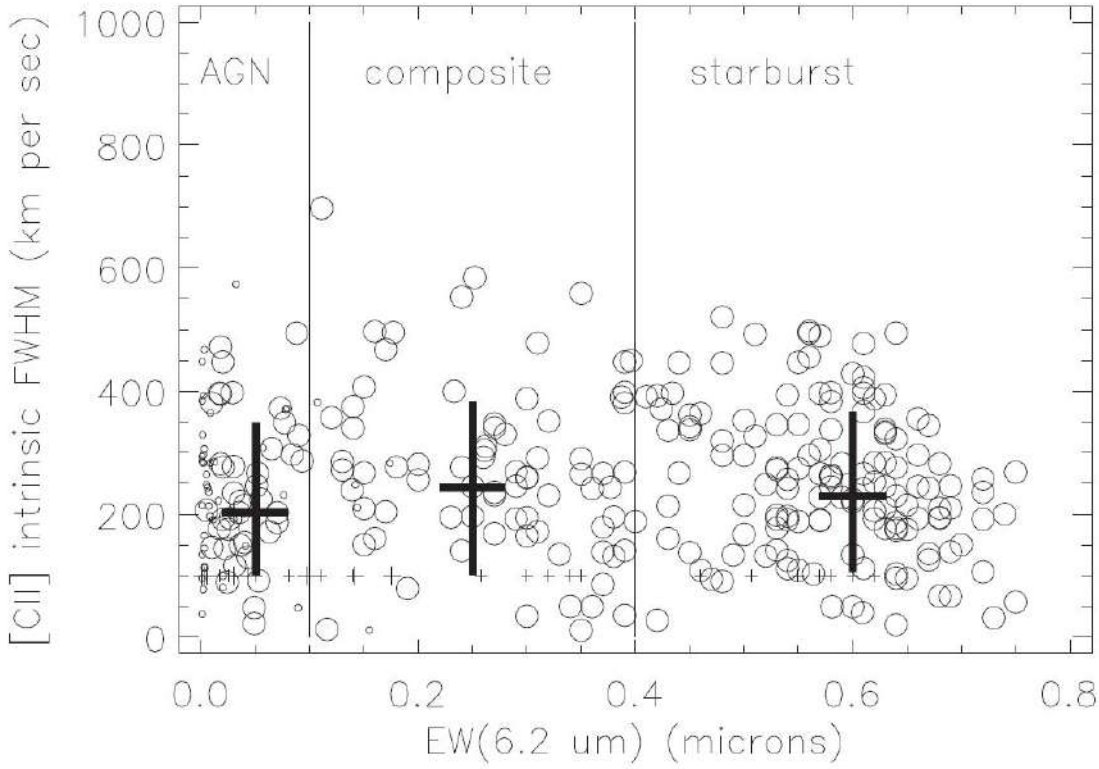

Figure 4-4. Intrinsic FWHM of [CII] 158 μm in km s^{-1} compared to EW (6.2 μm) from Table 1. Large crosses show the median line width and 1σ dispersion of line widths within classifications. Thin vertical lines divide classifications; AGNs have EW (6.2 μm) < 0.1 μm, composite AGNs plus starburst have 0.1 μm < EW (6.2 μm) < 0.4 μm, and starbursts have EW (6.2 μm) > 0.4 μm. Small symbols are sources with measured line widths but upper limits in EW (6.2 μm). Small crosses are sources in which the observed FWHM appears to be smaller than the instrumental resolution so the FWHM is arbitrarily assumed as 100 km s^{-1}. Observational uncertainty for [CII] FWHM is typically smaller than the size of symbols; uncertainties for each source are displayed in CASSIS.

The results for [NeII] in Figure 4-5 show a similar result to [CII], with only a slight trend of increased widths for AGNs; the median FWHM for AGNs and composites is 340 km s^{-1} compared to 300 km s^{-1} for starbursts. The best comparison with [CII] is for the starbursts to rule out any broadening of [NeII] by an AGN. For starbursts, the difference between the median FWHM of 233 km s^{-1} for [CII] and 300 km s^{-1} for [NeII] is interesting,

but we cannot be confident that it is meaningful. This difference is less than the uncertainty in the individual IRS width measures shown in Figure 4-5. The difference would disappear if we assume a broader instrumental line width for [NeII] than we have adopted, requiring an instrumental width of 380 km s^{-1} instead of the 331 km s^{-1} that is used. This larger value is close to the full aperture instrumental width discussed in Section 4.2.2, but such a large instrumental width would not be appropriate for unresolved sources, which require an optimal extraction. If this larger instrumental width were used, full aperture extractions would also have to be used, and these are systematically larger than the optimal extraction widths that are given in Table 1. The net result would remain that intrinsic widths for [NeII] are greater than those for [CII]. We must conclude, therefore, that we cannot precisely compare the [CII] widths from PACS with the neon widths from the IRS because of uncertainties in determining the most accurate extraction procedure for the IRS lines.

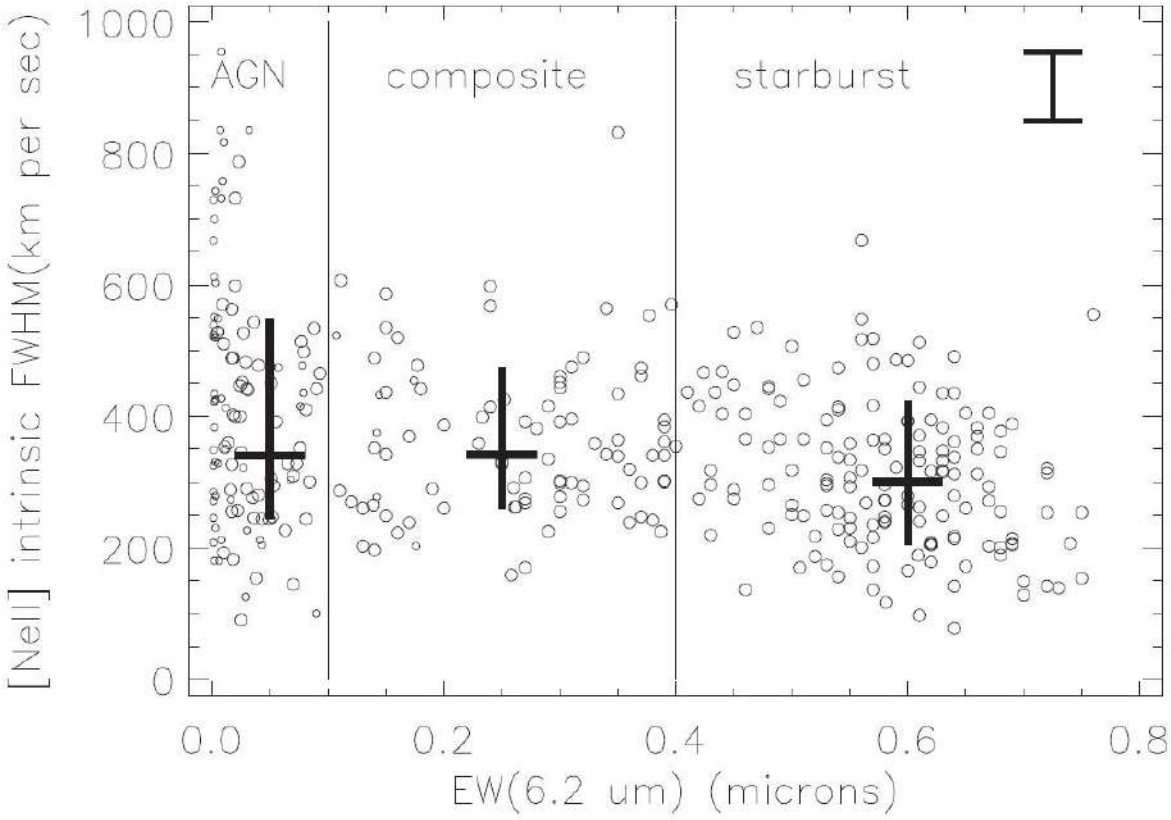

Figure 4-5. Intrinsic FWHM of [NeII] 12.81 μm in km s^{-1} compared to EW (6.2 μm) from Table 1. Symbols and explanations are the same as in Figure 4-4, with an additional error bar that shows 1σ dispersion of differences between full aperture and optimal extractions of the same line profiles, which is the measure of uncertainty adopted for observed FWHM, discussed in Section 4.2.2.

Despite these uncertainties among comparisons of [CII] and neon line widths, the relative widths between the [NeII] and [NeIII] lines are meaningful. Unlike the [NeII] FWHMs in Figure 4-5, the [NeIII] FWHMs in Figure 4-6 show a trend for increasing line widths from starbursts through AGNs. Both the median values of line widths and the upper values of the dispersions are progressively larger from starbursts through composites to AGNs, with medians of 289 km s^{-1} for starbursts, 367 km s^{-1} for composites, and 426 km s^{-1} for AGNs. Upper values of the observed 1σ dispersions are 417 km s^{-1} for starbursts, 580 km s^{-1} for composites, and 748 km s^{-1} for AGNs. This trend for AGNs to be offset to larger values of intrinsic [NeIII] line width is independent of the adopted value for [NeIII] instrumental width and demonstrates that some additional [NeIII] line broadening is associated with AGNs. This is additional confirmation that we should not expect similar profiles between [CII] and higher ionization features such as [NeIII] because they often arise in different physical regions of sources.

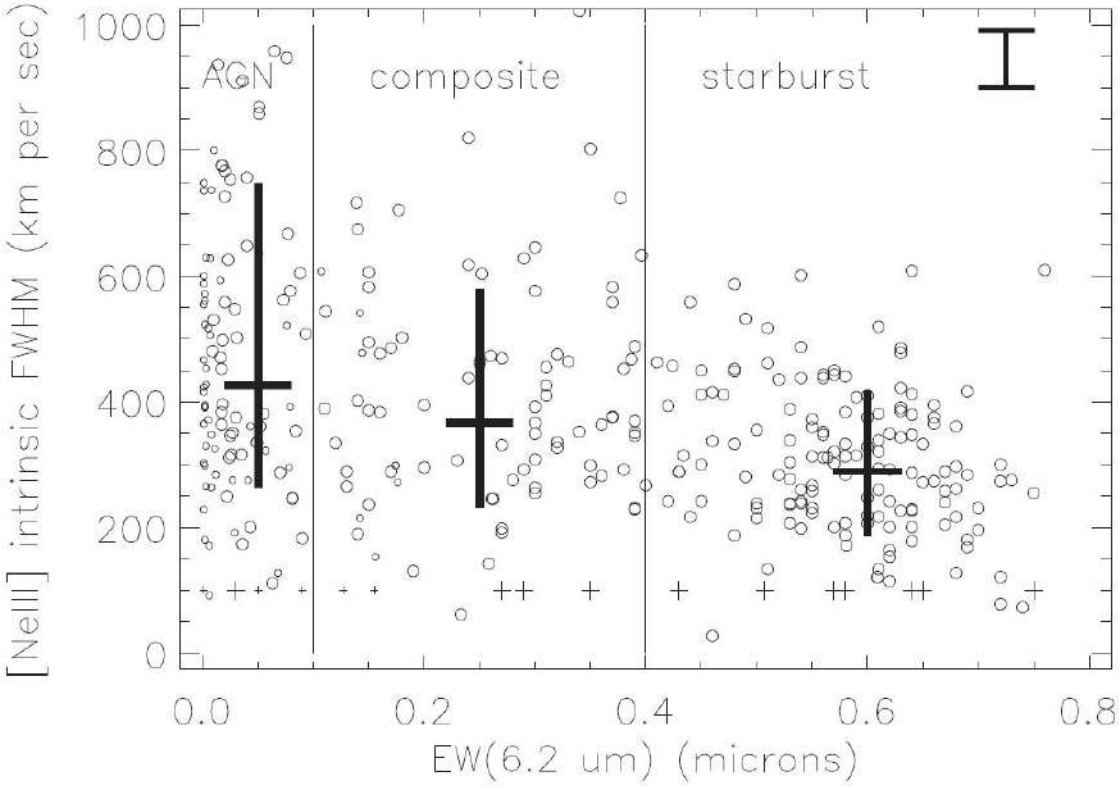

Figure 4-6. Intrinsic FWHM of [NeIII] 15.55 μm in km s^{-1} compared to EW (6.2 μm) from Table 1. Symbols and explanations are the same as in Figures 4-4 and 4-5.

Having confirmed that [CII] and [NeII] line profiles generally track one another, an additional use of the results in Table 1 is to compare line widths for [CII] and [NeII] lines to find anomalous sources that are broad in one line but not the other. For example, are there sources where [CII] arises in regions where [NeII] is not seen, either because of too much extinction or because there is a diffuse [CII] not associated with starbursts? Or, are there sources in which even the low ionization [NeII] is dominated by the AGN? This comparison is shown in Figure 4-7. This Figure is used to identify sources with unusually broad features, defined as having FWHMs that exceed the median values by 2σ. These sources are noted in Table 1 for further study in the future.

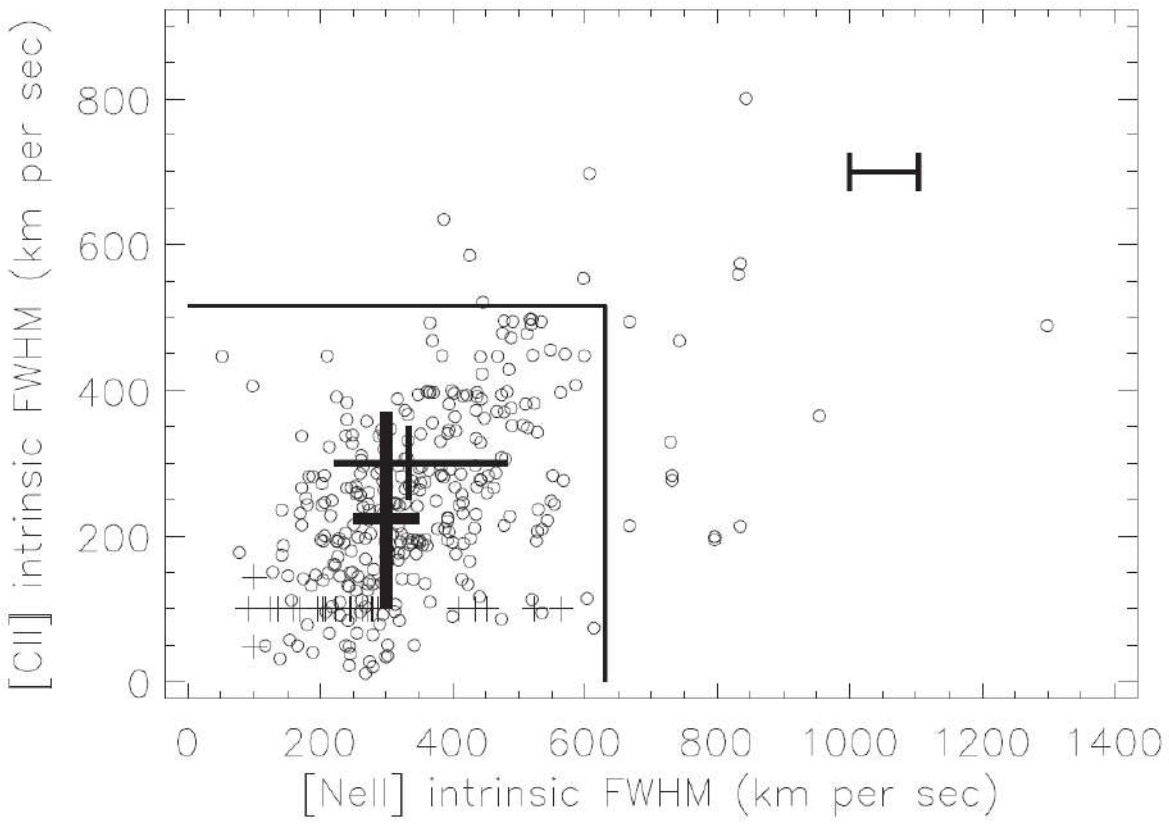

Figure 4-7. Intrinsic [CII] width compared to [Ne II] width in km s^{-1} from Table 1. Small crosses are sources in which the observed FWHM appears smaller than the instrumental resolution, so the FWHM is arbitrarily assumed as 100 km s^{-1}. The thick cross shows median (228 km s^{-1}) and 1σ dispersion for [CII], and then thin cross shows the median (333 km s^{-1}) and 1σ dispersion for [NeII] using the sources of all the AGN/starburst classifications. Sources outside of the box have FWHMs that exceed medians by 2σ. Observational uncertainty for [CII] FWHM is typically smaller than the size of symbols; uncertainties for each source are displayed in CASSIS. The error bar is the observational uncertainty of [NeII] FWHM, as in Figure 4-5.

A similar comparison is also made in Figure 4-8 between [CII] and [NeIII], although it would be less surprising in this case to find broad [NeIII] associated with an AGN. The few [CII] sources that equal or exceed the [NeIII] width are particularly interesting. Broad profiles seen in this comparison are also noted in Table 1.

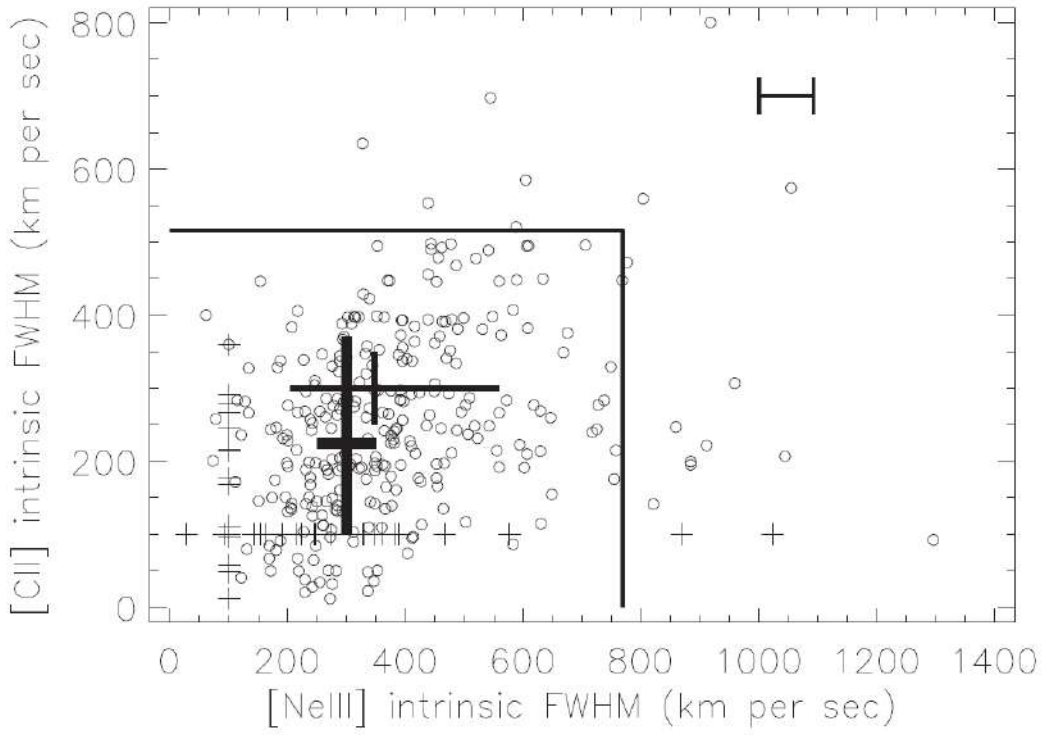

Figure 4-8. Intrinsic [CII] width compared to [NeIII] width in km s^{-1} from Table 1. Symbols and explanations are the same as in Figure 4-7, with the error bar showing the observational uncertainty of [NeIII] FWHM from Figure 4-6.

4.3.2. Comparisons of Radial Velocities

An alternative way to seek sources with significant differences between the physical locations of [CII] and neon emission is to compare the observed radial velocities measured in these different features. These comparisons are in Figures 4-9 and 4-10. The velocity differences dV between the profile centroids are given in Table 1, determined from the redshifts measured independently for the [CII] and neon lines and transformed to velocity units so that dV = c [z ([CII]) - z (Neon)] . Comparisons of dV are made to the [CII] FWHM to learn if broader lines have systematically more scatter in dV measures, although we see no indication of this. From these plots, sources with dV differing from the medians by more than 2σ are selected and noted in Table 1, because these sources may also prove

to be unusual. Dispersions in dV measures between [CII] and neon are ~±50 km s^{-1}, or ~10% of the observed median FWHM for the neon lines.

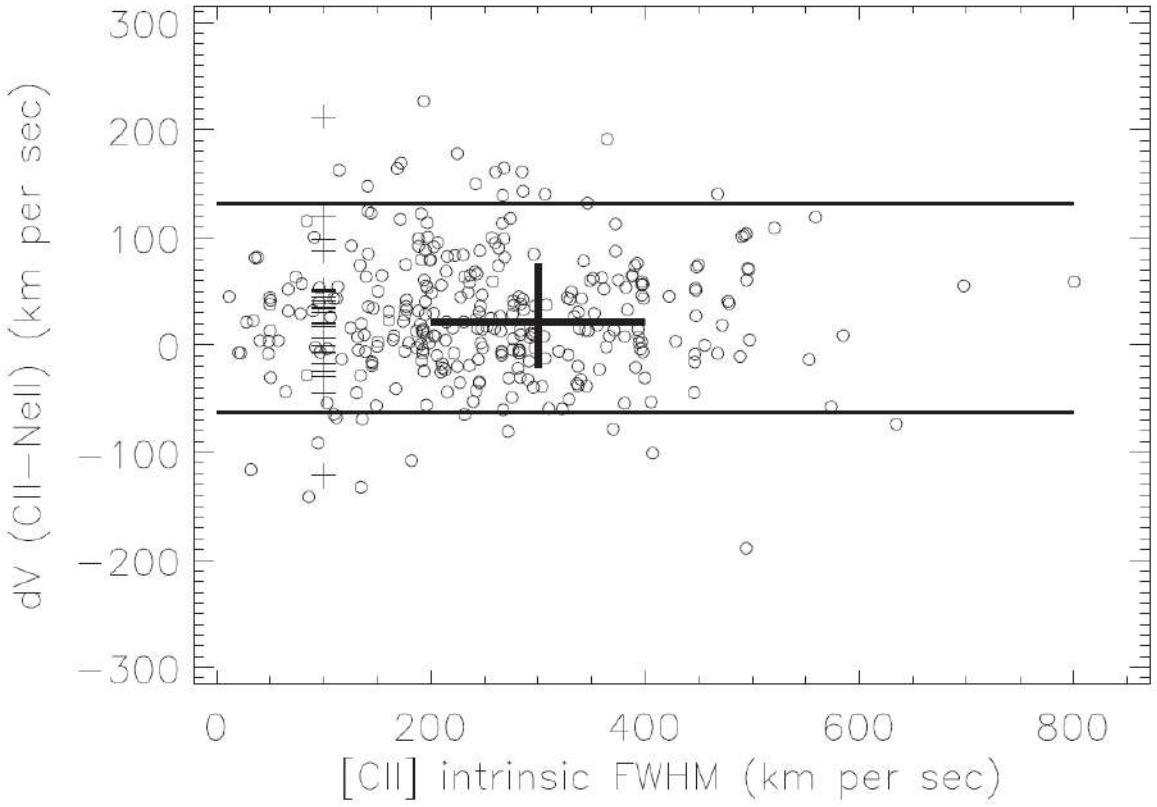

Figure 4-9. Difference dV between [CII] radial velocity and [NeII] radial velocity in km s^{-1} compared to [CII] line width. The large cross shows median (horizontal line) and 1σ dispersion about the median (vertical line) of radial velocity differences. Small crosses are sources in which the observed [CII] FWHM appears smaller than the instrumental resolution, so FWHM is arbitrarily assumed as 100 km s^{-1}. Sources outside of lines have dV that exceed the median by 2σ.

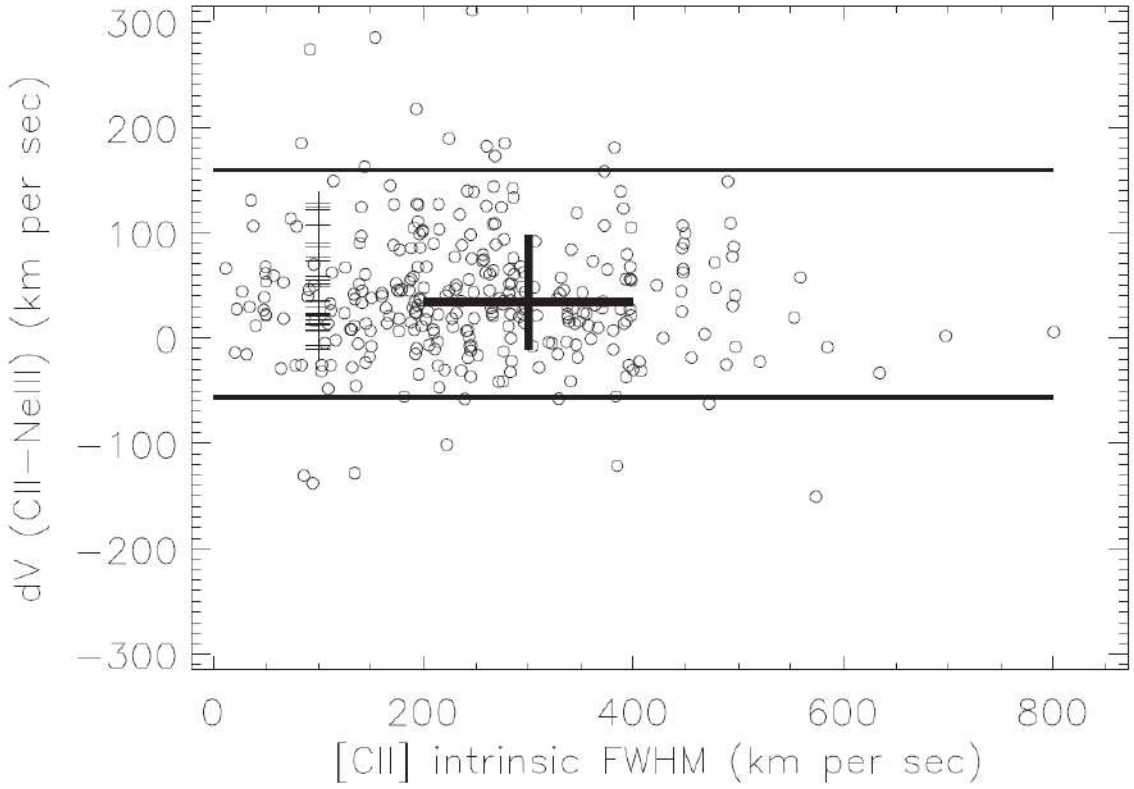

Figure 4-10. Difference dV in the [CII] radial velocity compared to the [NeIII] radial velocity in km s^{-1}. The symbols are the same same as in Figure 4-9.

In both Figures 4-9 and 4-10, there is little difference in the median radial velocities determined from PACS [CII] or IRS neon. For dV ([CII] - [NeII]), the median difference is 21 km s^{-1} and is 34 km s^{-1} for dV ([CII] - [NeIII]). These small systematic differences are a confirmation of the careful wavelength calibrations that were done independently for both instruments. There is a known instrumental effect in PACS that can lead to a skewed profile and offset in velocity. This effect arises when an unresolved source is not perfectly centered in a spaxel 7 and can produce velocity offsets up to ~±30 km s^{-1} for [CII]. This is less than the offsets that we note as unusually large, and offsets caused by this instrumental effect would be recognized as having a skewed profile.

4.4. Summary and Conclusions

We measure emission line profiles and redshifts for extragalactic sources observed in both [CII] 158 μm with Herschel PACS and in [NeII] 12.81 μm and [NeIII] 15.55 μm with the high-resolution Spitzer IRS. Data are presented and compared for 379 different sources. Results for [CII] and neon are compared by locating the PACS observing spaxel that most closely corresponds to the position of the IRS slit. Intrinsic line profile widths are determined by applying empirically measured instrumental widths from observed planetary nebulae or HII regions. All [CII] and neon line profiles, together with overlays of PACS spaxels compared to IRS slits, are illustrated in the CASSIS spectral atlas *(http://cassis.sirtf.com/herschel)*.

Sources are classified as AGNs, composites, or starbursts based on the equivalent width of the PAH 6.2 μm feature. The median intrinsic FWHM for [CII] shows no change with classification, being 207 km s^{-1} for AGNs, 248 km s^{-1} for composites, and 233 km s^{-1} for starbursts with dispersions in intrinsic line widths of about ±130 km s^{-1}. Results show that [CII] line widths generally match those of [NeII], as previously indicated in comparisons of line fluxes. A small number of sources are identified with unusually broad lines or with radial velocity differences between [CII] and neon measures. Accurate redshifts are determined for sources as demonstrated by a systematic difference of only 21 km s^{-1} between the independent measures of [CII] and [NeII] radial velocities using PACS and IRS.

5. ANALYSIS OF EMISSION LINE WIDTHS OF [CII] 158 μm

A study of [CII] 158 μm emission line profiles observed with Herschel PACS for 379 galaxies is presented. Emission line widths are compared to [CII] luminosities, to near-infrared 1.6 μm luminosities and to infrared 22 μm luminosities to decide if any luminosity relates to velocity dispersion. Archival data for [CII] fluxes and line profiles are taken from *http://cassis.sirtf.com/herschel/*. Line profiles are classified as Gaussian, flattened and asymmetric. H magnitudes are taken from 2MASS catalogues, and 22 μm fluxes from the WISE catalogue. These luminosities are compared to [CII] line Full Width Half Maximum. Asymmetric profiles are not primarily AGN, which indicates that asymmetries are not produced primarily by outflows from the nuclear region. [CII] line widths do not show a significant correlation with any measure of galaxy luminosity. The correlation having smallest dispersion is with the H band luminosity for which $L(H) \sim FWHM^{0.73}$, which is a much flatter correlation than the $L \sim FWHM^4$ previously found for optical emission lines or stellar velocity dispersions.

5.1. Introduction

Investigation of early galaxies is crucial for understanding galaxy formation and evolution. A particularly important new capability is the study of the far infrared [CII] 158 μm emission line. Especially in dusty, obscured sources it may be the only line observable with currently available techniques.

This [CII] line is the strongest far-infrared line in most sources [130, 131, 41, 42, 17] and is associated with star formation because it arises within the photodissociation region (PDR) surrounding starbursts [51, 52, 53, 54]. Numerous observations of the [CII] line have been made [75, 110, 109, 106, 116] using the Photodetector Array Camera and Spectrometer (PACS) instrument [73] on the Herschel Space Observatory [72]. The [CII] line profiles are often of very high quality, with velocity resolution < 250 km s^{-1}, so the line profiles themselves potentially contain diagnostic information.

In previous papers [64, 106], we compared the [CII] line with mid-infrared emission lines and with the Polycyclic Aromatic Hydrocarbon (PAH) feature observed with the Infrared Spectrograph (IRS; [30]) on the Spitzer Space Telescope [55]. These comparisons led to our calibration of the star formation rate (SFR) based on [CII] luminosities such that log SFR = log L([CII]) - 7.0 for SFR in solar masses/year and L([CII]) in solar luminosities. For those sources also observed at high resolution with the IRS, we compared line widths for various emission lines and confirmed the association of [CII] with the starburst component of 379 sources [121]. The [CII] line profiles were published in [121]. In this paper our primary new results are a classification of the line profiles based on shape, and comparisons of the line widths with various other properties of the galaxies to search for astrophysical mechanisms that control the line widths.

5.2. Sample Selection and Data

For the analysis in this chapter, the [CII] profiles shown in [121] are used. These profiles arise from the 8" x 8" spaxel of the PACS observation which is most closely aligned with the position of the Spitzer IRS observations used for comparisons in [121]. The full data used for the analysis in section 5.3 is available in VizieR Online Data Catalog. The table lists all sources with the same numbering and naming conventions, coordinates, observation numbers, and other ancillary data as in [121].

The [CII] results in Table 1 of the paper [132] are some of the profile classifications with examples in Figure 5-1, the full list of the FWHM of the profile from the Gaussian fits illustrated in *http://cassis.sirtf.com/herschel/* (profiles and profile data are in the EPS column under "Line Profile"), and the luminosities of the [CII] line derived from the fluxes shown in the profiles. The FWHM-s listed are intrinsic widths, after correcting for instrumental resolution of 236 km s^{-1}. The FWHM errors are also given in the webpage, the errors are so small, that they can be neglected. Archival data for H band fluxes and luminosities from the Two Micron All Sky Survey (2MASS; [133]) and for 22 μm fluxes

and luminosities from the Wide-Field Infrared Survey Explorer (WISE; [134]) are also given.

For use in the [132] paper, I have classified all of the [CII] profiles by shape, as compared to the best fitted Gaussian profiles illustrated in [121]. The objective of this classification is to distinguish among profiles obviously affected by disk rotation and those profiles which probably arise because of virialized three dimensional motions of the gas. Flattened profiles are those which have the clearest evidence of velocities dominated by rotation. Asymmetric profiles show evidence either of systematic gas outflows, or of rotation by an inhomogeneous disk.

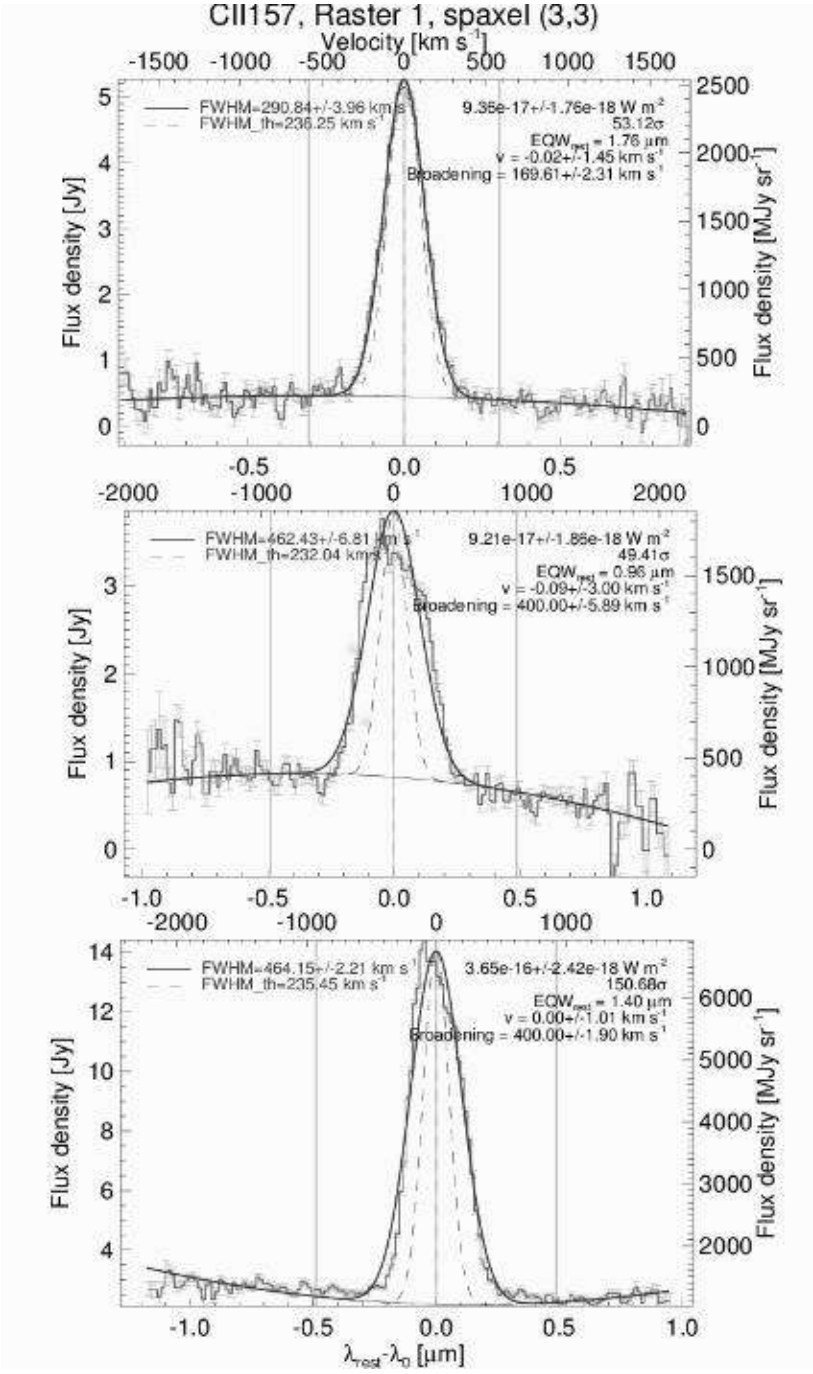

Figure 5-1. Examples of profile classifications as Gaussian (top, NGC3393), flattened (center, NGC7603), and asymmetric (bottom, ESO323-G077). All profiles used are shown in http://cassis.sirtf.com/herschel/.

5.3. Analysis and Discussion

The objective of this study is to search for what physical characteristic of the galaxies is primarily responsible for determining the observed [CII] profile widths. Much of the analysis in [121] was designed to compare the [CII] line to mid-infrared forbidden lines observed with the Spitzer IRS, with the goal of seeking differences between AGN and starburst sources. As described and reviewed in that paper, the mid-infrared AGN/starburst classification is made using the strength relative to continuum (equivalent width - EW) of the 6.2 μm PAH emission feature. In Figure 5-2, the [CII] line widths are seen to be independent of this classification, as also shown in [121].

The new result in Figure 5-2 is including the classification of profile shapes. One notable conclusion is that the asymmetric and flattened profiles are generally broader. This indicates that profiles with evidence of rotation generally show higher velocities. This is expected from dynamics of disk rotation compared to three-dimensional velocity dispersions arising within a galactic bulge, as pointed out for example by Nelson & Whittle [129]. The rotational velocity of the disk represents the potential of the disk and halo, yielding V max expected to be about 1.5 times the dispersion within the bulge. That flattened profiles are broader is evidence that the classification of profiles has a meaningful physical interpretation and leads to the comparisons below that use only Gaussian profiles for considering which galactic properties might control these velocity dispersions. Another important conclusion from Figure 5-2 is that the asymmetric profiles are not primarily AGN, which implies the asymmetries are not produced primarily by outflows from the nuclear region.

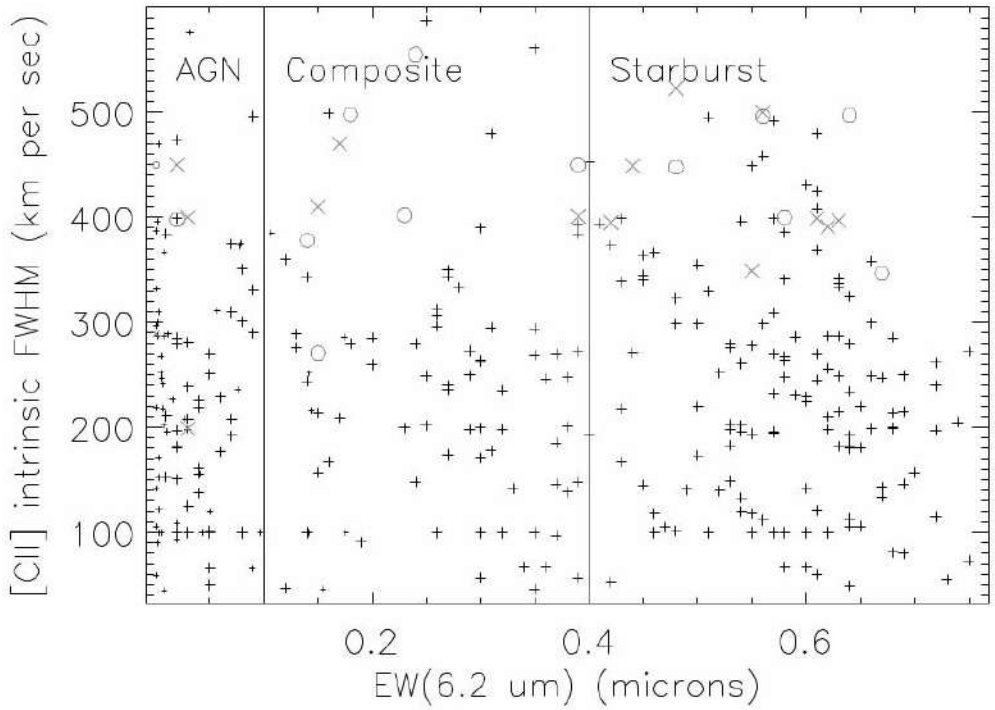

Figure 5-2. Profile FWHM compared to AGN/Starburst classification showing Gaussian profiles (+), asymmetric profiles (X) and flattened profiles (O). Horizontal axis shows the classification of sources using the 6.2 μm PAH feature; AGN have EW (6.2 μm) < 0.1 μm, Composite (AGN plus starburst) have 0.1 μm < W (6.2 μm) < 0.4 μm, and starbursts have EW (6.2 μm) > 0.4 μm.

Figure 5-3 shows the comparison of luminosities to sizes. The luminosities of the [CII] sources in Table 1 of the paper [132] for a single PACS spaxel. Transforming the 8" spaxel to a physical size gives the values in Table 1, which are plotted in Figure 5-3. The [CII] luminosities for the local sources level off for sizes > 8 kpc, indicating that most luminosity arises with this area. This is also an appropriate size to adopt for a galactic bulge, so the kinematical analysis below for the FWHM will be restricted to sources of size < 8 kpc. If more details are desired of galaxy morphologies, optical images of individual sources can be seen with overlays showing the PACS spaxels in the "footprint" column of *http://cas-sis.sirtf.com/herschel/*.

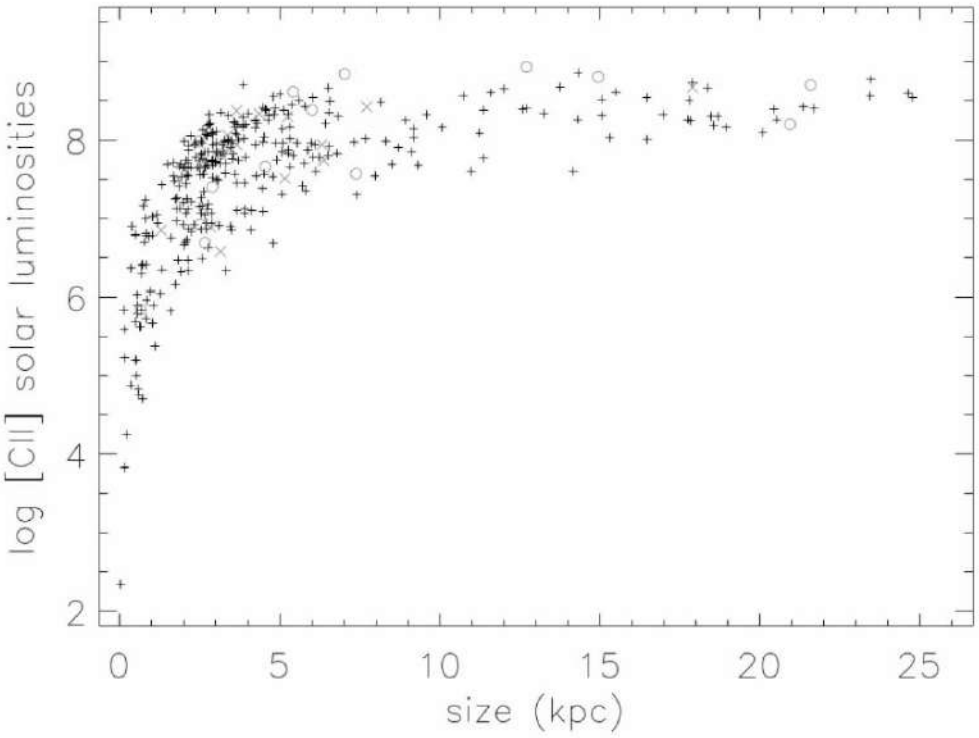

Figure 5-3. [CII] luminosities compared to observed size. Symbols are as in Figure 5-2.

The second objective of this paper is to compare [CII] FWHM to other galactic parameters in search of correlations. It has long been known that stellar velocity dispersions within galactic bulges relate to bulge luminosity with a form $L \propto \sigma n$ for the stellar line of sight velocity dispersion. This relates to the FWHM by FWHM 2.35σ, and FWHM is normally used as the measure of velocity dispersion when using optical emission lines [117, 135, 136]. The initial study [137] found that $3 < n < 4$. In a reevaluation of a large sample of galactic bulges, Whittle [135] found $n = 3.2$. When using the [OIII] optical emission line, primarily for Seyfert galaxies, he found n = 2.2. Subsequent studies by Nelson & Whittle [129] and Shields et al. [136] determined that even the [OIII] widths from the narrow line region of AGN are controlled primarily by bulge gravity rather than by other sources inputting kinetic energy to the gas. More recent studies of relations between velocity dispersions and bulge gravity emphasized the use of sigma to determine relations among the masses of central black holes, bulge velocity dispersions, and bulge luminosities. The comprehensive summary of Kormendy & Ho studies [138] yields n = 3.7, and that of McConnell & Ma [139] gives $n = 5.1$.

Based on this extensive previous work, it would be expected that any integrated measure of velocity dispersion for a galaxy should show a meaningful correlation with the mass of that galaxy. This is my motive for comparing the FWHM of the [CII] lines with three different measures of galaxy luminosity, each of which measures a different mass. The three parameters are: 1. the luminosity of the [CII] line itself, which scales primarily with the photodissociation regions surrounding starbursts and so scales with the gas mass connected to star formation; 2. The luminosity of dust reradiation, taken as 22 μm dust luminosity, which scales with the total luminosity of younger, hotter stars that are heating the dust; 3. The near infrared (H band) luminosity of the galaxy, which scales with the total luminosity of the evolved stars. Comparisons of [CII] FWHM with these three measures of luminosity are shown in Figure 5-4 and 5-5. These plots include only sources in Vizier Table with Gaussian profiles, and only objects with size < 8 kpc. This gives more confidence that the observed FWHM represent velocity dispersions that measure gravity from the halo regions of the galaxies.

Figure 5-4 illustrates the results using the conventional comparison of logL with log-FWHM. In all cases, the value of n is much smaller than previous studies using stellar velocity dispersions or optical emission lines. For [CII] luminosities, $n = 1.52 \pm 0.24$; for 22 μm luminosities, $n = 0.38 \pm 0.20$; for H luminosities, $n = 0.73 \pm 0.11$.

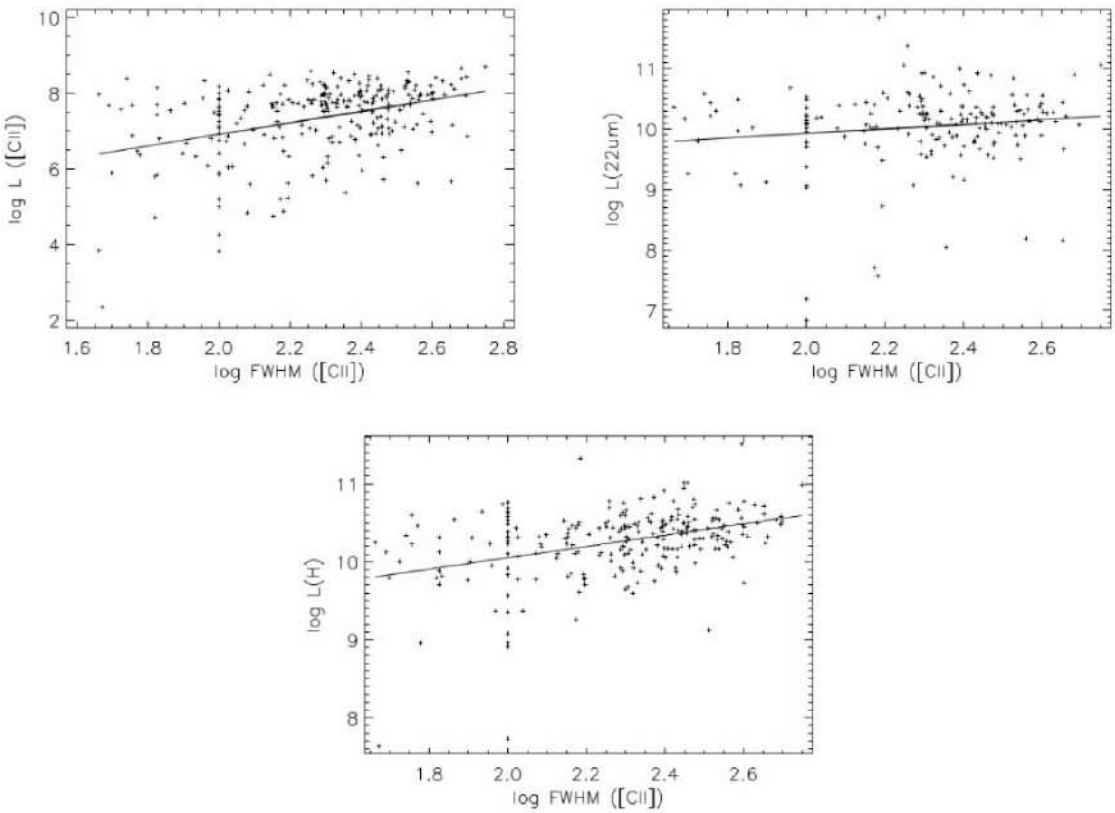

Figure 5-4. Luminosities in solar luminosities compared to [CII] FWHM in km s^{-1}. Top left figure shows [CII] luminosity and line fit is log L([CII]) = 1.52(±0.24)logFWHM+3.86. Top right figure shows 22 μm luminosity and line fit is log L(22 μm) = 0.38(±0.20)log FWHM+9.17. Lower figure shows H luminosity and line fit is log L(H) = 0.73(±0.11)log FWHM+8.60.

In Figure 5-5, the fits are shown using linear values for FWHM to compare scatter among the comparisons using the different parameters. These plots show the scatter in the luminosity distributions above and below the formal fits (+-1σ for logL) within three different ranges of FWHM. In all cases, the scatter is extreme. The range of luminosities at a given value of FWHM is comparable in all cases to the full range of FWHM over all luminosities. There can be a factor of 5 range in gas velocities for the same value of luminosity. It does not appear, therefore, that FWHM for [CII] can be used in a meaningful way to predict any kind of galaxy luminosity.

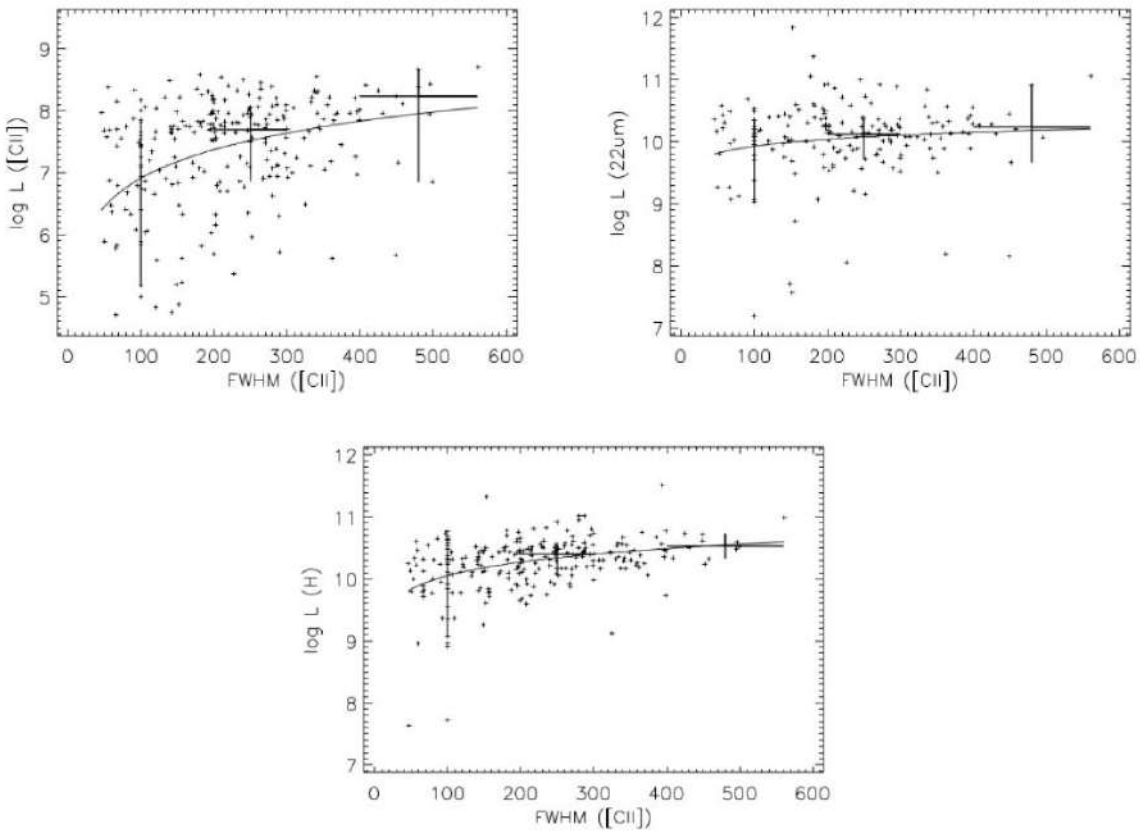

Figure 5-5. Luminosities compared to FWHM (linear scale). Fits are as in Figure 5-4. Vertical lines show 1σ dispersions for velocities 100 km s^{-1}, 200-300 km s^{-1} and > 400 km s^{-1}.

Despite the large scatters, the results do imply a meaningful conclusion. The luminosity dispersions are smallest for the H band luminosities, next for the dust luminosities, and largest for the [CII] luminosities. This scaling of luminosity dispersions also progresses the same as the uncertainties in the slopes of the line fits in Figure 5-4 (smallest uncertainty for H luminosity). In both cases, therefore, the correlation of FWHM with H band luminosity is better than with either other parameter. I conclude from this that the gravity associated with the mass of evolved stars is a factor controlling the widths of the [CII] line. Nevertheless, the large range in gas velocities that can be found at the same value of luminosity remains puzzling. It seems that some unidentified process other than straightforward gravitational forces within the galactic bulge is the primary controller of CII gas velocities.

5.4. Summary

I classify [CII] 158 μm profiles for 379 galaxies observed with Herschel PACS as Gaussian, flattened and asymmetric based on the comparison of observed profiles to Gaussian fits. Profile shapes can indicate the origin of the line widths because the lines whose width is caused by three dimensional random motions in a galaxy should be Gaussian, but widths caused by rotation of a disk should not be Gaussian. Emission line widths are compared to [CII] luminosities, to near-infrared 1.6 μm luminosities and to infrared 22 μm luminosities to decide if any luminosity accurately relates to velocity dispersion. The luminosity dispersions are smallest for H band luminosities and the slope uncertainty for the line fit is the smallest for H luminosities. I conclude from this that the gravity associated with the mass of evolved stars is a weak factor controlling the widths of the [CII] line, but line widths are primarily determined by a mechanism that is still unknown.

6. CONCLUSIONS

This comprehensive study used Herschel PACS observations of the [CII] 158 μm fine-structure line, combined with Spitzer IRS mid-infrared spectroscopy and IRAS fluxes, to investigate the properties of a large sample of galaxies spanning a broad range of star formation and active galactic nucleus (AGN) activity. The results firmly establish [CII] as a robust tracer of the star-forming (starburst) component in galaxies and provide valuable calibrations and insights into star formation rates, kinematics, and the interplay of AGNs and starbursts.

Across the sample, [CII] emission correlates strongly with mid-infrared polycyclic aromatic hydrocarbon (PAH) features, notably the 6.2 μm and 11.3 μm PAH lines, and with mid-infrared [NeII] line, which means that both [CII] and [NeII] represent the starburst component of the galaxy. The consistency of these relationships, independent of whether a source is dominated by star formation or an AGN, demonstrates that [CII] measures the starburst component as reliably as established mid-infrared tracers. The result is a firm calibration of star formation rates (SFRs) from [CII] luminosity:

$$\text{Log (SFR)} = \log (L\,[\text{CII}]) - 7.0 \pm 0.2,$$

where SFR is in $M_\odot\ yr^{-1}$ and L([CII]) in $L_\odot$. This relation applies not just to pure starburst galaxies but also to systems where AGNs are present, allowing isolation of the star-forming contribution even in composite sources.

While the [CII]/IR ratio generally declines at the highest infrared luminosities—known as the [CII] “deficit”, these findings clarify that this phenomenon arises primarily because luminous sources often have a substantial AGN component inflating their total infrared output. Consequently, the proportion of [CII] coming from star formation appears smaller against the AGN-driven IR continuum. When the starburst component is isolated, [CII] remains a faithful measure of the star formation activity.

The ratio of [CII] line flux to the continuum at 158 μm remains relatively constant across classifications, suggesting that the far-infrared continuum near 158 μm is also dominated by star-forming regions. For pure starbursts, the continuum alone at 158 μm provides a

secondary SFR indicator. However, in AGN-dominated systems, using only the far-infrared continuum to estimate SFR can lead to moderate overestimates (by a factor of about 1.4). This highlights the importance of line diagnostics like [CII] for accurate SFR estimates in complex systems.

High-resolution measurements of [CII] line profiles and comparisons with neon lines reveal that line widths and kinematics are broadly similar across AGN, composite, and starburst classifications. The median intrinsic [CII] line widths (~200–250 km s^{-1}) do not depend strongly on nuclear activity type. Moreover, [CII] and [NeII] lines yield consistent redshifts, demonstrating the utility of these far-infrared and mid-infrared lines as reliable probes of galaxy velocities and distances.

Analysis of [CII] line profiles show a range of shapes—Gaussian, flattened, or asymmetric—implying that not all linewidths are driven purely by random motions. While comparing line widths to various luminosities suggests that the gravitational potential traced by the mass of more evolved stars (as indicated by H-band luminosity) may modestly influence the observed kinematics, the dominant mechanism controlling [CII] line width remains unclear.

These results solidify the role of [CII] 158 μm emission as a key diagnostic of star formation in diverse galactic environments. They demonstrate that [CII] emission is an integral counterpart to mid-infrared emission line and PAH diagnostics, providing robust SFR measures and aiding in disentangling star formation from AGN effects. In addition, the kinematic analyses improve our understanding of the gas dynamics in galaxies, though further work is needed to pinpoint the main drivers of the observed velocity dispersions. In summary, [CII] emerges as a powerful, versatile tool for studying the star-forming properties and kinematics of galaxies, serving as a cornerstone for multi-wavelength analyses of galaxy evolution.

ACKNOWLEDGEMENTS

First and foremost, I would like to express my deepest gratitude to my colleague, Prof. Daniel W. Weedman, for providing me with a pivotal opportunity in my scientific career. Working on a highly significant topic in astrophysics alongside some of the best scientists in the field—James Houck, Don Barry, and Lusine Sargsyan—was an honor. My research missions to Cornell University remain some of the most memorable and productive experiences of my life. Prof. Weedman's encouragement to excel in the field and present my work at international conferences, workshops, and summer schools was invaluable.

I also wish to extend my gratitude to my PhD supervisor, Dr. Ararat Yeghikyan, and to Dr. Elena Nikoghosyan for their unwavering guidance and encouragement during the completion of my thesis. Their expertise and support were instrumental in navigating the challenges of my academic journey.

I am deeply grateful to my colleague Dr. Naira Azatyan for being a motivation for me in the Byurakan Astrophysical Observatory.

I would like to thank the Higher Education and Science Committee of the RA Ministry of Education, Science, Culture and Sports for supporting scientists in Armenia. Their efforts to improve opportunities are appreciated, and I believe that quality education and competitive science are key to having a developed country.

To my husband, Ashot Kosakyan, thank you for your unwavering support and for standing by my side through all the milestones of my life.

Finally, I want to thank my colleagues at the Byurakan Astrophysical Observatory. The collaborative scientific environment and knowledge I have gained here have been crucial to my growth as a researcher.

REFERENCES

[1] D. Lutz, H. W. W. Spoon, D. Rigopoulou, A. F. M. Moorwood and R. Genzel, "The Nature and Evolution of Ultraluminous Infrared Galaxies," *Astrophysical Journal,* pp. L103-l107, 1998.

[2] V. A. Ambartsumian, "On the Activity of Galctic Nuclei (introductory lecture)," in *proceedings of IAU Symposium No. 29*, Byurakan, 1968.

[3] V. A. Ambartsumian, "On nuclei of galaxies and their activity," in *Problems of gravitation*, Izdatel'stvo Erevanskogo Universiteta, 1975, pp. 5-17.

[4] V. A. Ambartsumian, "Galaxies and their nuclei," *Highlights of Astronomy,* vol. 3, pp. 51-66, 1974.

[5] R. Antonucci, "Unified models for active galactic nuclei and quasars," *Annual Review of Astronomy and Astrophysics,* vol. 31, pp. 473-521, 1993.

[6] H. Netzer, "Revisiting the Unified Model of Active Galactic Nuclei," *Annual Review of Astronomy and Astrophysics,* vol. 53, pp. 365-408, 2015.

[7] J. H. Krolik, Active galactic nuclei : from the central black hole to the galactic environment, Princeton University Press, 1999.

[8] C. M. Urry and P. Padovani, "Unified Schemes for Radio-Loud Active Galactic Nuclei," *Publications of the Astronomical Society of the Pacific,* vol. 107, p. 803, 1995.

[9] B. M. Peterson, An Introduction to Active Galactic Nuclei, New York: Cambridge University Press, 1997.

[10] R. C. J. Kennicutt, "Star Formation in Galaxies Along the Hubble Sequence," *Annual Review of Astronomy and Astrophysics,* vol. 36, pp. 189-232, 1998.

[11] D. Calzetti, L. Armus, R. C. Bohlin, A. L. Kinney, J. Koornneef and T. Storchi-Bergmann, "The Dust Content and Opacity of Actively Star-forming Galaxies," *The Astrophysical Journal,* vol. 533, no. 2, pp. 682-695, 2000.

[12] R. Genzel and C. J. Cesarsky, "Extragalactic Results from the Infrared Space Observatory," *Annual Review of Astronomy and Astrophysics,* vol. 38, pp. 761-814, 2000.

[13] J. D. T. Smith, B. T. Draine, D. A. Dale, J. Moustakas, R. C. J. Kennicutt, G. Helou, L. Armus, H. Roussel, K. Sheth, G. J. Bendo, B. A. Buckalew, D. Calzetti and Engel, "The Mid-Infrared Spectrum of Star-forming Galaxies: Global Properties of Polycyclic Aromatic Hydrocarbon Emission," *The Astrophysical Journal,* vol. 656, no. 2, pp. 770-791, 2007.

[14] S. Veilleux and D. E. Osterbrock, "Spectral Classification of Emission-Line Galaxies," *Astrophysical Journal Supplement,* vol. 63, p. 295, 1987.

[15] N. Indriolo and B. J. McCall, "Investigating the Cosmic-Ray Ionization Rate in the Galactic Diffuse Interstellar Medium through Observations of H3+," *The Astrophysical Journal,* vol. 745, no. 1, p. 91/17, 2012.

[16] T. Oka, "Interstellar Chemistry Special Feature: Interstellar H3+," in *Proceedings of the National Academy of Science*, 2006.

[17] G. J. Stacey, N. Geis, R. Genzel, J. B. Lugten, A. Poglitsch, A. Sternberg and C. H. Townes, "The 158 Micron [C II] Line: A Measure of Global Star Formation Activity in Galaxies," *Astrophysical Journal,* vol. 373, p. 423, 1991.

[18] I. De Looze, M. Baes, G. J. Bendo, L. Cortese and J. Fritz, "The reliability of [C II] as an indicator of the star formation rate," *Monthly Notices of the Royal Astronomical Society,* vol. 416, no. 4, pp. 2712-2724, 2011.

[19] D. Weedman, M. Polletta, C. J. Lonsdale, B. J. Wilkes, B. Siana, J. R. Houck, J. Surace, D. Shupe, D. Farrah and H. E. Smith, "Active Galactic Nucleus and Starburst Classification from Spitzer Mid-Infrared Spectra for High-Redshift SWIRE Sources," *The Astrophysical Journal,* vol. 653, no. 1, pp. 101-111, 2006.

[20] I. De Looze, D. Cormier, V. Lebouteiller, S. Madden, M. Baes, G. J. Bendo, M. Boquien, A. Boselli, D. L. Clements, L. Cortese and ..., "The applicability of far-infrared fine-structure lines as star formation rate tracers over wide ranges of metallicities and galaxy types," *Astronomy & Astrophysics,* vol. 568, p. A62/34, 2014.

[21] J. Graciá-Carpio, E. Sturm, S. Hailey-Dunsheath, J. Fischer, A. Contursi, A. Poglitsch, R. Genzel, E. González-Alfonso, A. Sternberg, A. Verma, N. Christopher, R. Davies, H. Feuchtgruber and ..., "Far-infrared Line Deficits in Galaxies with Extreme L_FIR/M_H2 Ratios," *The Astrophysical Journal Letters,* vol. 728, no. 1, p. L7/5, 2011.

[22] C. L. Carilli and F. Walter, "Cool Gas in High-Redshift Galaxies," *Annual Review of Astronomy and Astrophysics,* vol. 51, no. 1, pp. 105-161, 2013.

[23] R. Maiolino, S. Carniani, A. Fontana, L. Vallini, L. Pentericci, A. Ferrara, E. Vanzella, A. Grazian, S. Gallerani, M. Castellano and ..., "The assembly of 'normal' galaxies at z

~ 7 probed by ALMA," *Monthly Notices of the Royal Astronomical Society,* vol. 452, no. 1, pp. 54-68, 2015.

[24] B. T. Soifer, G. Neugebauer and J. R. Houck, "The IRAS view of the extragalactic sky," *Annual Rev. Astron. Astrophys.,* vol. 25, pp. 187-230, 1987.

[25] D. B. Sanders and I. F. Mirabel, "Luminous Infrared Galaxies," *Annual Review of Astronomy and Astrophysics,* vol. 34, p. 749, 1996.

[26] R. Chary and D. Elbaz, "Interpreting the Cosmic Infrared Background: Constraints on the Evolution of the Dust-enshrouded Star Formation Rate," *The Astrophysical Journal,* vol. 556, no. 2, pp. 562-581, 2001.

[27] G. Lagache, H. Dole, J. -L. Puget, P. G. Pérez-González, E. Le Floc'h, G. H. Rieke, C. Papovich, E. Egami, A. Alonso-Herrero, C. W. Engelbracht, K. D. Gordon, K. A. Misselt and J. E. Morrison, "Polycyclic Aromatic Hydrocarbon Contribution to the Infrared Output Energy of the Universe at z ~= 2," *The Astrophysical Journal Supplement Series,* vol. 154, no. 1, pp. 112-117, 2004.

[28] E. Le Floc'h, C. Papovich, H. Dole, E. F. s. b. o. Bell, G. Lagache, G. H. Rieke, E. Egami, P. G. Pérez-González, A. Alonso-Herrero, M. J. Rieke, M. Blaylock and ..., "Infrared Luminosity Functions from the Chandra Deep Field-South: The Spitzer View on the History of Dusty Star Formation at 0 <~ z <~ 1," *The Astrophysical Journal,* vol. 632, no. 1, pp. 169-190, 2005.

[29] S. C. Chapman, A. W. Blain, I. Smail and R. J. Ivison, "A Redshift Survey of the Submillimeter Galaxy Population," *The Astrophysical Journal,* vol. 622, no. 2, pp. 772-796, 2005.

[30] J. R. Houck, T. L. Roellig, J. van Cleve, W. J. Forrest, T. Herter, C. R. Lawrence, K. Matthews, H. J. Reitsema, B. T. Soifer, D. M. Watson, D. Weedman, M. Huisjen, J. Troeltzsch, D. J. Barry and ..., "The Infrared Spectrograph (IRS) on the Spitzer Space Telescope," *The Astrophysical Journal Supplement Series,* vol. 154, no. 1, pp. 18-24, 2004.

[31] J. R. Houck, B. T. Soifer, D. Weedman, S. J. U. Higdon, J. L. Higdon, T. Herter, M. J. I. Brown, A. Dey, B. T. Jannuzi, E. Le Floc'h, M. Rieke, L. Armus and ..., "Spectroscopic Redshifts to z > 2 for Optically Obscured Sources Discovered with the Spitzer Space Telescope," *The Astrophysical Journal,* vol. 622, no. 2, pp. L105-L108, 2005.

[32] L. Yan, A. Sajina, D. Fadda, P. Choi, L. Armus, G. Helou, H. Teplitz, D. Frayer and J. Surace, "Spitzer Mid-Infrared Spectroscopy of Infrared Luminous Galaxies at z ~ 2. I. The Spectra," *The Astrophysical Journal,* vol. 658, no. 2, pp. 778-793, 2007.

[33] A. Sajina, L. Yan, L. Armus, P. Choi, D. Fadda, G. Helou and H. Spoon, "Spitzer Mid-Infrared Spectroscopy of Infrared Luminous Galaxies at z~2. II. Diagnostics," *The Astrophysical Journal,* vol. 664, no. 2, pp. 713-737, 2007.

[34] D. W. Weedman and J. R. Houck, "Evolution of the Most Luminous Dusty Galaxies," *The Astrophysical Journal,* vol. 698, no. 2, pp. 1682-1697, 2009.

[35] A. Dey, B. T. Soifer, V. Desai, K. Brand, E. Le Floc'h, M. J. I. Brown, B. T. Jannuzi, L. Armus, S. Bussmann, M. Brodwin, C. Bian, P. Eisenhardt, S. J. Higdon, D. Weedman and S. P. Willner, "A Significant Population of Very Luminous Dust-Obscured Galaxies at Redshift z ~ 2," *The Astrophysical Journal,* vol. 677, no. 2, pp. 943-956, 2008.

[36] D. M. Alexander, F. E. Bauer, S. C. Chapman, I. Smail, A. W. Blain, W. N. Brandt and R. J. Ivison, "The X-Ray Spectral Properties of SCUBA Galaxies," *The Astrophysical Journal,* vol. 632, no. 2, pp. 736-750, 2005.

[37] A. Pope, R.-R. Chary, D. M. Alexander, L. Armus, M. Dickinson, D. Elbaz, D. Frayer, D. Scott and H. Teplitz, "Mid-Infrared Spectral Diagnosis of Submillimeter Galaxies," *The Astrophysical Journal,* vol. 675, no. 2, pp. 1171-1193, 2008.

[38] K. Menéndez-Delmestre, A. W. Blain, I. Smail, D. M. Alexander, S. C. Chapman, L. Armus, D. Frayer, R. J. Ivison and H. Teplitz, "Mid-Infrared Spectroscopy of Submillimeter Galaxies: Extended Star Formation in Massive High-redshift Galaxies," *The Astrophysical Journal,* vol. 699, no. 1, pp. 667-685, 2009.

[39] K. Coppin, A. Pope, K. Menéndez-Delmestre, D. M. Alexander, J. S. Dunlop, E. Egami, J. Gabor, E. Ibar, R. J. Ivison, J. E. Austermann, A. W. Blain, S. C. Chapman and ..., "Mid-infrared Spectroscopy of Candidate Active Galactic Nuclei-dominated Submillimeter Galaxies," *The Astrophysical Journal,* vol. 713, no. 1, pp. 503-519, 2010.

[40] A. Kovács, A. Omont, A. Beelen, C. Lonsdale, M. Polletta, N. Fiolet, T. R. Greve, C. Borys, P. Cox, C. De Breuck, H. Dole, C. D. Dowell, D. Farrah and ..., "Far-infrared Properties of Spitzer-selected Luminous Starbursts," *The Astrophysical Journal,* vol. 717, no. 1, pp. 29-39, 2010.

[41] M. L. Luhman, S. Satyapal, J. Fischer, M. G. Wolfire, E. Sturm, C. C. Dudley, D. Lutz and R. Genzel, "The [C II] 158 Micron Line Deficit in Ultraluminous Infrared Galaxies Revisited," *The Astrophysical Journal,* vol. 594, no. 2, pp. 758-775, 2003.

[42] J. R. Brauher, D. A. Dale and G. Helou, "A Compendium of Far-Infrared Line and Continuum Emission for 227 Galaxies Observed by the Infrared Space Observatory," *The Astrophysical Journal Supplement Series,* vol. 178, no. 2, pp. 280-301, 2008.

[43] E. Bañados, R. Decarli, F. Walter, B. P. Venemans, E. P. Farina and X. Fan, "Bright [C II] 158 μm Emission in a Quasar Host Galaxy at z = 6.54," *The Astrophysical Journal Letters,* vol. 805, no. 1, p. L8, 2015.

[44] M. T. Huynh, R. P. Norris, K. E. K. Coppin, B. H. C. Emonts, R. J. Ivison, N. Seymour, I. Smail, V. Smolcic, A. M. Swinbank, W. N. Brandt and ..., "Physical conditions of the gas in an ALMA [C ii]-identified submillimetre galaxy at z = 4.44.," *Mon. Not. R. Astron. Soc.,* vol. 431, pp. L88-L92, 2013.

[45] R. Wang, J. Wagg, C. L. Carilli, F. Walter, L. Lentati, X. Fan, D. A. Riechers, F. Bertoldi, D. Narayanan, M. A. Strauss, P. Cox and A. Omont, "Star Formation and Gas Kinematics of Quasar Host Galaxies at z ~ 6: New Insights from ALMA," *The Astrophysical Journal,* vol. 773, no. 1, p. 44, 2013.

[46] R. Maiolino, P. Cox, P. Caselli, A. Beelen, F. Bertoldi, C. L. Carilli, M. J. Kaufman, K. M. Menten, T. Nagao, A. Omont, A. Weiß, C. M. Walmsley, F. Walter and ..., "First detection of [CII]158 μm at high redshift: vigorous star formation in the early universe," *Astronomy and Astrophysics,* vol. 440, no. 2, pp. L51-L54, 2005.

[47] B. P. Venemans, R. G. McMahon, F. Walter, R. Decarli, P. Cox, R. Neri, P. Hewett, D. J. Mortlock, C. Simpson and S. J. Warren, "Detection of Atomic Carbon [C II] 158 μm and Dust Emission from a z = 7.1 Quasar Host Galaxy," *The Astrophysical Journal Letters,* vol. 751, no. 2, p. L25, 2012.

[48] S. Hailey-Dunsheath, T. Nikola, G. J. Stacey, T. E. Oberst, S. C. Parshley, D. J. Benford, J. G. Staguhn and C. E. Tucker, "Detection of the 158 μm [C II] Transition at z = 1.3: Evidence for a Galaxy-wide Starburst," *The Astrophysical Journal Letters,* vol. 714, no. 1, pp. L162-L166, 2010.

[49] G. J. Stacey, S. Hailey-Dunsheath, C. Ferkinhoff, T. Nikola, S. C. Parshley, D. J. Benford, J. G. Staguhn and N. Fiolet, "A 158 μm [C II] Line Survey of Galaxies at z ~ 1-2: An Indicator of Star Formation in the Early Universe," *The Astrophysical Journal,* vol. 724, no. 2, pp. 957-974, 2010.

[50] R. J. Ivison, A. M. Swinbank, B. Swinyard, I. Smail, C. P. Pearson, D. Rigopoulou, E. Polehampton, J. -P. Baluteau, M. J. Barlow, A. W. s. b. o. Blain, J. Bock, C and ..., "Herschel and SCUBA-2 imaging and spectroscopy of a bright, lensed submillimetre galaxy at z = 2.3," *Astronomy and Astrophysics,* vol. 518, p. L35, 2010.

[51] A. G. G. M. Tielens and D. Hollenbach, "Photodissociation regions. I. Basic model.," *Astrophysical Journal,* vol. 291, pp. 722-746, 1985.

[52] G. Helou, S. Malhotra, D. J. Hollenbach, D. A. Dale and A. Contursi, "Evidence for the Heating of Atomic Interstellar Gas by Polycyclic Aromatic Hydrocarbons," *The Astrophysical Journal,* vol. 548, no. 1, pp. L73-L76, 2001.

[53] S. Malhotra, M. J. Kaufman, D. Hollenbach, G. Helou, R. H. Rubin, J. Brauher, D. Dale, N. Y. Lu, S. Lord, G. Stacey, A. Contursi, D. A. Hunter and H. Dinerstein, "Far-Infrared Spectroscopy of Normal Galaxies: Physical Conditions in the Interstellar Medium," *The Astrophysical Journal,* vol. 561, no. 2, pp. 766-786, 2001.

[54] R. Meijerink, M. Spaans and F. P. Israel, "Diagnostics of irradiated dense gas in galaxy nuclei. II. A grid of XDR and PDR models," *Astronomy and Astrophysics,* vol. 461, no. 3, pp. 793-811, 2007.

[55] M. W. Werner, T. L. Roellig, F. J. Low, G. H. Rieke, M. Rieke, W. F. Hoffmann, E. Young, J. R. Houck, B. Brandl, G. G. Fazio, J. L. Hora, R. D. Gehrz, G. Helou, B. T. Soifer, J. Stauffer, Keene and ..., "The Spitzer Space Telescope Mission," *The Astrophysical Journal Supplement Series,* vol. 154, no. 1, pp. 1-9, 2004.

[56] B. R. Brandl, J. Bernard-Salas, H. W. W. Spoon, D. Devost, G. C. Sloan, S. Guilles, Y. Wu, J. R. Houck, D. W. Weedman, L. Armus, P. N. Appleton, B. T. Soifer, V. Charmandaris and ..., "The Mid-Infrared Properties of Starburst Galaxies from Spitzer-IRS Spectroscopy," *The Astrophysical Journal,* vol. 653, no. 2, pp. 1129-1144, 2006.

[57] V. Desai, L. Armus, H. W. W. Spoon, V. Charmandaris, J. Bernard-Salas, B. R. Brandl, D. Farrah, B. T. Soifer, H. I. Teplitz, P. M. Ogle and ..., "PAH Emission from Ultraluminous Infrared Galaxies," *The Astrophysical Journal,* vol. 669, no. 2, pp. 810-820, 2007.

[58] D. Farrah, J. Bernard-Salas, H. W. W. Spoon, B. T. Soifer, L. Armus, B. Brandl, V. Charmandaris, V. Desai, S. Higdon, D. Devost and J. Houck, "High-Resolution Mid-Infrared Spectroscopy of Ultraluminous Infrared Galaxies," *The Astrophysical Journal,* vol. 667, no. 1, pp. 149-169, 2007.

[59] J. Bernard-Salas, H. W. W. Spoon, V. Charmandaris, V. Lebouteiller, D. Farrah, D. Devost, B. R. Brandl, Y. Wu, L. Armus, L. Hao, G. C. Sloan, D. Weedman and J. R. Houck, "A Spitzer High-resolution Mid-Infrared Spectral Atlas of Starburst Galaxies," *The Astrophysical Journal Supplement,* vol. 184, no. 2, pp. 230-247, 2009.

[60] S. Veilleux, D. S. N. Rupke, D. -C. Kim, R. Genzel, E. Sturm, D. Lutz, A. Contursi, M. Schweitzer, L. J. Tacconi, H. Netzer, A. Sternberg, J. C. Mihos, A. J. Baker, J. M. Mazzarella and ..., "Spitzer Quasar and Ulirg Evolution Study (QUEST). IV.

Comparison of 1 Jy Ultraluminous Infrared Galaxies with Palomar-Green Quasars," *The Astrophysical Journal Supplement,* vol. 182, no. 2, pp. 628-666, 2009.

[61] D. W. Weedman and J. R. Houck, "Average Infrared Galaxy Spectra from Spitzer Flux-Limited Samples," *The Astrophysical Journal,* vol. 693, no. 1, pp. 370-382, 2009.

[62] S. Tommasin, L. Spinoglio, M. A. Malkan and G. Fazio, "Spitzer-IRS High-Resolution Spectroscopy of the 12 μm Seyfert Galaxies. II. Results for the Complete Data Set," *The Astrophysical Journal,* vol. 709, no. 2, pp. 1257-1283, 2010.

[63] Y. Wu, G. Helou, L. Armus, D. Cormier, Y. Shi, D. Dale, K. Dasyra, J. D. Smith, C. Papovich, B. Draine, N. Rahman, S. Stierwalt, D. Fadda, G. Lagache and E. L. Wright, "Infrared Luminosities and Aromatic Features in the 24 μm Flux-limited Sample of 5MUSES," *The Astrophysical Journal,* vol. 723, no. 1, pp. 895-914, 2010.

[64] L. Sargsyan, D. Weedman, V. Lebouteiller, J. Houck, D. Barry, A. Hovhannisyan and A. Mickaelian, "Infrared Spectra and Spectral Energy Distributions for Dusty Starbursts and Active Galactic Nuclei," *The Astrophysical Journal,* vol. 730, no. 1, p. 19, 2011.

[65] H. Inami, L. Armus, V. Charmandaris, B. Groves, L. Kewley, A. Petric, S. Stierwalt, T. Díaz-Santos, J. Surace, J. Rich and ..., "Mid-infrared Atomic Fine-structure Emission-line Spectra of Luminous Infrared Galaxies: Spitzer/IRS Spectra of the GOALS Sample," *The Astrophysical Journal,* vol. 777, no. 2, p. 156, 2013.

[66] S. Stierwalt, L. Armus, J. A. Surace, H. Inami, A. O. Petric, T. Diaz-Santos, S. Haan, V. Charmandaris, J. Howell, D. C. Kim, J. Marshall, J. Mazzarella and ..., "Mid-infrared Properties of Nearby Luminous Infrared Galaxies. I. Spitzer Infrared Spectrograph Spectra for the GOALS Sample," *The Astrophysical Journal Supplement,* vol. 206, no. 1, p. 1, 2013.

[67] P. Madau, L. Pozzetti and M. Dickinson, "The Star Formation History of Field Galaxies," *The Astrophysical Journal,* vol. 498, no. 1, pp. 106-116, 1998.

[68] N. A. Reddy and C. C. Steidel, "A Steep Faint-End Slope of the UV Luminosity Function at z ~ 2-3: Implications for the Global Stellar Mass Density and Star Formation in Low-Mass Halos," *The Astrophysical Journal,* vol. 692, no. 1, pp. 778-803, 2009.

[69] X. Fan, J. F. Hennawi, G. T. Richards, M. A. Strauss, D. P. Schneider, J. L. Donley, J. E. Young, J. Annis, H. Lin, H. Lampeitl, R. H. Lupton and ..., "A Survey of z>5.7 Quasars in the Sloan Digital Sky Survey. III. Discovery of Five Additional Quasars," *The Astronomical Journal,* vol. 128, no. 2, pp. 515-522, 2004.

[70] S. M. Croom, R. J. Smith, B. J. Boyle, T. Shanks, L. Miller, P. J. Outram and N. S. Loaring, "The 2dF QSO Redshift Survey - XII. The spectroscopic catalogue and luminosity function," *Monthly Notices of the Royal Astronomical Society,* vol. 349, no. 4, pp. 1397-1418, 2004.

[71] M. J. I. Brown, K. Brand, A. Dey, B. T. Jannuzi, R. Cool, E. Le Floc'h, C. S. Kochanek, L. Armus, C. Bian, J. Higdon, S. Higdon and ..., "The 1 < z < 5 Infrared Luminosity Function of Type I Quasars," *The Astrophysical Journal,* vol. 638, no. 1, pp. 88-99, 2006.

[72] G. L. Pilbratt, J. R. Riedinger, T. Passvogel, G. Crone, D. Doyle, U. Gageur, A. M. Heras, C. Jewell, L. Metcalfe, S. Ott and M. Schmidt, "Herschel Space Observatory. An ESA facility for far-infrared and submillimetre astronomy," *Astronomy and Astrophysics,* vol. 518, p. L1, 2010.

[73] A. Poglitsch, C. Waelkens, N. Geis, H. Feuchtgruber, B. Vandenbussche, L. Rodriguez, O. Krause, E. Renotte, C. van Hoof, P. Saraceno, J. Cepa, F. Kerschbaum, P. Agnèse, B. Ali, B. Altieri and ..., "The Photodetector Array Camera and Spectrometer (PACS) on the Herschel Space Observatory," *Astronomy and Astrophysics,* vol. 518, p. L2, 2010.

[74] V. Lebouteiller, D. J. Barry, H. W. W. Spoon, J. Bernard-Salas, G. C. Sloan, J. R. Houck and D. W. Weedman, "CASSIS: The Cornell Atlas of Spitzer/Infrared Spectrograph Sources," *The Astrophysical Journal Supplement,* vol. 196, no. 1, p. 8, 2011.

[75] L. Sargsyan, V. Lebouteiller, D. Weedman, H. Spoon, J. Bernard-Salas, D. Engels, G. Stacey, J. Houck, D. Barry, J. Miles and A. Samsonyan, "[C II] 158 μm Luminosities and Star Formation Rate in Dusty Starbursts and Active Galactic Nuclei," *The Astrophysical Journal,* vol. 755, no. 2, p. 171, 2012.

[76] J. Fischer, E. Sturm, E. González-Alfonso, J. Graciá-Carpio, S. Hailey-Dunsheath, A. Poglitsch, A. Contursi, D. Lutz, R. Genzel, A. Sternberg, A. Verma and L. Tacconi, "Herschel-PACS spectroscopic diagnostics of local ULIRGs: Conditions and kinematics in Markarian 231," *Astronomy and Astrophysics,* vol. 518, p. L41, 2010.

[77] E. Peeters, H. W. W. Spoon and A. G. G. M. Tielens, "Polycyclic Aromatic Hydrocarbons as a Tracer of Star Formation?," *The Astrophysical Journal,* vol. 613, no. 2, pp. 986-1003, 2004.

[78] R. Genzel, D. Lutz, E. Sturm, E. Egami, D. Kunze, A. F. M. Moorwood, D. Rigopoulou, H. W. W. Spoon, A. Sternberg, L. E. Tacconi-Garman, L. Tacconi and N. Thatte,

"What Powers Ultraluminous IRAS Galaxies?," *The Astrophysical Journal,* vol. 498, no. 2, pp. 579-605, 1998.

[79] S. J. U. Higdon, D. Devost, J. L. Higdon, B. R. Brandl, J. R. Houck, P. Hall, D. Barry, V. Charmandaris, J. D. T. Smith, G. C. Sloan and J. Green, "The SMART Data Analysis Package for the Infrared Spectrograph on the Spitzer Space Telescope," *The Publications of the Astronomical Society of the Pacific,* vol. 116, no. 824, pp. 975-984, 2004.

[80] V. Lebouteiller, D. Cormier, S. C. Madden, F. Galliano, R. Indebetouw, N. Abel, M. Sauvage, S. Hony, A. Contursi, A. Poglitsch, A. Rémy, E. Sturm and R. Wu, "Physical conditions in the gas phases of the giant H II region LMC-N 11 unveiled by Herschel . I. Diffuse [C II] and [O III] emission in LMC-N 11B," *Astronomy & Astrophysics,* vol. 548, p. A91, 2012.

[81] D. J. Hollenbach and A. G. G. M. Tielens, "Photodissociation regions in the interstellar medium of galaxies," *Reviews of Modern Physics,* vol. 71, no. 1, pp. 173-230, 1999.

[82] N. P. Abel, C. Dudley, J. Fischer, S. Satyapal and P. A. M. van Hoof, "Dust-Bounded Ultraluminous Infrared Galaxies: Model Predictions for Infrared Spectroscopic Surveys," *The Astrophysical Journal,* vol. 701, no. 2, pp. 1147-1160, 2009.

[83] B. Mookerjea, C. Kramer, C. Buchbender, M. Boquien, S. Verley, M. Relaño, G. Quintana-Lacaci, S. Aalto, J. Braine, D. Calzetti, F. Combes and ..., "The Herschel M 33 extended survey (HerM33es): PACS spectroscopy of the star-forming region BCLMP 302," *Astronomy & Astrophysics,* vol. 532, p. A152, 2011.

[84] T. Velusamy, W. D. Langer, J. L. Pineda and P. F. Goldsmith, "[C ii] 158 μm line detection of the warm ionized medium in the Scutum-Crux spiral arm tangency," *Astronomy & Astrophysics,* vol. 541, p. L10, 2012.

[85] J. Bernard-Salas, E. Habart, H. Arab, A. Abergel, E. Dartois, P. Martin, S. Bontemps, C. Joblin, G. J. White, J. -P. Bernard and D. Naylor, "Spatial variation of the cooling lines in the Orion Bar from Herschel/PACS," *Astronomy & Astrophysics,* vol. 538, p. 37, 2012.

[86] K. V. Croxall, J. D. Smith, M. G. Wolfire, H. Roussel, K. M. Sandstrom, B. T. Draine, G. Aniano, D. A. Dale, L. Armus, P. Beirão, G. Helou, A. D. Bolatto and ..., "Resolving the Far-IR Line Deficit: Photoelectric Heating and Far-IR Line Cooling in NGC 1097 and NGC 4559," *The Astrophysical Journal,* vol. 747, no. 1, p. 81, 2012.

[87] P. Beirão, L. Armus, G. Helou, P. N. Appleton, J. -D. T. Smith, K. V. Croxall, E. J. Murphy, D. A. Dale, B. T. Draine, M. G. Wolfire, K. M. Sandstrom and ..., "A Study of

Heating and Cooling of the ISM in NGC 1097 with Herschel-PACS and Spitzer-IRS," *The Astrophysical Journal,* vol. 751, no. 2, p. 144, 2012.

[88] M. Imanishi, C. C. Dudley, R. Maiolino, P. R. Maloney, T. Nakagawa and G. Risaliti, "A Spitzer IRS Low-Resolution Spectroscopic Search for Buried AGNs in Nearby Ultraluminous Infrared Galaxies: A Constraint on Geometry between Energy Sources and Dust," *The Astrophysical Journal Supplement Series,* vol. 171, no. 1, pp. 72-100, 2007.

[89] N. A. Levenson, M. M. Sirocky, L. Hao, H. W. W. Spoon, J. A. Marshall, M. Elitzur and J. R. Houck, "Deep Mid-Infrared Silicate Absorption as a Diagnostic of Obscuring Geometry toward Galactic Nuclei," *The Astrophysical Journal,* vol. 654, no. 1, pp. L45-L48, 2007.

[90] V. Buat, E. Giovannoli, D. Burgarella, B. Altieri, A. Amblard, V. Arumugam, H. Aussel, T. Babbedge, A. Blain, J. Bock, A. Boselli, N. Castro-Rodríguez, A. Cava and ..., "Measures of star formation rates from infrared (Herschel) and UV (GALEX) emissions of galaxies in the HerMES fields," *Monthly Notices of the Royal Astronomical Society: Letters,* vol. 409, no. 1, pp. L1-L6, 2010.

[91] D. W. Weedman and J. R. Houck, "The Most Luminous Starbursts in the Universe," *The Astrophysical Journal,* vol. 686, no. 1, pp. 127-137, 2008.

[92] H. W. W. Spoon, L. Armus, J. Cami, A. G. G. M. Tielens, J. E. Chiar, E. Peeters, J. V. Keane, V. Charmandaris, P. N. Appleton, H. I. Teplitz and M. J. Burgdorf, "Fire and Ice: Spitzer Infrared Spectrograph (IRS) Mid-Infrared Spectroscopy of IRAS F00183-7111," *The Astrophysical Journal Supplement Series,* vol. 154, no. 1, pp. 184-187, 2004.

[93] L. Hao, H. W. W. Spoon, G. C. Sloan, J. A. Marshall, L. Armus, A. G. G. M. Tielens, B. Sargent, I. M. van Bemmel, V. Charmandaris, D. W. Weedman and J. R. Houck, "The Detection of Silicate Emission from Quasars at 10 and 18 Microns," *The Astrophysical Journal,* vol. 625, no. 2, pp. L75-L78, 2005.

[94] G. H. Rieke, E. T. Young, C. W. Engelbracht, D. M. Kelly, F. J. Low, E. E. Haller, J. W. Beeman, K. D. Gordon, J. A. Stansberry, K. A. Misselt, J. Cadien, J. E. Morrison, G. Rivlis, W. B. Latter, A. Noriega-Crespo and ..., "The Multiband Imaging Photometer for Spitzer (MIPS)," *The Astrophysical Journal Supplement Series,* vol. 154, no. 1, pp. 25-29, 2004.

[95] G. E. Magdis, D. Elbaz, H. S. Hwang, A. Amblard, V. Arumugam, H. Aussel, A. Blain, J. Bock, A. Boselli, V. Buat, N. Castro-Rodríguez, A. Cava and ..., "Herschel reveals a Tdust-unbiased selection of z ~ 2 ultraluminous infrared galaxies," *Monthly Notices of the Royal Astronomical Society,* vol. 409, no. 1, pp. 22-28, 2010.

[96] V. Desai, B. T. Soifer, A. Dey, E. Le Floc'h, L. Armus, K. Brand, M. J. I. Brown, M. Brodwin, B. T. Jannuzi, J. R. Houck, D. W. Weedman and ..., "Strong Polycyclic Aromatic Hydrocarbon Emission from z ≈ 2 ULIRGs," *The Astrophysical Journal,* vol. 700, no. 2, pp. 1190-1204, 2009.

[97] D. Farrah, C. J. Lonsdale, D. W. Weedman, H. W. W. Spoon, M. Rowan-Robinson, M. Polletta, S. Oliver, J. R. Houck and H. E. Smith, "The Nature of Star Formation in Distant Ultraluminous Infrared Galaxies Selected in a Remarkably Narrow Redshift Range," *The Astrophysical Journal,* vol. 677, no. 2, pp. 957-969, 2008.

[98] J. R. Houck, D. W. Weedman, E. Le Floc'h and L. Hao, "Spitzer Spectra of a 10 mJy Galaxy Sample and the Star Formation Rate in the Local Universe," *The Astrophysical Journal,* vol. 671, no. 1, pp. 323-332, 2007.

[99] L. A. Sargsyan, D. W. Weedman and J. R. Houck, "Comparing Ultraviolet- and Infrared-selected Starburst Galaxies in Dust Obscuration and Luminosity," *The Astrophysical Journal,* vol. 715, no. 2, pp. 986-1005, 2010.

[100] L. C. Ho and E. Keto, "The Mid-Infrared Fine-Structure Lines of Neon as an Indicator of Star Formation Rate in Galaxies," *The Astrophysical Journal,* vol. 658, no. 1, pp. 314-318, 2007.

[101] D. Calzetti, S. -Y. Wu, S. Hong, R. C. Kennicutt, J. C. Lee, D. A. Dale, C. W. Engelbracht, L. van Zee, B. T. Draine, C. -N. Hao, K. D. Gordon, J. Moustakas and ..., "The Calibration of Monochromatic Far-Infrared Star Formation Rate Indicators," *The Astrophysical Journal,* vol. 714, no. 2, pp. 1256-1279, 2010.

[102] O. Laurent, I. F. Mirabel, V. Charmandaris, P. Gallais, S. C. Madden, M. Sauvage, L. Vigroux and C. Cesarsky, "Mid-infrared diagnostics to distinguish AGNs from starbursts," *Astronomy and Astrophysics,* vol. 659, pp. 887-899, 2000.

[103] G. M. Voit, "Infrared Fine-Structure Line Diagnostics of Shrouded Active Galactic Nuclei," *Astrophysical Journal,* vol. 399, p. 495, 1992.

[104] E. Sturm, D. Lutz, A. Verma, H. Netzer, A. Sternberg, A. F. M. Moorwood, E. Oliva and R. Genzel, "Mid-Infrared line diagnostics of active galaxies. A spectroscopic AGN survey with ISO-SWS," *Astronomy and Astrophysics,* vol. 393, pp. 821-841, 2002.

[105] A. Verma, D. Lutz, E. Sturm, A. Sternberg, R. Genzel and W. Vacca, "A mid-infrared spectroscopic survey of starburst galaxies: Excitation and abundances," *Astronomy and Astrophysics,* vol. 403, pp. 829-846, 2003.

[106] L. Sargsyan, A. Samsonyan, V. Lebouteiller, D. Weedman, D. Barry, J. Bernard-Salas, J. Houck and H. Spoon, "Star Formation Rates from [C II] 158 μm and Mid-infrared

Emission Lines for Starbursts and Active Galactic Nuclei," *The Astrophysical Journal,* vol. 790, no. 1, p. 15, 2014.

[107] A. O. Petric, L. Armus, J. Howell, B. Chan, J. M. Mazzarella, A. S. Evans, J. A. Surace, D. Sanders, P. Appleton, V. Charmandaris and ..., "Mid-Infrared Spectral Diagnostics of Luminous Infrared Galaxies," *The Astrophysical Journal,* vol. 730, no. 1, p. 28, 2011.

[108] R. C. Kennicutt, D. Calzetti, G. Aniano, P. Appleton, L. Armus, P. Beirão, A. D. Bolatto, B. Brandl, A. Crocker, K. Croxall, D. A. Dale, J. Donovan Meyer, B. T. Draine and ..., "KINGFISH—Key Insights on Nearby Galaxies: A Far-Infrared Survey with Herschel: Survey Description and Image Atlas," *Publications of the Astronomical Society of the Pacific,* vol. 123, no. 910, p. 1347, 2011.

[109] T. Díaz-Santos, L. Armus, V. Charmandaris, S. Stierwalt, E. J. Murphy, S. Haan, H. Inami, S. Malhotra, R. Meijerink, G. Stacey, A. O. Petric, A. S. Evans and ..., "Explaining the [C II]157.7 μm Deficit in Luminous Infrared Galaxies—First Results from a Herschel/PACS Study of the GOALS Sample," *The Astrophysical Journal,* vol. 774, no. 1, p. 68, 2013.

[110] D. Farrah, V. Lebouteiller, H. W. W. Spoon, J. Bernard-Salas, C. Pearson, D. Rigopoulou, H. A. Smith, E. González-Alfonso, D. L. Clements, A. Efstathiou, D. Cormier, J. Afonso and ..., "Far-infrared Fine-structure Line Diagnostics of Ultraluminous Infrared Galaxies," *The Astrophysical Journal,* vol. 776, no. 1, p. id. 38, 2013.

[111] B. Lo Faro, A. Franceschini, M. Vaccari, L. Silva, G. Rodighiero, S. Berta, J. Bock, D. Burgarella, V. Buat, A. Cava, D. L. Clements, A. Cooray, D. Farrah and ..., "The Complex Physics of Dusty Star-forming Galaxies at High Redshifts as Revealed by Herschel and Spitzer," *The Astrophysical Journal,* vol. 762, no. 2, p. 108, 2013.

[112] J. Melbourne, B. T. Soifer, V. Desai, A. Pope, L. Armus, A. Dey, R. S. Bussmann, B. T. Jannuzi and S. Alberts, "The Spectral Energy Distributions and Infrared Luminosities of $z \approx 2$ Dust-obscured Galaxies from Herschel and Spitzer," *The Astronomical Journal,* vol. 143, no. 5, p. 125, 2012.

[113] D. Elbaz, M. Dickinson, H. S. Hwang, T. Díaz-Santos, G. Magdis, B. Magnelli, D. Le Borgne, F. Galliano, M. Pannella, P. Chanial, L. Armus and ..., "GOODS-Herschel: an infrared main sequence for star-forming galaxies," *Astronomy & Astrophysics,* vol. 533, p. A119, 2011.

[114] Y. Zhao, N. Lu, C. K. Xu, Y. Gao, S. Lord, J. Howell, K. G. Isaak, V. Charmandaris, T. Diaz-Santos, P. Appleton, A. Evans and ..., "A Herschel Survey of the [N II] 205 μm Line in Local Luminous Infrared Galaxies: The [N II] 205 μm Emission as a Star

Formation Rate Indicator," *The Astrophysical Journal Letters,* vol. 765, no. 1, p. L13, 2013.

[115] G. Helou, I. R. Khan, L. Malek and L. Boehmer, "IRAS Observations of Galaxies in the Virgo Cluster Area," *Astrophysical Journal Supplement,* vol. 68, p. 151, 1988.

[116] T. Díaz-Santos, L. Armus, V. Charmandaris, G. Stacey, E. J. Murphy, S. Haan, S. Stierwalt, S. Malhotra, P. Appleton, H. Inami, G. E. Magdis and ..., "Extended [C II] Emission in Local Luminous Infrared Galaxies," *The Astrophysical Journal Letters,* vol. 788, no. 1, p. L17, 2014.

[117] F. R. Feldman, D. W. Weedman, V. A. Balzano and L. W. Ramsey, "Emission-line widths in galactic nuclei.," *Astrophysical Journal,* vol. 256, pp. 427-434, 1982.

[118] M. Whittle, "The narrow line region of active galaxies - I. Nuclear O III profiles.," *Monthly Notices of the Royal Astronomical Society,* vol. 213, pp. 1-31, 1985.

[119] H. W. W. Spoon, D. Farrah, V. Lebouteiller, E. González-Alfonso, J. Bernard-Salas, T. Urrutia, D. Rigopoulou, M. S. Westmoquette, H. A. Smith, J. Afonso and ..., "Diagnostics of AGN-Driven Molecular Outflows in ULIRGs from Herschel-PACS Observations of OH at 119 μm," *The Astrophysical Journal,* vol. 775, no. 2, p. 127, 2013.

[120] V. Lebouteiller, D. J. Barry, C. Goes, G. C. Sloan, H. W. W. Spoon, D. W. Weedman, J. Bernard-Salas and J. R. Houck, "CASSIS: The Cornell Atlas of Spitzer/Infrared Spectrograph Sources. II. High-resolution Observations," *The Astrophysical Journal Supplement Series,* vol. 218, no. 2, p. 21, 2015.

[121] A. Samsonyan, D. Weedman, V. Lebouteiller, D. Barry and L. Sargsyan, "Neon and [C II] 158 μm Emission Line Profiles in Dusty Starbursts and Active Galactic Nuclei," *The Astrophysical Journal Supplement Series,* vol. 226, no. 1, p. 11, 2016.

[122] K. M. Dasyra, L. C. Ho, H. Netzer, F. Combes, B. Trakhtenbrot, E. Sturm, L. Armus and D. Elbaz, "A View of the Narrow-line Region in the Infrared: Active Galactic Nuclei with Resolved Fine-structure Lines in the Spitzer Archive," *The Astrophysical Journal,* vol. 740, no. 2, p. 94, 2011.

[123] J. Bernard-Salas, E. Peeters, G. C. Sloan, S. Gutenkunst, M. Matsuura, A. G. G. M. Tielens, A. A. Zijlstra and J. R. Houck, "Unusual Dust Emission from Planetary Nebulae in the Magellanic Clouds," *The Astrophysical Journal,* vol. 699, no. 2, pp. 1541-1552, 2009.

[124] S. R. Pottasch and J. Bernard-Salas, "Planetary nebulae abundances and stellar evolution II," *Astronomy and Astrophysics,* vol. 517, p. A95, 2010.

[125] V. Lebouteiller, J. Bernard-Salas, G. C. Sloan and D. J. Barry, "Advanced Optimal Extraction for the Spitzer/IRS," *Publications of the Astronomical Society of the Pacific,* vol. 122, no. 888, p. 231, 2010.

[126] E. L. Wright, "A Cosmology Calculator for the World Wide Web," *The Publications of the Astronomical Society of the Pacific,* vol. 118, no. 850, pp. 1711-1715, 2006.

[127] A. W. Janssen, N. Christopher, E. Sturm, S. Veilleux, A. Contursi, E. González-Alfonso, J. Fischer, R. Davies, A. Verma and ..., "Broad [C II] Line Wings as Tracer of Molecular and Multi-phase Outflows in Infrared Bright Galaxies," *The Astrophysical Journal,* vol. 822, no. 1, p. 43, 2016.

[128] M. G. Smith and D. W. Weedman, "Internal Kinematics of the 30 Doradus Nebula in the Large Magellanic Cloud.," *Astrophysical Journal,* vol. 172, p. 307, 1972.

[129] C. H. Nelson and M. Whittle, "Stellar and Gaseous Kinematics of Seyfert Galaxies. II. The Role of the Bulge," *Astrophysical Journal,* vol. 465, p. 96, 1996.

[130] S. Malhotra, G. Helou, G. Stacey, D. Hollenbach, S. Lord, C. A. Beichman, H. Dinerstein, D. A. Hunter, K. Y. Lo, N. Y. Lu, R. H. Rubin, N. Silbermann, H. A. J. Thronson and M. W. Werner, "Infrared Space Observatory Measurements of [C II] Line Variations in Galaxies," *The Astrophysical Journal,* vol. 491, no. 1, pp. L27-L30, 1997.

[131] T. Nikola, R. Genzel, F. Herrmann, S. C. Madden, A. Poglitsch, N. Geis, C. H. Townes and G. J. Stacey, "[C ii] Emission from NGC 4038/9 (the ``Antennae")," *The Astrophysical Journal,* vol. 504, no. 2, pp. 749-760, 1998.

[132] A. L. Samsonyan, "Analysis of Emission Line Widths of [CII] 158μm," *Astrophysics,* vol. 65, no. 2, pp. 151-160, 2022.

[133] M. F. Skrutskie, R. M. Cutri, R. Stiening, M. D. Weinberg, S. Schneider, J. M. Carpenter, C. Beichman, R. Capps, T. Chester, J. Elias, J. Huchra, J. Liebert, C. Lonsdale, D. G. Monet, S. Price, P. Seitzer and ..., "The Two Micron All Sky Survey (2MASS)," *The Astronomical Journal,* vol. 131, no. 2, pp. 1163-1183, 2006.

[134] E. L. Wright, P. R. M. Eisenhardt, A. K. Mainzer, M. E. Ressler, R. M. Cutri, T. Jarrett, J. D. Kirkpatrick, D. Padgett, R. S. McMillan and ..., "The Wide-field Infrared Survey Explorer (WISE): Mission Description and Initial On-orbit Performance," *The Astronomical Journal,* vol. 140, no. 6, pp. 1868-1881, 2010.

[135] M. Whittle, "Virial and Jet-induced Velocities in Seyfert Galaxies. III. Galaxy Luminosity as Virial Parameter," *Astrophysical Journal,* vol. 387, p. 121, 1992.

[136] G. A. Shields, K. Gebhardt, S. Salviander, B. J. Wills, B. Xie, M. S. Brotherton, J. Yuan and M. Dietrich, "The Black Hole-Bulge Relationship in Quasars," *The Astrophysical Journal,* vol. 583, no. 1, pp. 124-133, 2003.

[137] S. M. Faber and R. E. Jackson, "Velocity dispersions and mass-to-light ratios for elliptical galaxies.," *Astrophysical Journal,* vol. 204, pp. 668-683, 1976.

[138] J. Kormendy and L. C. Ho, "Coevolution (Or Not) of Supermassive Black Holes and Host Galaxies," *Annual Review of Astronomy and Astrophysics,* vol. 51, no. 1, pp. 511-653, 2013.

[139] N. J. McConnell and C.-P. Ma, "Revisiting the Scaling Relations of Black Hole Masses and Host Galaxy Properties," *The Astrophysical Journal,* vol. 764, no. 2, p. 184, 2013.